

2017

Gravity Wave and Turbulence Transport in the Mesopause Region

Yafang Guo
Embry-Riddle Aeronautical University

Follow this and additional works at: <https://commons.erau.edu/edt>



Part of the [Atmospheric Sciences Commons](#), [Cosmology, Relativity, and Gravity Commons](#), and the [Engineering Physics Commons](#)

Scholarly Commons Citation

Guo, Yafang, "Gravity Wave and Turbulence Transport in the Mesopause Region" (2017). *Doctoral Dissertations and Master's Theses*. 346.
<https://commons.erau.edu/edt/346>

This Dissertation - Open Access is brought to you for free and open access by Scholarly Commons. It has been accepted for inclusion in Doctoral Dissertations and Master's Theses by an authorized administrator of Scholarly Commons. For more information, please contact commons@erau.edu.

**GRAVITY WAVE AND TURBULENCE TRANSPORT IN THE
MESOPAUSE REGION**

By

Yafang Guo

A dissertation submitted to the Physical Sciences Department

in Partial Fulfillment of the Requirements

for the Degree of

DOCTOR OF PHILOSOPHY

(Engineering Physics)

Embry-Riddle Aeronautical University

Daytona Beach, FL 32114

2017

Copyright by Yafang Guo 2017

All Rights Reserved

Gravity Wave and Turbulence Transport in the Mesopause Region

By Yafang Guo

This dissertation was prepared under the direction of the candidate's dissertation committee chair, Dr. Alan Z. Liu, and has been approved by the members of the dissertation committee. It was submitted to the College of Arts and Sciences and was accepted in partial fulfillment of the requirements for the

Degree of
Doctor of Philosophy in Engineering Physics



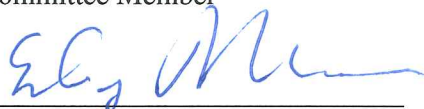
Dr. Alan Z. Liu, Ph.D
Committee Chair



Dr. Chester S. Gardner, Ph.D
Committee Member



Dr. Michael P. Hickey, Ph.D
Committee Member



Dr. Edwin Mierkiewicz, Ph.D
Committee Member



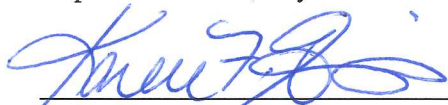
Dr. Jonathan B. Snively, Ph.D
Committee Member



Dr. Terry D. Oswalt, Ph.D
Department Chair, Physical Sciences



Dr. Michael P. Hickey, Ph.D
Dean of Research and Graduate Studies



Dr. Karen F. Gaines, Ph.D
Dean of College of Arts and Sciences

8/14/2017

Date

Acknowledgments

First of all, I would like to thank my advisor Dr. Alan Z. Liu for the continuous support of my Ph.D study during the past years, for his patience, motivation, and expertise. His guidance has helped me in all the time of research and writing of this dissertation. I could not have imagined having a better advisor and mentor for my Ph.D study. Many thanks to Dr. Liu's wife, Dr. Li Ding, for all the lovely parties and delicious Chinese food. Also I would like to thank the rest of my dissertation committee. Thank you, Dr. Chester Gardner for those significant insights and ideas in helping me fulfilling my Ph.D research. I have been learning a lot from your immense knowledge. It's my pleasure to work with you and have you as my committee. I would also like to thank Dr. Michael Hickey, Dr. Edwin Mierkiewicz, and Dr. Jonathan Snively for their help and comments. Finally, I would like to thank my family for all the support and encouragement through my education. The work in this dissertation was supported by the NSF grants AGS-1110199 and AGS-1115249.

Abstract

Vertical transport due to dissipating gravity waves and turbulence in the mesopause region (85-100 km) are analyzed with observational data obtained from a narrow-band sodium wind/temperature lidar located at Andes Lidar Observatory (ALO), Cerro Pachón (30.25° S, 70.73° W), Chile. The Na lidar at ALO has been in regular operation since 2010. The upgrade of the lidar system in May 2014 resulted in great improvements of the signal levels, which enabled data acquisition of high temporal and vertical resolutions reaching 6 s and 25 m. Traditional data processing utilizes signals at lower resolutions, typically at 60 s and 500 m, to reduce the measurement errors caused by photon noise. By using the high quality signals at much higher resolutions, the lidar is capable of resolving smallest scale gravity waves and even turbulence. This dissertation focuses on characterizing the vertical heat flux induced by both dissipating gravity waves and turbulence with observations after the upgrade. The vertical heat flux is defined as the covariance between vertical wind and temperature perturbations (also called sensible heat flux or enthalpy flux if it is potential temperature). The associated cooling and heating effects on the atmosphere due to this heat transport are also determined.

Starting from the observational data, the increased signal of ALO Na lidar significantly reduces the photon noise error but leads to challenges with photomultiplier tube (PMT) saturation at the same time. Corrections to this effect can be measured in a laboratory setting but may have large uncertainties at high photon count rates. Results show that this laboratory-correction can induce large errors for temperature, wind, and Na density measurements, which generates significant bias in the heat flux calculation due to the inherent correlation between vertical wind and temperature errors. A calibration procedure is developed to remove such PMT correction errors from laboratory measurements; then, the revised PMT correction curves are applied to reprocess the data. The corresponding heat

flux bias is also calculated with numerical simulations and observations, and both conclude that it is necessary to eliminate this bias from heat flux calculations.

Next, the seasonal variation of gravity wave vertical fluxes is calculated from over 400 hours of observations. The flux of potential temperature (enthalpy flux) and sensible heat are related through energy flux. The energy flux is estimated from vertical wavenumber (m) and frequency (ω) spectra of temperature perturbations. Flux of potential temperature exhibits a strong semi-annual variation with maximum downward transport appears at 95 km in Jan and 88 km in Aug. Energy flux decreases exponentially with altitude from 10^{-2} to 10^{-4} Wm^{-2} and is larger during southern hemisphere winter. In order to investigate the dissipation of different scale gravity waves and their contributions to the vertical transports, perturbations are separated into three scale ranges. Results show that shorter period gravity waves tend to dissipate at higher altitudes and generate more heat transports. Wave vertical group velocity is estimated from energy flux and total wave energy. The averaged vertical group velocities for high, medium, and low frequency waves are 3.9 ms^{-1} , 0.9 ms^{-1} , and 0.3 ms^{-1} , respectively.

In the end, with the high resolution raw data, a new method is developed to derive the turbulence by relating the turbulent perturbations to the photon count fluctuations. Using 150 h of lidar observations k_H is directly derived for the first time from eddy heat transport. Other key parameters such as the energy dissipation rate and the associated heating rate are also derived from the measurements without resorting to complex turbulence theory. Turbulence ω and m spectra are calculated, which follow the power law with slopes consistent with theoretical models. The eddy heat flux generally decreases with altitude from about -0.5 Kms^{-1} at 85 km to -0.1 Kms^{-1} at 100 km, with a local maximum of -0.6 Kms^{-1} at 93 km. The derived mean turbulence thermal diffusivity and energy dissipation rate are $43 \text{ m}^2 \text{ s}^{-1}$ and 37 mW kg^{-1} , respectively. The mean net cooling resulted from the heat transport and energy dissipation is $-4.9 \pm 1.5 \text{ Kd}^{-1}$, comparable to that due

to gravity wave transport at $-7.9 \pm 1.9 \text{ K d}^{-1}$. Turbulence key parameters show consistency with turbulence theories.

The results presented in this dissertation can contribute to a more comprehensive parameterization scheme in terms of the thermal structure and wave dissipation for the general circulation models (GCMs). The derived turbulence parameters and cooling/heating rates can provide significant references for parameterizing the wave-driven residual circulation by generating more realistic global thermal structures.

Contents

List of Tables	x
List of Figures	xi
1 Introduction	1
1.1 Atmospheric Gravity Waves	2
1.1.1 Background	2
1.1.2 Linear wave theory	4
1.2 Turbulence in the Atmosphere	7
1.2.1 Turbulence theory	8
1.2.2 Existing turbulence measurements	12
1.3 Research Motivations and Outline	14
1.3.1 Atmospheric transports	14
1.3.2 Objectives and outline	17
2 Sodium Lidar and Data Process	19
2.1 Sodium Fluorescence Hyperfine Spectrum	20
2.1.1 Sodium spectrum	21
2.1.2 Hanle effect	23
2.1.3 Effective scattering cross section	26
2.1.4 Three-frequency technique	28
2.2 ALO Lidar	29
2.2.1 ALO Na lidar system	31
2.2.2 Data summary	33

2.3	Data Processing	36
2.3.1	Lidar equation	36
2.3.2	Lidar data analysis	40
2.3.3	Error analysis	45
2.4	Data Processing Updates	50
2.4.1	Extinction coefficient	50
2.4.2	Hanle effect bias	51
3	PMT Nonlinearity and Calibration	54
3.1	Introduction	54
3.2	PMT Nonlinearity	57
3.2.1	Correction curves	57
3.2.2	Effect of PMT correction error	58
3.3	Correction of ALO Measurements	62
3.3.1	Evidence of error in PMT correction	62
3.3.2	Calibration of PMT correction curve	63
3.4	Heat Flux Bias due to PMT Correction Error	68
3.4.1	Numerical method	68
3.4.2	ALO heat flux correction	71
3.5	Summary	73
4	Dissipating Gravity Wave Induced Vertical Fluxes	75
4.1	Introduction	75
4.2	Observations	78
4.3	Energy Flux	81
4.4	Seasonal Heat Flux	85
4.5	Heat Flux due to Different Scale Waves	90

4.6	Summary	96
5	Atmospheric Turbulence and Turbulent Heat Flux	98
5.1	Introduction	98
5.2	Key Parameters of Turbulence	100
5.3	Observations	102
5.4	Signal Perturbation Method	104
5.4.1	Theory	104
5.4.2	Verification	107
5.5	Turbulence Power Spectra	109
5.6	Turbulence Measurements	111
5.7	Summary and Discussion	115
6	Conclusion	120
6.1	Summary	120
6.2	Future Work	125
A	Data Processing Procedures	127
A.1	Graphical User Interface	127
A.2	Procedures	128
A.3	Data Processing Example	130

List of Tables

2.1	Frequencies and relative strength of sodium D ₂ six transition lines.	23
2.2	Relative intensity of sodium D ₂ six transition lines for a linearly polarized lidar.	25
2.3	Earth's geomagnetic field over Andes Lidar Observatory, Cerro Pachón, Chile. Data is retrieved from NOAA' Geomagnetic Calculator.	25
2.4	Relative strength of sodium D ₂ six transition lines with Hanle effect.	26
2.5	ALO Na Lidar system parameters	34
2.6	Summary of lidar operation modes and data resolutions after upgrade.	36
4.1	Nights and hours of lidar vertical measurements for each month since the upgrade in May 2014, no data in December.	79
4.2	Magnitudes and altitudes of downward maxima for vertical heat fluxes induced by gravity waves with different periods.	93
4.3	Mean vertical energy flux, total energy density per unit volume, and group velocity for gravity waves with different periods.	95

List of Figures

1.1	Turbulence wavenumber (κ) energy spectrum. The well known Kolmogorov inertial subrange exhibits with a slope of $-5/3$ in the log-log coordinates. The Heisenberg viscous subrange is also shown as the dissipation range.	11
2.1	Energy level of the Na transition with frequency splitting. The basic model only includes two states, 3s ground state and 3p excited state. The electron spin causes the excited-state splits into a doublet, $^2p_{1/2}$ and $^2p_{3/2}$, corresponding to the D ₁ and D ₂ transition lines to the ground state $^2s_{1/2}$, respectively. Under the nuclear spin, the states $^2s_{1/2}$, $^2p_{1/2}$, and $^2p_{3/2}$ then split into 2, 2, and 4 energy hyperfine levels, respectively, labeled by total angular momentum of the atom, F , with the degeneracy $2f+1$. See [<i>She and Yu, 1995</i>]	22
2.2	Na absorption cross section for (a) three temperatures at $v_R = 0$ and (b) three wind velocities at $T = 200$ K. The three red dots are corresponding to the three frequencies adopted in lidar system to retrieve temperature and wind.	30
2.3	Schematic diagram of the ALO Na lidar. There are three main parts: a transmitter, a receiver, a data acquisition and system control.	32
2.4	Na lidar data summary including old and new data, total number of nights is 140, with 21 nights of old data, 119 from new data. Notice that there is no data in December for now.	34

2.5	Na lidar data summary including old and new data, total number of nights is 140, with 21 nights of old data, 119 from new data. Notice that there is no data in December for now.	35
2.6	A two dimensional calibration curve presenting the theoretical ratios R_T and R_w as functions of temperature (T) and LOS wind (W). R_T and R_w are calculated theoretically from the Na fluorescence effective backscattering cross section σ_{eff} . The curves can be used to retrieve T and W from experimental ratios.	42
2.7	Flow chart of ALO Na lidar data processing. There are three main blocks: preprocessing, main data processing, post-processing.	45
2.8	Temperature and wind measurement errors on the night of May 28th, 2014 at UT hour 10. Data was processed under the vertical and temporal resolution of 500 m and 90 s. The magnitude increases with decreasing signal levels. In the central Na layer, the average temperature error is around 1.1 K and wind error is 1 m/s.	49
2.9	(a) Temperature and (b) vertical wind (c) Na density with updated extinction coefficient calculation. The data is on May 28th, 2014 and processed with resolutions of 500 m and 90 s. Blues lines are the results when ignoring the difference between upward and downward extinction. Red lines are the updated results calculated from eq.(2.24). The averaged biases within the this altitude range are 0.75 K, 0.03 m/s and 0.54% for temperature, wind, and Na relative density, respectively.	52

2.10	(a) Temperature and (b) vertical wind derived under three circumstances: no Hanle effect (blue solid lines), with Hanle effect when zero magnetic field ($B=0$, red solid lines) and the magnetic field at ALO ($B=ALO$, black dashed lines). The data is on May 28th, 2014 and processed with resolutions of 500 m and 90 s. The mean temperature difference for blue and red lines is -0.31 K and 0.05 m/s for wind.	53
3.1	Old and new PMT correction curves. Green line is the Hamamatsu theoretical curve for an old PMT. Blue and red solid lines are laboratory measured corrections for old and new PMTs, respectively. Black line indicates linear response. Dashed lines indicate $\pm 10\%$ error on the correction amount. . . .	59
3.2	Temperature (left) and wind (right) errors as functions of the percentage of the PMT correction error (abscissa) and the count rate (ordinate) for the old PMT.	60
3.3	Same as Figure 3.2 but for the new PMT.	61
3.4	Na density (left) and vertical wind (right) in the zenith direction measured on the night of 6 November 2015. Data is processed in 60 s temporal and 500 m vertical resolutions, then smoothed with 15 min and 0.5 km full width hamming windows.	63
3.5	Same as Figure 3.4 but for temperatures in zenith (left), east (middle) and south (right) directions.	64
3.6	Scatter plots of the count rate at zenith vs. at east (left) and at south vs. at east (right) for same altitudes and times.	65
3.7	Scatter plots of the temperature differences of zenith minus east (left) and south minus east (right) vs. the output count rates. Exponential fittings and the fitting parameters are also shown.	66

3.8	Top: Old (blue) and new (red) PMT correction curves. Dashed lines are laboratory-measured correction curves. Solid lines are the adjusted curves based on measured temperature errors. The thin black line indicates the linear relationship. Bottom: The error percentages of the original old (blue) and new (red) PMTs correction curves.	67
3.9	Same as Figure 3.4 but with revised PMT correction curve.	68
3.10	Same as Figure 3.5 but with the revised PMT correction curves.	69
3.11	Left: Initial temperature and wind. Middle: Temperature and wind errors when +30% error is added to the PMT correction amount, with peak frequency count rate at 6 MHz. Right: Same as the middle except with peak frequency count rate at 12 MHz.	71
3.12	Heat flux bias as a function of count rate and the heat flux for a +30% error in PMT correction. See text for details.	72
3.13	Gravity wave heat flux calculated from 26 nights of zenith measurement of vertical wind and temperature from May 2014 to Apr 2015. Blue is the original heat flux profile and red is the profile obtained after the data were reprocessed using the revised PMT curve.	73
4.1	Seasonal variation of T' power spectra slopes. Blue line is frequency and red is for vertical wave number. The error bars represent the standard deviations calculated from linear fitting uncertainties.	84
4.2	Seasonal variation of gravity wave (a) temperature variance and (b) vertical energy flux inferred from eq. (4.2).	86
4.3	Seasonal variation of gravity wave vertical heat fluxes $\langle w'T' \rangle$ (a) and $\langle w'\theta' \rangle$ (b). The two heat flux are related through eq. (4.1).	89

4.4	(a) seasonal and (b) annual dynamical heating/cooling rate associated with dissipating gravity wave induced heat transport. Mean dynamical cooling rate throughout the region is -6.7 Kd^{-1} with a uncertainty of 1.1 Kd^{-1}	91
4.5	(a) sensible heat flux $\langle w'T' \rangle$ and (b) heat flux of potential temperature $\langle w'\theta' \rangle$ induced by gravity waves with different periods. Blue, red, and pink are related to waves with periods from 5 min to 1 hour, 1 to 3 hour, and 3 to 6 hour, respectively.	93
4.6	Transport velocities corresponding to three terms in eq.(4.1). Blue, red, and pink are corresponding to the first term, second term on the right side, and the left side, respectively.	96
5.1	Gravity wave temperature (top) and vertical wind (bottom) perturbations derived from traditional (blue) and SPM (red) throughout the night on September 6th, 2014 at 92 km. The overall structure matches well between the two different methods.	108
5.2	Scatter plot of gravity wave temperature (left) and vertical wind (right) perturbations derived from traditional (blue) and SPM (red) on September 6th, 2014 at 92 km.	108
5.3	Power spectra density of temperature perturbation (T') on Sep 7th, 2014. The curves represent the frequency spectra derived from SPM and traditional method in three different sets of resolutions.	109
5.4	Nightly (a) temporal frequency (ω) and (b) vertical wave number (m) spectra of relative temperature turbulent perturbations. Each colored line represents spectra on one night.	111

5.5	(a) Vertical wave number (m) and (b) temporal frequency (ω) spectra of relative temperature perturbations due to gravity waves (blue) and turbulence (red). Blue and red dashed lines represent the spectra predicted from theoretical models; solid lines are measured from high resolution lidar measurements; black dashed lines represent the data used for fitting.	112
5.6	(a) Vertical eddy heat flux, (b) thermal eddy diffusion coefficient k_H , and (c) energy dissipation rate ε calculated from lidar measurements.	112
5.7	(a) Turbulence-induced vertical wind variance and (b) turbulence-induced temperature variance measured from lidar observations (blue) and calculated using the k_H values (red) in Figure 5.6b and eq.(5.5) with a C_0 value of 0.37.	113
5.8	(a) Vertical gravity wave heat flux, (b) wave-induced vertical wind variance and (c) wave-induced temperature variance computed from the same lidar measurements used to derive the turbulence parameters shown in Figure 5.6.	114
5.9	Atmospheric heating/cooling rates associated with vertical heat transport by turbulence (eq. (5.6)) and waves.	116
A.1	The graphical user interface used to process the raw data of ALO Na lidar. Three modules are included: Pre-Processing,Parameter Retrieval, and Results Plotting	127
A.2	The count-per-shot in Zenith direction for peak (blue), plus (red), and minus (yellow) frequencies on April 24th, 2017. Left is in time-series, right is in the sequence of profile number.	130
A.3	Same as Figure A.2 but for Rayleigh signal.	131
A.4	Same as Figure A.2 but for combined profiles with 60 s integration time. . .	131

A.5 From left to right, top to bottom are the Na density, thermospheric Na layer, temperature, vertical wind, zonal wind, meridional wind on April 24th, 2017. The resolutions are 60 s in temporal and 500 m in vertical. 132

Chapter 1

Introduction

The Earth's atmosphere is stably stratified with pressure and density decreasing exponentially with altitude. However, the atmospheric temperature exhibits a more complicated vertical structure. Based on the temperature gradient over different altitude regions, the atmospheric regions are divided into the following layers: troposphere, stratosphere, mesosphere, thermosphere. The ionosphere is the layer that contains a relevant concentration of ions and free electrons and lies above the mesopause (the top of mesosphere) extending into the thermosphere. The lower atmosphere refers to troposphere and lower stratosphere, where weather phenomena occur and commercial airplanes fly. The middle atmosphere is usually defined as the middle stratosphere through the mesosphere and lower thermosphere. The region corresponding to the transition between the middle atmosphere and thermosphere is known as the MLT (Mesosphere and Lower Thermosphere), which has drawn a lot of attention because of its unique characteristics and composition. For instance, the region features an interesting phenomena in which the temperature is colder in summer than it is in winter. The mesopause is also the coldest and least stable region of the entire atmosphere, and where neutral metallic layers (Na, Fe, K, Ca, etc.) present. Over the last decades, our knowledge of the MLT has been expanded extensively through observations and models with studies mainly focused on describing and understanding its dynamics and variability.

1.1 Atmospheric Gravity Waves

1.1.1 Background

As a stratified fluid, one characteristic of the Earth's atmosphere is the ability to support wave motions. It is well recognized that the atmosphere is driven by various wave motions. Gravity waves produce one of the most important motions. They are generated when an atmospheric parcel is perturbed from its equilibrium position and the buoyancy and gravity act as the restoring forces driving the atmosphere back to the equilibrium level. Gravity waves are commonly observed in the oceans and atmosphere. Since the pioneering work done by *Hines* [1960], the dynamics and effects of atmospheric gravity waves have been widely acknowledged and studied. Research topics range from sources of wave generation, wave propagation, dissipation, breaking, as well as the accompanying influences on the background atmosphere [*Fritts and Alexander*, 2003]. Several dominant gravity wave sources have been identified based on theories, models, and observations. The most important sources include topography, convection, fronts, wind shear, wave-wave interactions, etc. The significance of each individual source depends on the region of the atmosphere considered and what location and season are discussed. Mountain waves form when stable air flow passes over a mountain. These are usually called stationary waves as they remain fixed to the observer and can often be observed as cloud bands. Mountain waves have been studied and modeled extensively with different methods [e.g. *Smith*, 1979, 1985; *Eckermann and Preusse*, 1999; *Jiang et al.*, 2002; *Wang et al.*, 2006; *Smith et al.*, 2009]. Unlike mountain waves, gravity waves generated by convection are more broadly distributed in terms of wave spectra. Several mechanisms have been proposed to explain the convective wave generation such as pure thermal forcing, an "obstacle" effect, and a "mechanical oscillator" effect [*Fovell et al.*, 1992]. There have been studies on wave occurrence related to

convection conducted in the troposphere and lower stratosphere [e.g. *Ceselski*, 1974; *Sato*, 1990; *Alexander et al.*, 1995; *Holton and Alexander*, 1999; *Walterscheid*, 2001; *Alexander et al.*, 2004; *Beres et al.*, 2005; *Vadas and Fritts*, 2006]. Compared with the previous two sources, other gravity wave sources like wind shear, fronts, wave-wave interactions, are less studied and more controversial. The conditions and mechanisms for them to excite waves are more complicated and difficult to quantify and require further understanding. However, their roles and importance are becoming better acknowledged with increasing theoretical, numerical, and observational studies [*Fritts*, 1982; *Chimonas and Grant*, 1984; *Fritts*, 1984; *Fritts and Nastrom*, 1992; *Klostermeyer*, 1990]. In terms of the wave propagation, gravity waves originating from the lower atmosphere propagate upward and can experience refraction, reflection, ducting, etc., depending on background conditions. Numerous studies have contributed to our understanding of these processes [*Taylor et al.*, 1995; *Hecht et al.*, 1997; *Li et al.*, 2007; *Snively et al.*, 2007; *Suzuki et al.*, 2013; *Bossert et al.*, 2014; *Cao et al.*, 2016; *Yuan et al.*, 2016]. As gravity waves propagate into higher altitudes, in order to maintain the conserved energy, wave amplitude increases exponentially due to the decreasing atmosphere density. Through this upward propagating process, gravity waves play an important role in coupling energy and momentum from their source regions, in the lower atmosphere, to the MLT. The carried energy and momentum are then deposited into the background atmosphere when waves reach upper mesosphere (near mesopause at ~ 85 km) through mechanisms such as instability, breaking, dissipation, saturation [*Weinstock*, 1982; *Huang and Smith*, 1991; *Medvedev and Klaassen*, 2003]. Characterizing the associated effects of gravity waves on the MLT generated by these mechanisms is the main objective in this dissertation and will be discussed in more detail in section 1.3.

1.1.2 Linear wave theory

Gravity waves are commonly described by linear theory in which perturbations are treated as the departures from a stably stratified state. Nowadays, most of our understanding of gravity waves is based upon this linear theory. It is an extremely useful tool in analyzing wave characteristics from observations. The review by *Fritts and Alexander* [2003] and textbook by *Nappo* [2013] have summarized the wave theory developed since the 1970s. A brief introduction of gravity wave linear theory is given below.

The basic governing equations arise from the conservation of mass, momentum, and energy, which are nonlinear. First of all, the inertial frequency, also called the Coriolis frequency, is defined as $2\Omega \sin \phi$, where Ω is the Earth's rotation rate, ϕ is the latitude. In this dissertation, only data from one site, located at Cerro Pachón, Chile (30.2°S , 70.7°W), is used so the inertial period corresponding to the Coriolis frequency is about 24 hours. Waves at this period will be strongly affected by the rotation of the Earth. Since this research only focuses on small and medium scale gravity waves with the largest period of 10 hours, mainly due to the 10 hours maximum nightly observation periods, the Earth's rotational effects are not considered in these equations. In addition, it is assumed that the background atmosphere varies only in altitude. Then the governing equations for 2-dimensional motions (x and z domains) are described as:

$$\begin{aligned}
 \frac{\partial u}{\partial t} + u \frac{\partial u}{\partial x} + w \frac{\partial u}{\partial z} &= -\frac{1}{\rho} \frac{\partial p}{\partial x} \\
 \frac{\partial w}{\partial t} + u \frac{\partial w}{\partial x} + w \frac{\partial w}{\partial z} &= -\frac{1}{\rho} \frac{\partial p}{\partial z} - g \\
 \frac{\partial \rho}{\partial t} + u \frac{\partial \rho}{\partial x} + w \frac{\partial \rho}{\partial z} + \frac{\partial u}{\partial x} + \frac{\partial w}{\partial z} &= 0 \\
 \frac{\partial \theta}{\partial t} + u \frac{\partial \theta}{\partial x} + w \frac{\partial \theta}{\partial z} &= 0
 \end{aligned} \tag{1.1}$$

where u and w are, respectively, the horizontal and vertical velocities; p is the pressure; ρ

is the density; g is the gravitational acceleration; x and z are the Cartesian coordinates in horizontal and vertical; θ is the potential temperature defined as:

$$\theta = \frac{p}{\rho R} \left(\frac{p_0}{p} \right)^\kappa = T \left(\frac{p_0}{p} \right)^\kappa. \quad (1.2)$$

Here p_0 is the pressure at reference level z_0 , R is the ideal gas constant, and $\kappa = R/c_p$, c_p is the specific heat at constant pressure, T is temperature. Assume the background parameters varying with altitude z are $(\bar{u}, 0)$ for winds, potential temperature $\bar{\theta}$, pressure \bar{p} , and density $\bar{\rho}$. The linearized eq. (1.1) can be expressed as

$$\begin{aligned} \frac{\partial u'}{\partial t} + \bar{u} \frac{\partial u'}{\partial x} + w' \frac{\partial \bar{u}}{\partial z} + \frac{\partial}{\partial x} \left(\frac{p'}{\bar{\rho}} \right) &= 0 \\ \frac{\partial w'}{\partial t} + \bar{u} \frac{\partial w'}{\partial x} + \frac{\partial}{\partial z} \left(\frac{p'}{\bar{\rho}} \right) &= \frac{1}{H} \left(\frac{p'}{\bar{\rho}} \right) - g \frac{\rho'}{\bar{\rho}} \\ \frac{\partial}{\partial t} \left(\frac{\rho'}{\bar{\rho}} \right) + \bar{u} \frac{\partial}{\partial x} \left(\frac{\rho'}{\bar{\rho}} \right) + \frac{\partial u'}{\partial x} + \frac{\partial w'}{\partial z} - \frac{w'}{H} &= 0 \\ \frac{\partial}{\partial t} \left(\frac{\theta'}{\bar{\theta}} \right) + \bar{u} \frac{\partial}{\partial x} \left(\frac{\theta'}{\bar{\theta}} \right) + w' \frac{N^2}{g} &= 0, \end{aligned} \quad (1.3)$$

where primes denote the perturbations, H is the scale height defined as the increase in altitude for which the atmospheric density/pressure decreases by a factor of e , $N = (g \partial \ln \theta / \partial z)^{1/2}$ is the buoyancy frequency. Solutions to eq. (1.3) are assumed to take the form:

$$\left(u', w', \frac{\theta'}{\bar{\theta}}, \frac{p'}{\bar{\rho}}, \frac{\rho'}{\bar{\rho}} \right) = (\tilde{u}, \tilde{w}, \tilde{\theta}, \tilde{p}, \tilde{\rho}) \cdot \exp \left[i(kx + mz - \omega t) + \frac{z}{2H} \right], \quad (1.4)$$

where k and m are the horizontal and vertical wavenumber, respectively. ω is the apparent frequency measured by an observer in a fixed coordinate system. The intrinsic frequency is defined, $\hat{\omega} = \omega - k\bar{u}$, as the frequency measured by an observer moving with the back-

ground winds, then eq.(1.3) can be rearranged as

$$\begin{aligned}
 -i\hat{\omega}\tilde{u} + \tilde{w}\frac{\partial\tilde{u}}{\partial z} + ik\frac{\tilde{p}}{\bar{\rho}} &= 0 \\
 -i\hat{\omega}\tilde{w} + \frac{\partial}{\partial z}\left(\frac{\tilde{p}}{\bar{\rho}}\right) - \frac{1}{H}\frac{\tilde{p}}{\bar{\rho}} + g\frac{\tilde{p}}{\bar{\rho}} &= 0 \\
 -i\hat{\omega}\tilde{\theta} + \frac{N^2}{g}\tilde{w} &= 0 \\
 -i\hat{\omega}\tilde{\rho} + ik\tilde{u} + \frac{\partial\tilde{w}}{\partial z} - \frac{\tilde{w}}{H} &= 0,
 \end{aligned} \tag{1.5}$$

Since the relative phase and amplitude of different perturbation quantities can be inferred from the above equations, eq.(1.5) are also described as the polarization equations. If one more dimension y is considered and the slowly changing background over a wave cycle is assumed (WKB approximation), the complete forms of the explicit polarization relations are listed as following (see *Fritts and Alexander* [2003]; *Vadas* [2013])

$$\begin{aligned}
 \tilde{u} &= \left(\frac{i\hat{\omega}k}{i\hat{\omega}l}\right)\tilde{v} \\
 \tilde{w} &= \frac{\hat{\omega}\left(-m - \frac{i}{2H}\right)}{N^2 - \hat{\omega}^2}\tilde{p} \\
 \tilde{\theta} &= \frac{-iN^2}{\hat{\omega}g}\tilde{w} \\
 \tilde{v} &= \frac{k\left(-m - \frac{i}{2H}\right)}{N^2 - \hat{\omega}^2}\tilde{u}.
 \end{aligned} \tag{1.6}$$

It is clear from the above relations that the potential temperature $\tilde{\theta}$ and vertical wind \tilde{w} perturbations are in quadrature, which results in zero heat flux $\langle w'\theta' \rangle$ (brackets denote an average over time, see more details about heat flux in Chapter 4) when averaged over a wave period (assuming no dissipation). Another important result obtained from the linear theory is the dispersion relation given by

$$m^2 = \frac{N^2k^2}{\hat{\omega}^2} - k^2 - \frac{1}{4H^2}. \tag{1.7}$$

The more complete version with background wind shear included is given in *Nappo* [2013] as

$$m^2 = \frac{N^2 k^2}{\hat{\omega}^2} + \frac{d^2 \bar{u}}{dz^2} \frac{k}{\hat{\omega}} - \frac{d\bar{u}}{dz} \frac{k}{H \hat{\omega}} - k^2 - \frac{1}{4H^2}. \quad (1.8)$$

This dispersion relation relates the wave numbers and frequency to the atmosphere background N and wind shear. The vertical wave group velocity is another crucial parameter in describing the wave propagation and energy transport, which is written as

$$\begin{aligned} (c_{gx}, c_{gy}, c_{gz}) &= \left(\frac{\partial \omega}{\partial k}, \frac{\partial \omega}{\partial l}, \frac{\partial \omega}{\partial m} \right) \\ &= (\bar{u}, \bar{v}, 0) + \frac{[k(N^2 - \hat{\omega}^2), l(N^2 - \hat{\omega}^2), -m\hat{\omega}^2]}{\hat{\omega} \left(k^2 + l^2 + m^2 + \frac{1}{4H^2} \right)}. \end{aligned} \quad (1.9)$$

For upward energy propagation gravity waves, the vertical component of group velocity, c_{gz} , is positive, and the vertical wave number m is negative. The wave dispersion and polarization relations have been useful tools when applied to describe and interpret observed gravity waves.

1.2 Turbulence in the Atmosphere

In addition to the wave motions, turbulence is also commonly observed in stably stratified atmosphere or ocean, such as the stable atmospheric boundary layer [e.g. *Albertson et al.*, 1997; *Sukoriansky et al.*, 2005; *Sun et al.*, 2015], upper troposphere and lower stratosphere [e.g. *Sharman et al.*, 2012], the MLT [e.g. *Lübken et al.*, 1993; *Fukao et al.*, 1994], oceans [e.g. *Seuront et al.*, 1996], and detectable via clouds, NLC, trace species, etc [e.g. *Falkovich et al.*, 2002]. It is believed that turbulence can influence the atmosphere physics and chemistry by transporting momentum, heat, and constituents, then result in the heating by energy dissipation, deceleration of mean circulation by momentum dissipation, and redistribution of constituents by turbulent mixing. Furthermore, some other atmospheric processes, such

as the transport of water vapor, heat transfer, clouds and precipitations, are also closely related to turbulence. However, turbulence has long been a difficult but important topic, which is described as “the last great unsolved problem of classical physics” due to the impossibility of solving the nonlinear equations of turbulence analytically. Since the revolutionary theory proposed by *Kolmogorov* [1941], our knowledge of turbulence has been rapidly expanded through numerical simulations and remote sensing experiments. This section will introduce the basic turbulence theory first, then summarize existing measurements of turbulence in the atmosphere.

1.2.1 Turbulence theory

A turbulent flow can be interpreted as composed by “eddies” of different sizes. The size l and the velocity u are applied to characterize the eddies. Because the turbulent flow consists of different size eddies, u and l are expected to vary within a certain range. A turbulent flow is said to be isotropic if the consideration of rotation and buoyancy are not important and there is no mean flow. Similarly, a flow is homogeneous if it is uniform in space and without preferential direction. In homogeneous and isotropic turbulence, all eddies of a given size (same l) behave more or less in the same way and can be thought of sharing the same characteristic velocity u . *Kolmogorov* [1941]’s theory not only provides a prediction for the energy spectrum of an isotropic homogeneous turbulent flow, but also proves that even though the velocity of an isotropic homogeneous turbulent flow fluctuates unpredictably, the energy spectrum describing how much kinetic energy is present on average at a particular scale is predictable. This theory basically answers three questions: 1) how energy is transferred from larger to smaller eddies, 2) how much energy is contained by eddies of a given size, 3) how much energy is dissipated by eddies of each size. Assuming a three dimensional turbulent flow, the velocities in each dimension are, respectively, u' , v' ,

and w' . Then the turbulent kinetic energy per unit mass is defined as:

$$KE = \frac{1}{2} (u'^2 + v'^2 + w'^2). \quad (1.10)$$

Among the eddies with different sizes, the large eddies are unstable and can easily break up into smaller eddies, thus transferring energy. Then the smaller eddies will undergo a similar break-up process and transfer their energy to even smaller eddies. This energy transfer is called the energy cascade, which will continue in the turbulent flow until the Reynolds number (defined as $Re = \frac{ul}{\nu}$, ν is the viscosity) is sufficiently small that the eddy motion is stable, and molecular viscosity is effective in dissipating the kinetic energy and converting it into heat. Then, average spatial scales increase again. If the state of turbulence is statistically steady, then the rate of energy transfer from one scale to the next is the same for all scales. The energy dissipation rate per unit mass can be expressed as:

$$\frac{d(KE)}{dt} = \varepsilon. \quad (1.11)$$

ε is an important parameter describing the rate of energy transferred from kinetic energy to thermal internal energy of the flow. The heating rate can be inferred from ε/c_p [Lübken, 1997], where c_p is the specific heat under constant pressure. The corresponding energy spectrum is denoted as $E(\kappa)$ and κ is the wavenumber. The integration of $E(\kappa)$ over all wavenumbers will then give the total energy as shown in the following equation:

$$KE = \int_0^{\infty} E(\kappa) d\kappa. \quad (1.12)$$

The inertial range is an intermediate range of turbulent scales or wavelengths that is smaller than the energy-containing eddies (large scales) but larger than viscous eddies (small scales). *Kolmogorov* [1941] also developed a spectrum theory for this inertial range by assuming

that the energy dissipation rate ε and wavenumber κ are the most important parameters in determining the energy. Now using a dimensional analysis:

$$[KE] = m^2 s^{-2}; [\varepsilon] = m^2 s^{-3}; [\kappa] = m^{-1};$$

$$[E(\kappa)] = [KE]/[\kappa] = m^3 s^{-2}.$$

The s^{-2} in $E(\kappa)$ can only be achieved by ε since there is no dependence of time in κ . Therefore, it can be simply determined that $E(\kappa)$ relies on $\varepsilon^{2/3}$. The final form of $E(\kappa)$ as a function of ε and κ is obtained as:

$$E(\kappa) = C\varepsilon^{2/3} \kappa^{-5/3}, \quad (1.13)$$

where C is the universal Kolmogorov constant, which was numerically determined to be $C = 1.5$. This is the famous Kolmogorov spectrum. The spectral slope, with a value of $-5/3$ has been widely observed and certified since then. The full spectrum of turbulence including the “energy containing range” and “dissipation range” is plotted in Figure 1.1. Characteristics of the turbulence spectrum at other ranges are further proposed. For example, *Heisenberg* [1948] predicted that the spectral slope follows a rapid decrease in the dissipation range with a slope of -7 . This dissertation will focus on the inertial range and the calculation of the turbulence energy spectrum with scales in this range. As the Na lidar data used in this study have limitations in the resolutions and measurement accuracies, the energy containing and dissipation ranges cannot be resolved; also because the scales in the energy containing range overlaps with the smallest gravity waves, it is difficult to distinguish between these small scale gravity waves and large scale turbulence in the energy containing range when considering a broad-band spectrum.

Turbulence induces transport of heat and momentum from the cascade process. Based

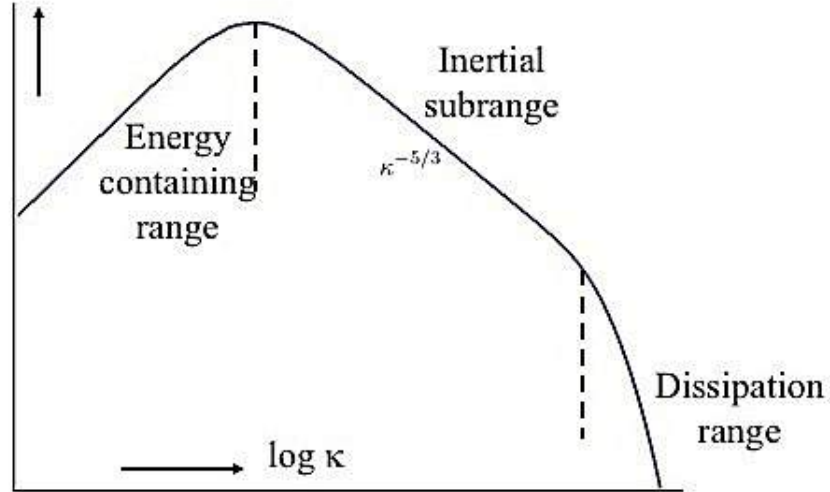


Figure 1.1: Turbulence wavenumber (κ) energy spectrum. The well known Kolmogorov inertial subrange exhibits with a slope of $-5/3$ in the log-log coordinates. The Heisenberg viscous subrange is also shown as the dissipation range.

on the governing equations of turbulence (see [Lumley and Panofsky, 1964, chapter 2]), the turbulent transport can be defined by turbulence exchange coefficients, namely diffusivities as follows:

$$\begin{aligned}
 k_M &= -\frac{1}{\rho} \frac{d\rho \langle w'u' \rangle}{dz} \\
 k_H &= -\frac{1}{\rho} \frac{d\rho \langle w'\theta' \rangle}{dz},
 \end{aligned}
 \tag{1.14}$$

where $\langle w'u' \rangle$ and $\langle w'\theta' \rangle$ are the turbulent momentum and heat fluxes, and k_M and k_H are the corresponding diffusivities, momentum diffusivity and thermal diffusivity, respectively. The ratio of k_M/k_H is the Prandtl number Pr . These coefficients are important for analyzing gravity wave and turbulence dynamics in the mesopause because this region is right below or near the turbopause (~ 105 km), which is the altitude where different diffusion mechanism dominates below and above. Above the turbopause, molecular diffusivity dominates and the chemical composition of the atmosphere varies according to chemical species, but below the turbopause, the constituents are well mixed due to the turbulent mixing process

represented by the turbulence diffusivities.

The common properties of turbulence are summarized here as:

- Turbulence is dissipative. Energy is eventually dissipated into internal energy through energy cascade, which is regarded as the essential feature of turbulence.
- Turbulence is three dimensional and nonlinear. The energy cascade can be treated as vortex stretching, which requires three dimensions. Also it happens only in one nonlinear way, from large to small size eddies.
- Turbulence is a continuum phenomenon. The smallest length scale of eddies in the turbulent flow is still much larger than the molecular collisional scales.
- Turbulence is stochastic. Practically, no matter how good experiments or observations are made, the turbulence field can not be captured fully in detail.
- Turbulence is diffusive. The mixing effect of turbulence is responsible statistically for diffusive transport of mass, heat, and momentum.

1.2.2 Existing turbulence measurements

Measurements of atmospheric turbulence have been made since the 1950s. Because of the unpredictable motion of turbulence, as well as their smaller scale compared to atmospheric waves, observing the turbulence dynamics has always been much more difficult than gravity waves. In general, turbulence is characterized in several ways: in the time domain, as auto- or cross-correlation functions, turbulent kinetic energy dissipation rates, and structure functions; or, in the Fourier domain, as one- or multi-dimensional auto- or cross-spectrum. These can be interpreted as measuring the transport of heat, momentum, and moisture by turbulence and determining the characteristics of turbulence spectra. For now, atmospheric turbulence is observed mostly at the lower atmosphere near the atmospheric

boundary layer (ABL), because of the easier access for instruments. The methods include ground-based remote sensing techniques such as windprofiler radar [*Schneider and Lilly, 1999*], radar/RASS [*Peters and Kirtzel, 1994*], sodar/RASS [*Engelbart and Bange, 2002*], radiosonde balloons [*Zhang et al., 2012*], and lidar [*O'Connor et al., 2010*]. In the MLT, where waves tend to dissipate and break through instabilities, turbulence can be generated frequently [e.g. *Hodges, 1967, 1969; Hines, 1988; Fritts et al., 2003; Zink and Vincent, 2004*]. Considerable progress has been made in understanding MLT turbulence over the past decades through observations mainly done by remote sensing techniques, including radars [e.g. *Hocking, 1986, 1996; Fukao et al., 1994*] and in situ rockets measurements of neutral density [e.g. *Lübken, 1992; Rapp et al., 2004*].

Among the observational studies in the MLT, there is one performed by *Lübken* [1997] that contributes a lot to our knowledge of turbulence in the upper mesosphere. *Lübken* [1997] used a series of 22 sounding rockets measurements at high latitudes within 6 years in the early 1990s. The study was based on detecting the small fluctuations in the neutral density, which were believed to be associated with the turbulent motions, with an ionization gauge equipped on the rockets. The important turbulence parameter, energy dissipation rate ϵ , and the corresponding heating rate, was then deduced from the power spectra of the relative density fluctuations. They found that ϵ shows significant seasonal variation, where turbulent activities are 10 times stronger around the summer mesopause than winter time, and also concluded that the turbulent heating is an important contribution to the MLT energy budget and can not be neglected. The turbulent diffusivities derived from the vertical wind variance have typical values between 4 and 100 m²/s near the mesopause. Mesospheric turbulence was also studied broadly by MST radars by inferring turbulent parameters from radar echoes [e.g. *Gage and Balsley, 1984*]. However, these in situ observations are necessarily restricted both temporally and spatially. In addition, direct numerical simulations have been an effective approach in studying turbulence but require powerful computing

capabilities [e.g. *Fritts et al.*, 2003, 2012].

1.3 Research Motivations and Outline

1.3.1 Atmospheric transports

It is known that gravity waves efficiently couple energy and momentum from source regions in the lower atmosphere to the middle and upper atmosphere through transport processes. During propagation, gravity waves can experience several mechanisms, such as dissipation, wave breaking, turbulent mixing, and critical level filtering. This can result in substantial influences on the MLT by their important roles such as driving the mean meridional circulation and thermal structure through deposition of energy, momentum, and heat into the background [e.g. *Hines*, 1960; *Hodges*, 1969; *Hines*, 1970; *Lindzen*, 1981; *Holton*, 1983; *Garcia and Solomon*, 1985; *Fritts and Alexander*, 2003; *Yiğit and Medvedev*, 2009; *Yiğit et al.*, 2009]. In terms of the atmosphere's thermal structure, the zonally averaged temperature of the Earth's atmosphere depends both on radiative and dynamical processes. In the limit where absorption of solar radiation (winter hemisphere, poles, etc.) and infrared emission control the temperature distribution, the atmosphere is in radiative equilibrium. However, vertical motions can produce significant local departures from this equilibrium through adiabatic processes. This wave driven process can result in the redistribution of the zonal mean temperature structure in the MLT. The warm winter mesopause and cold summer mesopause is one of the consequences of this process and has been known for decades. At high latitudes, the summer mesopause is typically several tens of K colder than the winter mesopause, even though the latter rarely receives any direct solar radiation. This large disturbance of the radiative equilibrium that occurs at the high-latitude mesopause requires a vigorous mean meridional circulation, with rising motion in summer and sinking in win-

ter, to balance the thermal budget at this level of the atmosphere. Gravity waves affect the zonal mean circulation by exerting a force (drag) on the background atmosphere, which have been widely acknowledged through analyzing the zonal and meridional momentum fluxes [e.g. *Vincent and Reid*, 1983; *Fritts and Vincent*, 1987; *Gardner et al.*, 1999; *Hocking*, 2005; *Fritts et al.*, 2006; *Gardner and Liu*, 2007; *Antonita et al.*, 2008; *Alexander et al.*, 2008, 2010; *Acott et al.*, 2011]. Besides the driven circulation by depositing gravity wave momentum, the vertical transport of atmospheric constituents is also very important and can largely affect the chemistry and composition of MLT [*Frederick*, 1979; *Fritts and Rastogi*, 1985; *Garcia and Solomon*, 1985; *Xu et al.*, 2003; *Gardner and Liu*, 2010, 2014]. There are several processes that are accounted when considering the vertical transport in the MLT including advection, turbulent mixing, dynamical, and chemical processes [*Gardner and Liu*, 2014]. Dissipating, but non-breaking, gravity waves induce dynamical and chemical transport. Gravity waves also contribute to the vertical transport by generating turbulence through breaking. Each mechanism can produce notable transport in the MLT. The vertical transport of several important chemical species have been investigated widely, such as metals (Na, Fe) [e.g. *Huang et al.*, 2015; *Liu and Gardner*, 2005; *Gardner and Liu*, 2010; *Gardner et al.*, 2016], O₃ [e.g. *Allen et al.*, 1981; *Bjarnason et al.*, 1987; *Strobel et al.*, 1987; *Bevilacqua et al.*, 1990], CO and OH [e.g. *Jin et al.*, 2005; *Funke et al.*, 2009; *Damiani et al.*, 2010; *Xu et al.*, 2012], CO₂ [e.g. *Kinnison et al.*, 2007; *Garcia et al.*, 2016], NO_x [e.g. *Bernath et al.*, 2005; *Rinsland et al.*, 2005; *Randall et al.*, 2006].

Despite significant studies into the momentum fluxes associated with gravity wave dynamics, their direct thermal impacts through heat transport are still not well understood. On one hand, even though dissipating GWs are expected to deposit energy in the MLT as a source of heating [*Hines*, 1965], *Walterscheid* [1981a] pointed out that gravity waves dissipated through a diffusive process also induce a downward sensible heat flux regardless of their propagation direction. This sensible heat flux creates a cooling effect in the upper

region of wave dissipation. On the other hand, GW dissipation can also occur through non-linear interactions and wave breaking, leading to turbulence, which generally dominates the molecular diffusion in the mesopause region [Fritts and Alexander, 2003]. Weinstock [1983] demonstrated a derivation of heat flux with nonlinear gravity wave equations and showed that the sensible heat flux is also downward and brings substantial cooling to the mesopause where waves are highly saturated. Many numerical simulations were also carried out to study the sensible heat flux by dissipating gravity waves [e.g. Liu *et al.*, 2000; Medvedev and Klaassen, 2003; Becker, 2004; Yiğit and Medvedev, 2009; Hickey *et al.*, 2011], which all confirmed the GW downward sensible heat flux and its cooling effect.

Aside from characterizing the sensible heat flux (the correlation between temperature and vertical wind), it is also important to better understand the vertical transport of thermal energy. This can be accomplished by using the potential temperature instead of the sensible temperature, which falls off with height adiabatically while the potential temperature is constant. Thus, the vertical transport of potential temperature (enthalpy flux) tells us about the transport of thermal energy by atmospheric motions similar to the way that sensible heat gets transferred in the atmosphere's energy budget. The detailed difference between these two transport definitions is discussed in Chapter 4.

Besides the transport by gravity waves, turbulence in the upper atmosphere (mostly generated by breaking gravity waves) also contributes to the heat, momentum, and constituent transports. The acknowledgment of turbulent transport predate our understanding of gravity waves in the MLT [Priestley and Swinbank, 1947; Montgomery, 1948; Swinbank, 1951]. The classic theory of turbulent heat transfer in the atmosphere states that the flux of heat is in the direction from high to low potential temperature. The turbulent heat flux was first discussed by Taylor [1915]. Later Priestley and Swinbank [1947] reexamined the eddy heat flux theory which will be discussed in the subsequent chapters and applied to both gravity wave and turbulence heat flux calculations.

1.3.2 Objectives and outline

The major objective of this dissertation is to better understand the effects of dissipating gravity waves on the MLT, mainly their effects on the energy budget, by quantifying the vertical heat and energy fluxes induced by gravity waves and turbulence. There have been very limited studies on determining the vertical fluxes due to dissipating gravity waves and turbulence in the MLT because of the difficulty in measuring the vertical wind and temperature simultaneously. Furthermore, vertical fluxes are characterized by the covariance of vertical wind and other quantities, which requires a relatively long term period of data for averaging. Another objective is to analyze the characteristics of gravity waves and turbulence, including their power spectra, seasonal activities, wind and temperature variances, and some other features, such as the dissipation of different scale waves, and the total thermal effect of gravity waves and turbulence.

The dissertation employs measurements from a high resolution Na lidar located at the Andes Lidar Observatory (ALO) in Chile. The lidar was deployed to ALO in 2009, and has been operated frequently since then. There was an upgrade in the optical alignment and a laser replacement on May 2014, which resulted in a significant increase of the signal levels. These improvements enable the data acquisition at high resolution (reaching 6 seconds and 25 meters) making it possible to detect gravity waves and turbulence at the same time. However, there are also severe saturation effects arising from the high signals. The saturation is caused by the nonlinearity of the Photon Multiplier Tube (PMT) in the lidar receiver system, and can introduce errors into the retrieval of temperature, wind, Na density from lidar data and also induce bias into the vertical flux calculations. Therefore, calibrating the PMT saturation effect and obtaining accurate retrieval from the lidar raw data is another objective in this dissertation.

Measuring the vertical transport by gravity wave and turbulence could lead to a more

comprehensive parameterization scheme in the general circulation models (GCMs). The current GCMs, such as WACCM, have placed emphasizes on parameterizing the forcing(drag) generated by gravity wave momentum flux divergence to obtain realistic mean circulations, but have neglected the heating and cooling effects of dissipating and breaking gravity waves on the thermal structure. The results presented here can provide references for future parameterization schemes in global models.

This dissertation covers four main chapters related to the objectives. Chapter 2 gives a review of the narrow-band Na lidar including the theory, data processing algorithm, and some updates in the data retrieval. Chapter 3 focuses on determining and correcting the PMT saturation effects on data processing and heat flux calculations. Chapter 4 presents the measurements of heat flux due to dissipating gravity waves and their seasonal variations with long term data. Chapter 5 provides a new method to derive turbulent perturbations and an analysis of turbulence characteristics. Finally, Chapter 6 provides the conclusion to this dissertation and discusses some future work.

Chapter 2

Sodium Lidar and Data Process

Atomic metals, such as Fe, Na, Ca, K, have been observed commonly in the upper atmosphere at the altitude ranging from about 80 to 100 km. The principal source of these metals is the ablation of meteoroids, which is defined as the cosmic dust particles. These particles entering the atmosphere are resulted from the collisions between asteroids and the sublimation of comets as they approach the Sun on their orbits through the solar system (see more details in the review by *Plane et al.* [2015]). The metal layer in the MLT enables the developments of modern techniques in detecting the dynamics in the metal layers. Lidar, stands for Light Detection and Ranging, is one of the most important remote sensing techniques used nowadays in studying the atmosphere. Normally, a lidar consists of a transmitter, a receiver, and a data acquisition and control system. The transmitter includes a pulsed laser and some optics. The transmitted laser is designed to be in certain frequency, which depends on what atmospheric parameters are acquired, and usually equipped with high energy to ensure data quality and small divergence. The receiver contains an optical telescope, a photon detector, and some filters. Backscattered photons in the lidar system are applied to retrieve the atmospheric parameters. The sodium lidar employed in this study measures sodium density, temperature, and winds, based on resonance fluorescence scattering. Resonance fluorescence is a process in which the energy of an incoming photon (from the laser) coincides with the energy of a transition in the level scheme of an atom, ion, or molecule (here it is the sodium atom), and is reemitted at the same or at some longer wavelength. In the lidar receiving system, only cases in which incident and scattered wave-

lengths are the same are considered. Resonance fluorescence is widely used for analytical purposes because of its high and narrow peaks of resonance lines. These properties result in high sensitivity and selectivity of the analytical procedures. The resonance process implies both absorption, or a loss, and reemission, or scattering of the primary radiation at the same time. Since the mean free path of a sodium atom in the mesopause region is less than 1 mm, the atom suffers more than 10^5 collisions in a volume with dimension of 100 m and in a time span of ~ 1 s [Krueger *et al.*, 2015]. For the temporal and spatial resolutions down to this scales, the motion of atoms is considered to be in thermal equilibrium with the ambient air. The sodium spectra are influenced by Doppler broadening and Doppler shift, which are related to the background wind and temperature. The scattering signal also depends on the sodium density. These fundamentals enable the development of Na lidar in detecting temperature, winds, and Na density simultaneously in the mesopause region. Gibson *et al.* [1979] first implemented the Doppler broadening principle in obtaining the mean temperature of sodium layer with a pulsed dye laser. Fricke and von Zahn [1985] then used an excimer-pumped pulsed laser and obtained the temperature profiles with altitude. Later, the two-frequency technique was developed by locking the seed laser to two absolute frequencies. A three-frequency technique was applied to derive temperature and wind profiles by She *et al.* [1991]. This chapter will describe the sodium lidar theory and the sodium lidar system located at Andes Lidar Observatory (ALO; 30.25° S, 70.74° W, Cerro Pachón, Chile), as well as the retrieval algorithms in the data processing.

2.1 Sodium Fluorescence Hyperfine Spectrum

To understand the narrow band Na lidar theory, it is necessary to know the laser induced Na fluorescence spectrum. A brief introduction of sodium laser spectroscopy is given here. More details can be found in She and Yu [1995]; Papen *et al.* [1995]; Chu and Papen [2005];

Krueger et al. [2015].

2.1.1 Sodium spectrum

The sodium spectrum is dominated by the bright doublet known as the Sodium D-lines at 589.1583 and 589.7567 nm (in the vacuum) as a result of the transition from 3p to the 3s energy levels, referring to D₂ and D₁ lines. Specifically, the two components are from $^2s_{1/2}$ to $^2p_{3/2}$ transition and $^2s_{1/2}$ to $^2p_{1/2}$ transition for D₂ and D₁, respectively. The D₂ transition is more relevant to the modern quantum and optics experiments, because it has a cycling transition that is used for cooling and trapping sodium, also because it has twice the intensity of D₁ line.

The doublet fine structure is from the coupling between an electron's orbital and spin angular momentums. Besides the two dominate transitions, each transition additionally has a hyperfine structure, which arises from the coupling between the total electron angular momentum and total nuclear angular momentum. Shown in Figure 2.1 is the full model for the sodium D transitions including both fine and hyperfine structures for D₁ and D₂ lines. Since the ALO narrow band sodium lidar employs the D₂ line particularly, here, the focus will be on the D₂ transition structure. The D₂ emission has a natural lifetime τ_{Na} of 16.40 ± 0.03 ns and an oscillator strength f_0 of 0.6357 [*Papen et al.*, 1995]. When the hyperfine interactions from nuclear-electron spin coupling are included, the states $^2s_{1/2}$, $^2p_{1/2}$, and $^2p_{3/2}$ then split into 2, 2, and 4 energy hyperfine levels, respectively, labeled by total angular momentum of the atom, F , with the degeneracy $2f+1$. Then the D₂ line consists of two groups of lines, D_{2a} and D_{2b}, formed by the transition from 4 $^2p_{3/2}$ split levels to 2 $^2s_{1/2}$ split levels. Among the 8 possible transitions, only 6 satisfy the selection rule for dipole radiation that $\Delta f < 2$. Although transitions of higher order are possible, the strengths of these transitions are negligible compared to the dipole terms. The center wavelength λ_0 of D₂ six transitions is 589.1583 nm. Listed in Table 2.1 are the frequencies

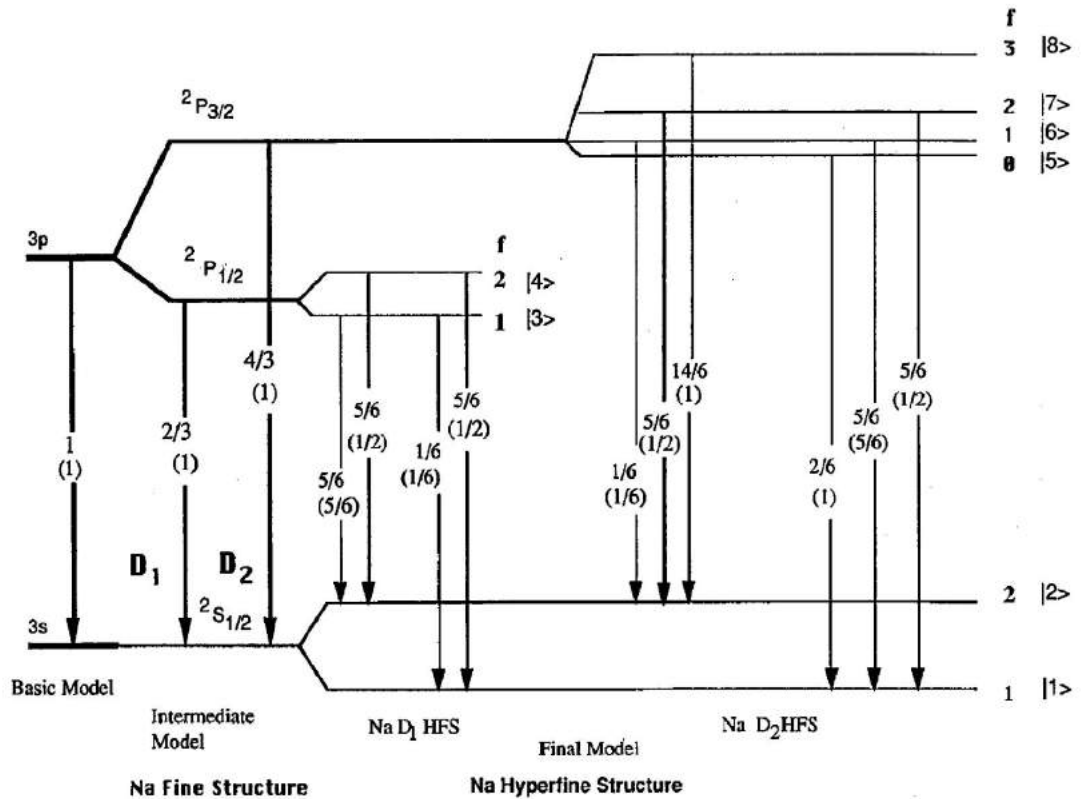


Figure 2.1: Energy level of the Na transition with frequency splitting. The basic model only includes two states, 3s ground state and 3p excited state. The electron spin causes the excited-state splits into a doublet, $2p_{1/2}$ and $2p_{3/2}$, corresponding to the D₁ and D₂ transition lines to the ground state $2s_{1/2}$, respectively. Under the nuclear spin, the states $2s_{1/2}$, $2p_{1/2}$, and $2p_{3/2}$ then split into 2, 2, and 4 energy hyperfine levels, respectively, labeled by total angular momentum of the atom, F , with the degeneracy $2f+1$. See [She and Yu, 1995]

Table 2.1: Frequencies and relative strength of sodium D₂ six transition lines.

Transition	² s _{1/2}	² p _{3/2}	Offset (GHz)	Relative Strength
D _{2a}	f = 1	f = 2	1.0911	5
		f = 1	1.0566	5
		f = 0	1.0408	2
D _{2b}	f = 2	f = 3	-0.6216	14
		f = 2	-0.6806	5
		f = 1	-0.7150	1

that relative to the center wavelength of six transitions and their relative oscillator strengths for incoherent light source.

2.1.2 Hanle effect

The Hanle effect is a reduction in the polarization of light emitted from an atom which is subject to a magnetic field in a particular direction [Hanle, 1924]. A weak magnetic field causes slow Larmor precession, so the dipoles have no time to change their orientation before they spontaneously decay. Consequently, re-emitted fluorescence preserves the polarization of the incident excitation light. On the other hand, in a high magnetic field, fast precession causes rapid averaging of the dipoles orientation, i.e., there is an efficient depolarization of the re-emitted light. Because of the polarization of laser and the magnitude of the Earth's geomagnetic field, the relative strengths should consider the interferences in the emitted light due to the Hanle effect. Thus, the intensity of six sodium D₂ hyperfine transitions could vary from Table 2.1. Zimmermann [1975] first applied the Hanle effect to determine the life time of ⁴p_{1/2} state Potassium by investigating the intensity of scattered resonance light of the potassium D₁ line as a function of magnetic field. Papen *et al.* [1995] reviewed the narrow-band sodium lidar principles and calculated the relative intensity of

Na D_2 transitions the lidar setup over the Urbana Atmospheric Observatory. The relative intensities are 5:5.5:2:15.68:5:0.98 for coherent and polarized transmitter light under zero magnetic field, which are slightly different from Table 2.1. This difference can result in a temperature bias of 1.4 K and a wind velocity bias of 0.7 m/s .

In this section, the Hanle effect is reanalyzed and applied to the ALO Na lidar system under the condition of local magnetic field. Following *Fricke and von Zahn* [1985]; *Papen et al.* [1995], the relative intensities of the hyperfine lines for Na D_2 resonance need to be considered under different viewing geometry and state of polarization of the transmitter and receiver. The transmitted light of ALO lidar is linearly polarized and coherent while the receiver is insensitive to polarization. When the laser is pointed into zenith, the angle between the direction of light propagation and the direction of the geomagnetic field vector is defined as χ . According to *Zimmermann* [1975]'s notation, χ is $\pm 90^\circ$ for circular polarization and 0 for linear polarization. The direction of linear polarization is given by α with respect to the magnetic north-south direction. Under the Earth's magnetic field, χ is also related to the inclination I of the geomagnetic field by $\chi = I + 90^\circ$. Assuming the magnetic field is B , the relative intensities evaluated from eq. (6) in *Zimmermann* [1975] for a linearly polarized lidar are summarized by *Fricke and von Zahn* [1985] as:

The magnetic field over ALO retrieved from NCEI Geomagnetic Calculators is listed in Table 2.3. The total field is around 22.64 μT almost in the direction of north-south. The inclination and declination angles are -30.69° and 0.11° , respectively. The lidar geometry in the transmitter is in the direction of east-west. Thus, α is believed to be 90° according to Figure.A1 in *Fricke and von Zahn* [1985]. The recalculated relative intensities based on Tables 2.2 and 2.3 are shown in Table 2.4 under the condition that no external magnetic field is considered ($\mathbf{B}=0$).

Compared with Table 2.1 and the results from *Papen et al.* [1995], it is clear that the influence of local magnetic field is nearly the same as other sites. However, the Hanle effect

Table 2.2: Relative intensity of sodium D₂ six transition lines for a linearly polarized lidar.

Transition	² s _{1/2}	² p _{3/2}	Relative Strength
D _{2a}	f=1	f=2	$5 + 0.2283 \cdot 10^8 \cdot B^2$
	f=1	f=1	$5.5 - 3 \cdot \sin^2 I \cdot \cos^2 I \cdot (1 + \cos(2\alpha))$ $+ 0.2867 \cdot 10^4 \cdot \sin I \cdot \cos^2 I \cdot \sin(2\alpha) \cdot B$ $+ \{0.2511 - \cos^2 I \cdot [0.0137 \cdot (1 - \cos(2\alpha))$ $+ 0.1096 \cdot (1 + \cos(2\alpha)) \cdot \sin^2 I]\} \cdot 10^8 \cdot B^2$
	f=1	f=0	$2 + 0.0913 \cdot 10^8 \cdot B^2$
D _{2b}	f=2	f=3	$15.68 - 10.08 \cdot \sin^2 I \cdot \cos^2 I \cdot (1 + \cos(2\alpha))$ $+ 0.9633 \cdot 10^4 \cdot \sin I \cdot \cos^2 I \cdot \sin(2\alpha) \cdot B$ $+ \{0.7160 - \cos^2 I \cdot [0.0460 \cdot (1 - \cos(2\alpha))$ $+ 0.3682 \cdot (1 + \cos(2\alpha)) \cdot \sin^2 I]\} \cdot 10^8 \cdot B^2$
	f=2	f=2	$5 + 0.2283 \cdot 10^8 \cdot B^2$
	f=2	f=1	$0.98 + 0.12 \cdot \sin^2 I \cdot \cos^2 I \cdot (1 + \cos(2\alpha))$ $- 0.0115 \cdot 10^4 \cdot \sin I \cdot \cos^2 I \cdot \sin(2\alpha) \cdot B$ $+ \{0.0447 - \cos^2 I \cdot [0.0460 \cdot (1 - \cos(2\alpha))$ $+ 0.0044 \cdot (1 + \cos(2\alpha)) \cdot \sin^2 I]\} \cdot 10^8 \cdot B^2$

Table 2.3: Earth's geomagnetic field over Andes Lidar Observatory, Cerro Pachón, Chile. Data is retrieved from NOAA' Geomagnetic Calculator.

Model used: World Magnetic Model (WMM)					
Latitude: 30.25° S					
Longitude: 70.74° W					
Elevation: 90 km above sea level					
Date	Declination	Inclination	North Comp	East Comp	Total Field
2017-04-07	0.1054°	-30.6878°	19,465.4 nT	35.8 nT	22,635.2 nT

Table 2.4: Relative strength of sodium D₂ six transition lines with Hanle effect.

Transition	² s _{1/2}	² p _{3/2}	Relative Strength (B=0)	Relative Strength (B=ALO)
D _{2a}	f =1	f=2	5.0	5.0117
		f=1	5.5	5.5118
		f=0	2.0	2.0047
D _{2b}	f =2	f=3	15.68	15.7132
		f=2	5.0	5.0117
		f=1	0.98	0.9823

will induce measurement errors for temperature and wind, which needs to be considered in lidar data analysis. In the next section, the bias caused by ignoring Hanle effect will be discussed with ALO data.

2.1.3 Effective scattering cross section

The lifetime for excited state of a Na atom is about 16 ns and their natural linewidth is $1/(2\pi\tau) \simeq 10$ MHz. This is the absorption line of Na due to natural broadening that arises from the uncertainty in energy of the states involved in the transition. Natural broadening is homogeneous and in a Lorentzian lineshape defined as:

$$g_H(v, v_0) = \frac{\Delta v_H}{2\pi \left[(v - v_0)^2 + (\Delta v_H/2)^2 \right]}, \quad (2.1)$$

where Δv_H is called the homogeneous broadened linewidth. Due to the low pressure in the mesopause region, the broadening caused by the collisions between atoms and molecules is negligible [Yu and She, 1995; Chu et al., 2005]. Doppler broadening is the broadening of spectral lines due to the Doppler effect caused by a distribution of velocities of atoms. Different velocities of the emitting particles result in different Doppler shifts, the cumulative effect of which is the line broadening. The velocity distribution, or the Doppler broaden-

ing, is temperature dependent and determined by Maxwell-Boltzmann distribution under the sodium density of ρ , which is given by

$$\rho(v)dv = \rho \sqrt{\frac{m}{2\pi k_B T}} \exp\left(-\frac{mv^2}{2k_B T}\right) dv, \quad (2.2)$$

where $\rho(v)$ is the number density of sodium atoms with speeds between v and $v + dv$; T is the absolute temperature; m is the sodium atom mass; k_B is the Boltzmann's constant. For a typical temperature of 200 K in the mesopause region, Doppler broadening produces 1 GHz linewidth, which is much larger than the natural broadening.

The total effective cross-section σ_{eff} is defined as the ratio of the average photon number scattered by an individual atom to the total incident photon number per unit area. σ_{eff} is determined by the convolution of absorption cross-section σ_{abs} and the laser spectral lineshape $g_L(v)$. Similarly, σ_{abs} is the ratio of the averaged absorbed single frequency photons per atom to the total incident photons per area. The statistically averaged absorption cross-section for each D₂ transition is expressed as

$$\sigma_{\text{abs}}(v, v_0) = \sigma_0 \exp\left(-\frac{(v - v_0)^2}{2\sigma_D^2}\right), \quad (2.3)$$

where

v_0 : the resonance frequency of each transition line.

$\sigma_D = v_0 \sqrt{\frac{k_B T}{mc^2}}$: the rms linewidth of Doppler broadening with c as the speed of light.

σ_0 : the peak absorption cross-section.

The laser spectral lineshape can be approximated by a Gaussian lineshape with a rms width of σ_L :

$$g_L(v, v_L) = \frac{1}{\sqrt{2\pi}\sigma_L} \exp\left(-\frac{(v - v_L)^2}{2(\sigma_D^2 + \sigma_L^2)}\right). \quad (2.4)$$

The total effective cross-section for sodium D₂ hyperfine structure with a Gaussian shape is

$$\sigma_{\text{eff}}(\nu, T, \nu_R) = \frac{1}{\sqrt{2\pi}\sigma_e} \frac{e^2}{4\epsilon_0 m_e c} \sum_{n=1}^6 A_n \exp\left(-\frac{(\nu - \nu_n + \frac{\nu_R}{\lambda})^2}{2\sigma_e^2}\right), \quad (2.5)$$

where e and m_e are the charge and mass of electron, ν_n and A_n are the center frequency and relative intensity for each transition line, respectively, ν and λ are the laser frequency and wavelength, ν_R is the radial velocity of the Na atom moving away from the laser source, and

$$\sigma_e^2 = \sigma_D^2 + \sigma_L^2. \quad (2.6)$$

Eq.(2.5) demonstrates that the resonance scattering of sodium D₂ line depends on the temperature and wind velocity, where the laser beam frequency is Doppler shifted. Therefore, it is possible to derive the temperature and wind with appropriate design for the Na lidar.

2.1.4 Three-frequency technique

By assuming the Na atoms are in equilibrium with the surrounding atmosphere, the Na temperature is equal to the atmospheric temperature. The dependence of Na resonance linewidth on the temperature and wind through Doppler broadening and Doppler shift enables the measurements of atmospheric temperature and winds in the mesopause. Figure 2.2 demonstrates the Na absorption cross section under different temperature and wind conditions. It is clear that the higher temperature, the linewidth is more broadened; the larger wind, the linewidth is more shifted.

The temperature profile at different altitudes in the mesopause region by the Na lidar technique was first obtained by *Fricke and von Zahn* [1985] with a frequency-scanning method. Later a two-frequency technique was developed by *She et al.* [1990] with the laser beam locked to the two absolute frequencies at the D_{2a} peak f_a and crossover f_c of the Na D₂ Doppler-free spectrum using a Na vapor cell. However, the two-frequency method

cannot derive the temperature, wind, and Na density at the same time. The temperature is derived under the assumption that radial wind is zero, which is Figure 2.2a. Modern Na lidar employs a three-frequency technique that can determine all three parameters simultaneously, which was first proposed by *Bills et al.* [1991]; *She et al.* [1992] and implemented in *She and Yu* [1994]. The laser frequency is tuned to three frequencies at f_a , $f_+ = f_a + \Delta f$, and $f_- = f_a - \Delta f$, where $\Delta f = 630$ MHz. Temperature and wind are derived based on the ratios between these three frequencies. The definitions of the ratios are chosen to be sensitive enough for good measurements.

2.2 ALO Lidar

The ALO Na lidar is located at Andes Lidar Observatory (ALO) in Cerro Pachón, Chile (30.3°S, 70.7°W). Since the lidar was deployed to ALO in 2009, it has been operated in terms of campaigns for 3-4 times per year maximal with about 2 weeks for each campaign. The lidar is equipped with high power and stable lasers, and is capable of measuring high resolution temperature, horizontal winds, vertical wind, and Na density at the same time. In May 2014, a major upgrade of the lidar system resulted in a significant improvement of the signals as well as the system's stability. This upgrade was followed by a replacement of the old Coherent Ring Dye Laser with a high-power amplified diode laser (TA-SHG from Topica Photonics, Inc.) as the master oscillator [*Liu et al.*, 2016]. The alignment of the lidar receiver optical system was also improved according to *Smith and Chu* [2015]. Several campaigns were conducted after the upgrade with more data acquired than all previous campaigns and with much better quality. Right now, the lidar operation can be nearly 9 hours in summer and 10 hours in winter without interruption through the entire night. Signals can reach 1000 counts per laser pulse, which is nearly five times higher than the signals before upgrade. One advantage of this upgrade is the capability of observing the

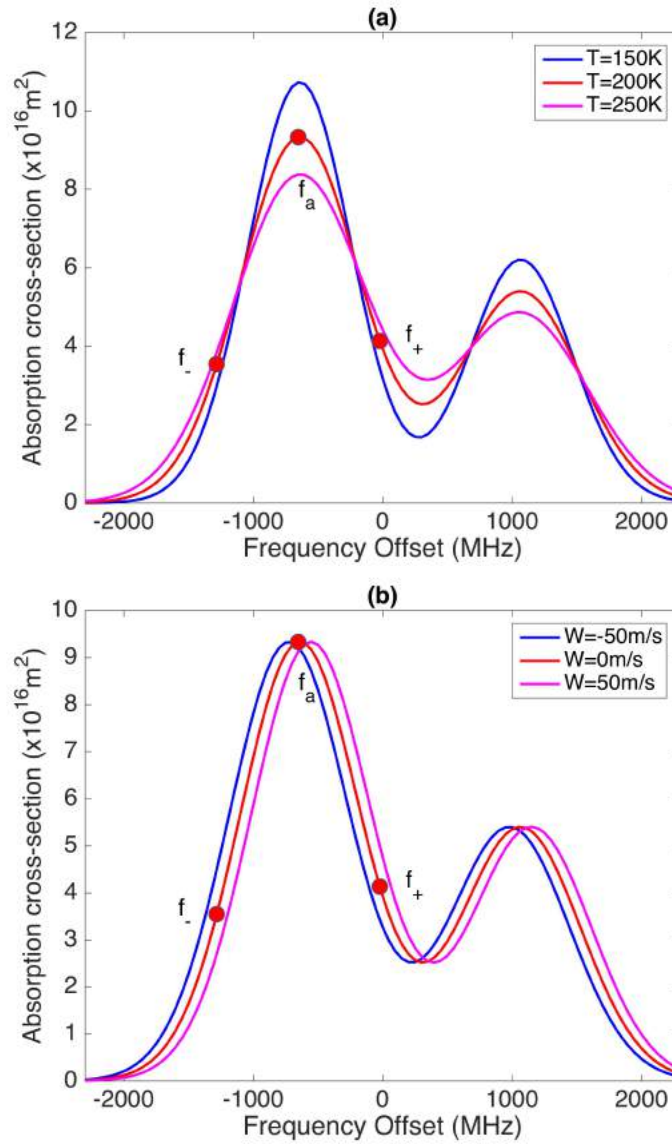


Figure 2.2: Na absorption cross section for (a) three temperatures at $v_R = 0$ and (b) three wind velocities at $T = 200\text{ K}$. The three red dots are corresponding to the three frequencies adopted in lidar system to retrieve temperature and wind.

thermospheric Na layer extended to 170 km [Liu *et al.*, 2016]. In consequence, the high signal level also causes photon counts saturation in the receiving instruments (see details in the next Chapter). This section introduces the ALO Na lidar system and presents a summary of the dataset applied to the studies in the dissertation.

2.2.1 ALO Na lidar system

Shown in Figure 2.3 is the schematic diagram of the current Na wind/temperature lidar. The system includes three main blocks: transmitting, receiving, data acquisition and control. The transmitter is to provide laser pulses with accurate frequency, high power, small divergence, and narrow-band linewidth. In the transmitter, the master oscillator is served by high-power amplified diode laser with a model of TA-SHG from Topica Photonics, which replaced the old Ring Dye Laser during the upgrade. Its output is continuous wave laser. Then a small portion of the light is sent to a Na vapor cell as Doppler-free spectroscopy used to lock the laser frequency at the D₂ line. The rest of the light is sent to an acousto-optic modulator (AOM), which achieves the cyclic operation with no shift or an up/down frequency shift to other two frequencies. The output of AOM is then transmitted to a pulsed dye amplifier (PDA) that converts the continuous wave (CW) laser beam into pulses with an average power of ~ 1.2 W. When a pumped pulse from the frequency-doubled Nd:YAG laser with wavelength of 532 nm is injected into the dye cells, the PDA will amplify the CW laser beam and produce a 589 nm laser pulse. The outgoing laser beam is pointed to the atmosphere in the directions of zenith and 20° off-zenith to measure the vertical and horizontal winds along with temperature and Na density.

The function of a receiver system is collecting the backscattered photon counts from the atmosphere. Currently the ALO lidar is coupled with four 75 cm diameter telescopes in the direction of zenith, east, south, and west. The mechanical chopper, collimation lenses, and narrow-band filters are used to prevent most of the background signals and

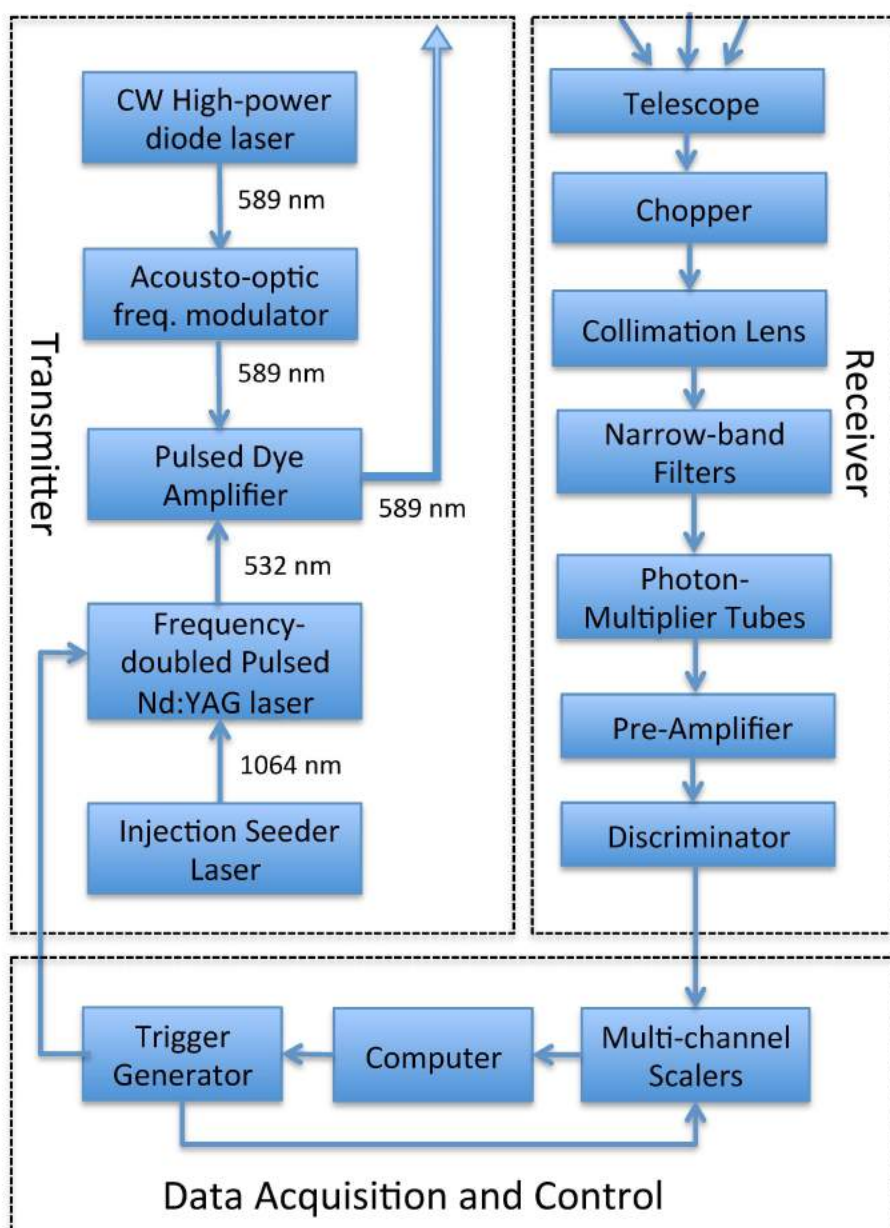


Figure 2.3: Schematic diagram of the ALO Na lidar. There are three main parts: a transmitter, a receiver, a data acquisition and system control.

the saturated signals below 15 km. The return signals at higher altitudes are counted by Photon-Multiplier Tubes (PMT). A PMT is a vacuum tube consisting of an input window, a photocathode, focusing electrodes, an electron multiplier, and an anode usually sealed into an evacuated glass tube. The PMT is a sensitive photon detection device that can count the number of incoming photons at very low levels. PMT is operated on photon counting mode in lidar system. When signal level is high, PMT experience severe nonlinearity and saturation effect, which can be corrected by using a correction function. At ALO, the model of the four PMTs used in four directions (ZSEW) was Hamamatsu H7421-40. The H7421-40 is an integrated module with a PMT, High-Voltage supply, amplifier, discriminator, thermoelectric cooler, and pulse shaper etc. It offers high quantum efficiency of over 40% at 589 nm wavelength, with a pulse-pair resolution of 70 ns. This limits the maximum count rate to be ~ 14 MHz. Starting on July 15th, 2015, the PMTs in zenith and east directions were replaced with a newer model H7421-M that has shorter pulse width and higher maximum count rate, which resulted in largely increased signals in these two directions. The incorrect calibration of PMT nonlinearity could not only influence the derivation of temperature, winds, and Na density, but also induce biases to the calculation of correlation between these parameters, such as vertical heat flux (see more details in Chapter 3).

The overall key features of the ALO lidar system are summarized in Table 2.5. The new laser power is three times higher than the Ring Dye Laser, which was 300-400 mW [Chu *et al.*, 2005].

2.2.2 Data summary

The histogram in Figure 2.4 shows the number of nights from ALO Na lidar in each month since 2009. Data collected before the upgrade is marked as old, while data after the upgrade is marked as new. Figure 2.5 shows the total hours of observations in each month including old and new data. The data before the upgrade is not high quality enough to

Table 2.5: ALO Na Lidar system parameters

Na lidar transmitter (λ @ 589.1583 nm)		
	High-power diode laser	Pulse Dye Amplifier
Model	TA-SHG Pro, Toptica Photonics	Spectra-Physics Quanta-Ray PDA
Pulse repetition rate	CW	50 Hz
Linewidth	< 500 kHz (rms)	60MHz (rms)
Output power	1.2W	1.2~1.5W

Na lidar receiver

Telescope diameter	75 cm
Field of view	1 mrad
PMT quantum efficiency	40%
Range resolution	$\Delta z \approx 25$ m

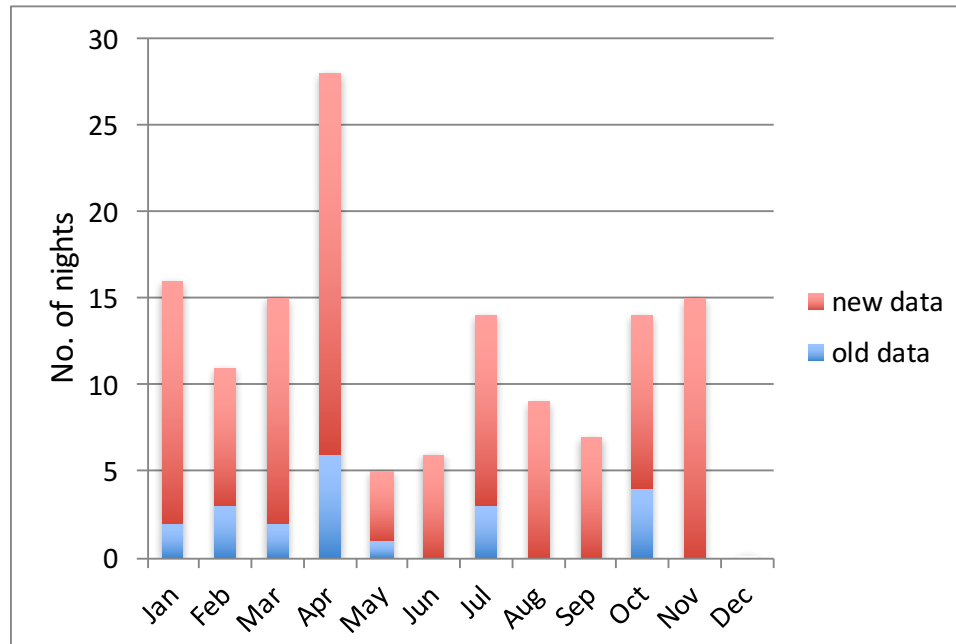


Figure 2.4: Na lidar data summary including old and new data, total number of nights is 140, with 21 nights of old data, 119 from new data. Notice that there is no data in December for now.

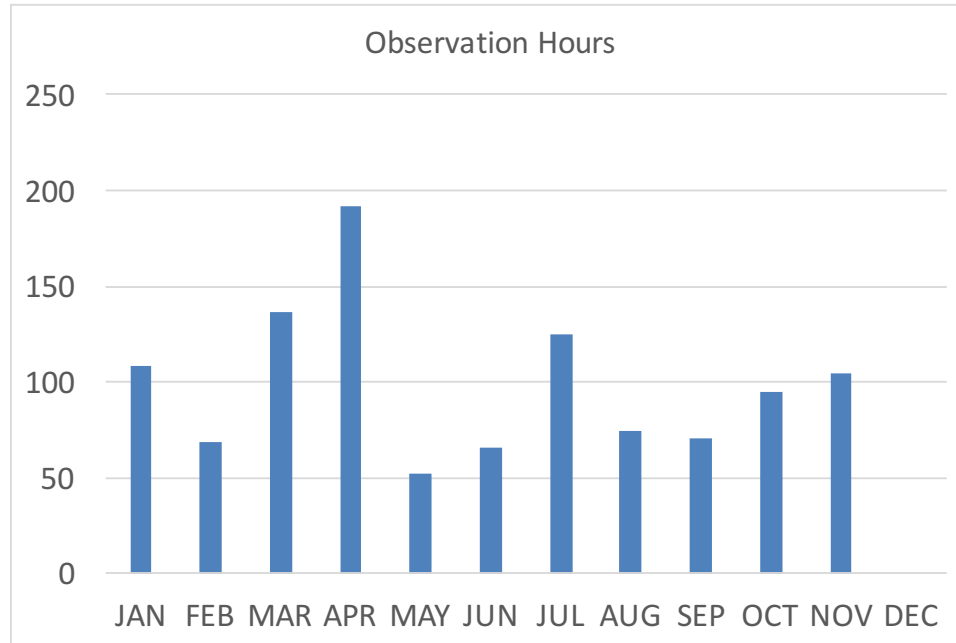


Figure 2.5: Na lidar data summary including old and new data, total number of nights is 140, with 21 nights of old data, 119 from new data. Notice that there is no data in December for now.

obtain high resolution measurements with relatively small uncertainties. Also, the nightly observation period is generally shorter than the data after the upgrade since the lidar system becomes more stable. Thus, only data after the upgrade is included and applied for heat flux calculations. Table 2.6 summarizes how lidar data was acquired and processed for all the campaigns since upgrade. The “description” column denotes the operating mode and raw data integration time. For example, “ZSZE” indicates that the sequence of directions that laser beam was pointed to is zenith-south-zenith-east, and “6s x10” means that the data was collected with 6 s integration time for each profile and 10 profiles consecutively in each direction before turning into the next direction. In data preprocessing, the raw data profiles are combined to 30, 60, or 90 seconds integration time with 500 m vertical resolution for temperature and winds derivation. This temporal and vertical resolutions are chosen so that the uncertainties of derived temperature and wind due to photon noise are acceptable.

Since this dissertation focuses on the vertical transports, only zenith measurements of

vertical wind, temperature, and Na density are chosen. For turbulence heat flux calculation, nights when the lidar was operated exclusively in zenith mode are selected.

Table 2.6: Summary of lidar operation modes and data resolutions after upgrade.

Date	Description	Processed data
May 2014	Z, 6s ; Z, 30s;	90s, 500m
Aug-Sep 2014	Z, 3s ; Z, 6s;	90s , 500m
Jan-Feb 2015	Z, 3s ; Z, 6s; ZSZE, 90S	90s , 500m
Apr 2015	Z, 6s ; ZSE, 6s x 10	60s, 500m
July 2015	ZSE, 6s x 10	60s, 500m
Oct-Nov 2015	Z, 6s ; ZSZE, 6s x 10	60s, 500m
Feb-Mar 2016	ZSZE, 3s x 10 ; ZSZE 6s x 10	30s/ 60s, 500m
June 2016	ZSZE, 3s x 10 ; ZSZE 6s x 10	30s/ 60s, 500m
Oct-Nov 2016	ZSZE 6s x 10	60s, 500m
Apr 2017	ZSZE 6s x 10	60s, 500m

2.3 Data Processing

The data processing of a narrow-band lidar with the backscattered signals collected from telescopes includes preprocessing, the procedures of retrieving temperature, winds, and Na density, which can be accomplished by solving the lidar equation, and the post-processing.

2.3.1 Lidar equation

The principle of a lidar is described by a lidar equation. The basic lidar equation relates the photon counts of the backscattered signals received at certain distance to the power of laser light originally transmitted to the atmosphere, the number density of the scattering constituent, the lidar system efficiency, and the transmission and extinction of the transmitted

and scattered signals. The lidar equation for a Na lidar is expressed as in eq. (2.7).

$$N_{Na}(z, f_L, T, v_R) = \left(\frac{P_L(\lambda_L)\Delta t}{hc/\lambda_L} \right) (\eta T_a^2(\lambda)) (\rho_{Na} \sigma_{\text{eff}}(f_L, T, v_R) \Delta z) \left(\frac{A}{4\pi z^2} \right) E^2(\lambda, z) + N_B \quad (2.7)$$

where

$N_{Na}(z, f_L, T, v_R)$: photon counts received by telescope between the range interval $(z - \Delta z/2, z + \Delta z/2)$

z : altitude (m)

f_L : transmitter laser frequency

T : temperature

v_R : radial wind velocity along the laser beam

P_L : laser power

h : Planck's constant

c : speed of light

λ_L : laser wavelength

Δt : integration time

Δz : range resolution

η : system efficiency

A : receiving telescope aperture area (m²)

ρ_{Na} : sodium number density (m⁻³)

T_a^2 : two-way atmospheric transmittance below Na layer

σ_{eff} : sodium effective cross section (m²)

$E^2(\lambda, z)$: extinction coefficient due to the absorption of Na layer

N_B : photon counts in Δz and Δt due to background noise and dark counts

The first term on the right side of the equation represents the total photon counts of the transmitted laser per pulse, in which $P_L \Delta t$ is the total laser energy and hc/λ is the energy

for a single photon. The second term is the probability that transmitted photon counts get attenuated by the aerosol and atmospheric molecules below the Na layer. The third term and fourth terms are the probability of scattering and the fraction of backscattered photon counts collected by the telescope. The last term denotes the extinction of photon counts due to the absorption in the Na layer.

Because the lidar efficiency and other parameters are difficult to determine, it is impossible to resolve eq.(2.7) directly. The common solution is normalizing the Na signals by the Rayleigh signals to obtain a relative density profile first, then calibrating it to absolute density by the atmospheric density retrieved from observations or atmospheric models at the Rayleigh reference altitude. The received Rayleigh signal at lower altitudes is

$$N_R(z_R, \lambda) = \left(\frac{P_L(\lambda_L)\Delta t}{hc/\lambda_L} \right) (\eta T_a^2(\lambda)) (\rho_a \sigma_R(\pi, \lambda) \Delta z) \left(\frac{A}{z_R^2} \right) + N_B, \quad (2.8)$$

where N_R is the Rayleigh signal, ρ_a is the atmospheric number density, z_R is the reference altitude, which is normally chosen in the region that is free of aerosol particles to avoid strong Mie Scattering, typically above 30 km. σ_R is the Rayleigh backscattering cross section.

The fluorescence scattering form of Na, σ_{eff} , has been discussed in detail in the previous section as eq.(2.5). Rayleigh scattering is an instantaneous scattering process with the incident light frequency same as the backscattered light. In eq.(2.8), $\rho_a(z) \sigma_R(\pi, \lambda)$ is defined to be the Rayleigh volume backscatter coefficient $\beta(\pi, \lambda, z)$. If θ is the scattering angle, then $\theta = \pi$ represents backscattering. Since Rayleigh scattering is anisotropic, the volume angular scattering coefficient $\beta(\theta, \lambda, z)$ is related to the volume total scattering coefficient $\beta_T(\lambda, z)$ through a phase function $P(\theta)$ as

$$\beta(\theta) = \frac{\beta_T}{4\pi} P(\theta), \quad (2.9)$$

where the phase function is given by

$$P(\theta) = 0.7629 \times (1 + 0.9324 \cos^2 \theta). \quad (2.10)$$

The Rayleigh volume total scattering coefficient is expressed through atmosphere temperature and pressure to be

$$\beta_T(\lambda, z) = 9.807 \times 10^{-23} \left(\frac{273}{T(z)} \right) \left(\frac{P(z)}{1013} \right) \frac{1}{\lambda^{4.0117}}. \quad (2.11)$$

where P and T are atmospheric pressure and temperature. The Rayleigh backscattering cross section $\sigma_R(\pi)$ at sodium lidar laser frequency 589.158 nm is 4.06×10^{-32} m²/sr, scaled from the value for 532 nm [She, 2001; Krueger *et al.*, 2015], which is applied directly to the ALO lidar data analysis.

The ALO Na lidar laser is tuned to three frequencies at f_0 (or f_a), $f_+ = f_0 + \Delta f$, and $f_- = f_0 - \Delta f$ in sequence with an period of 3 s, where $\Delta f = 630$ MHz. The corresponding photon counts in the Na layer are N_0^{Na} , N_+^{Na} , and N_-^{Na} for three frequencies with background subtracted. N_0^{Na} , N_+^{Na} , and N_-^{Na} are then normalized to the Rayleigh signal at z_R through

$$N_{\text{norm}}(f) = \frac{N_{Na}(f, z, t)}{N_R(f, z_R, t) E^2(f, z)}, \quad (2.12)$$

which gives $N_{\text{norm}}(f_0)$, $N_{\text{norm}}(f_+)$, and $N_{\text{norm}}(f_-)$. By normalizing the sodium signals to the Rayleigh signal, the undetermined parameters can be excluded in retrieving density, temperature, and winds.

The ratios applied to derive temperature and wind are defined as

$$R_T(z) = \frac{N_{\text{norm}}(f_+, z) + N_{\text{norm}}(f_-, z)}{N_{\text{norm}}(f_0, z)} \quad (2.13)$$

$$R_w(z) = \frac{\ln(N_{\text{norm}}(f_-, z)/N_{\text{norm}}(f_+, z))}{\ln(N_{\text{norm}}(f_-, z)N_{\text{norm}}(f_+, z)/N_{\text{norm}}(f_0, z)^2)}.$$

R_T and R_w are chosen to be sensitive enough to temperature and wind, respectively.

2.3.2 Lidar data analysis

Starting from the raw photon counts at three frequencies, N_0 , N_+ , and N_- , a standard preprocessing procedure is developed including the removal of bad profiles, profile combination to certain integration time, saturation correction of PMT, and background photon counts subtraction. Some criteria are employed to determine bad profiles, such as the counter-shot from Rayleigh signal (30-50 km) and Na layer (80-105 km), system power, etc. A list of the number of these files is created and designed to be skipped in further data processing. The temporal resolution of raw data is normally 6 s (some nights are 3 s), under which the photon noise is too large to retrieve the atmospheric parameters. Therefore, multiple profiles are combined into a lower temporal resolution profile, which is typically 60 or 90 s depending on the lidar operation modes.

The received photon counts from PMT can experience severe saturation effects when the return signals are high. A function can be applied to infer the incoming counts to the PMT from the output counts, which is called the PMT correction curve. Each direction is equipped with an individual PMT. Different PMTs have different correction curves. Even PMTs from the same mode may have different performance in photon counting. Thus, every PMT with an unique series number is required to be tested and calibrated. Incorrect correction of the saturation effect could induce a significant bias to temperature, wind, and Na density measurements. The background photon counts include the background noise and detector dark counts, and must be subtracted from the saturation corrected photon counts to obtain the actual counts from the sodium fluorescence backscattering. Generally the background counts are chosen in the high altitude region where Rayleigh scattering is limited because of the low atmospheric density and no Na scattering. Sometimes the background altitude range was selected to be 120-130 km, which is appropriate most of the

time since Na layer is normally observed below this region. However, thermospheric Na layers extended to ~ 170 km have been observed frequently during several campaigns over ALO [Liu *et al.*, 2016], so higher altitude is required to be considered as the background. The averaged background is only a few counts in the original acquisition time and range bin during the night, but could be 70 times higher during the daytime [Krueger *et al.*, 2015].

The key part of Na lidar data processing is the derivation of temperature, winds, and Na density. First, the preprocessed profiles are binned to certain range resolution ($\Delta r \approx 500$ m). For off-zenith directions, the vertical resolution is given by $\Delta z = \Delta r \times \cos\theta$, where $\theta = 20^\circ$ is the azimuth angle, gives a vertical resolution of $\Delta z \approx 470$ m. Second, Na layer signals are normalized to the Rayleigh signal as in eq.(2.12), where the extinction coefficient is assumed to be 1 initially. Then the ratios defined in eq.(2.13) are calculated with the 500 m and 60 s resolution profiles. Given the values of temperature and wind, the effective cross section can be calculated through eq.(2.5). Thus, it is possible to construct a two dimensional calibration curve or table relating the ratios to temperature and winds, which is the traditional method. Shown in Figure 2.6 is the curve commonly used to derive the temperature and wind. In the actual data analysis, the grids are much finer. Ratios calculated from lidar data are paired with the theoretical ratios in the curves by using a bilinear expansion in temperature and wind differences.

Instead of using the calibration curve, a more direct approach is chosen in ALO data analysis. Firstly, assume the derived temperature and wind are 200 K and 0 m/s, respectively. Then the difference between the calculated ratios from actual data and the corresponding ratios under the assumed temperature and wind is determined. Since the ratios depend on the temperature and wind, they can be written into differential forms by taking the ratios as functions of two independent variables T and w . The algorithm is described as:

1. calculate the ratios (R_{T_0}, R_{w_0}) with T and w set to 200 K and 0 m/s as T_0 and w_0 .

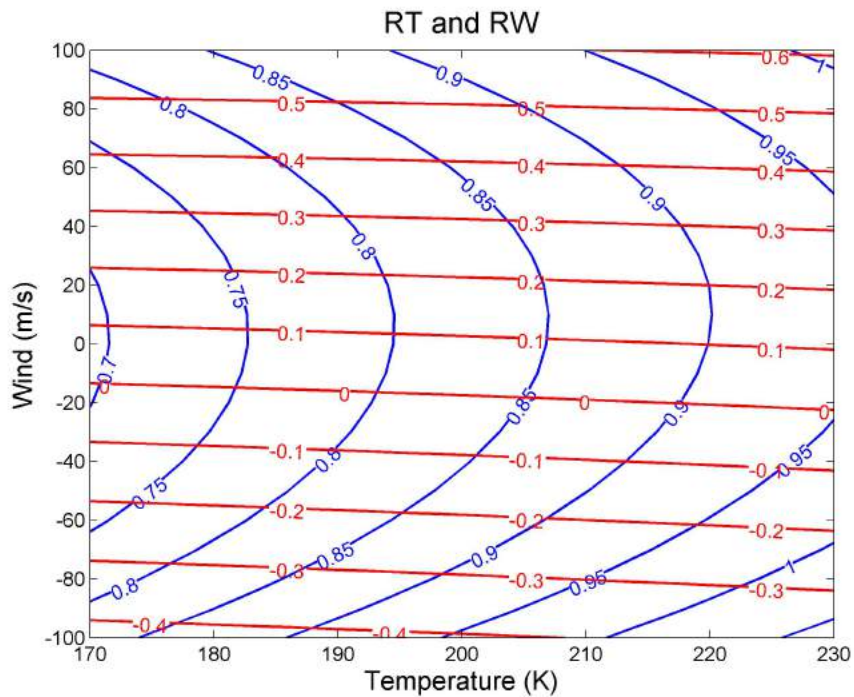


Figure 2.6: A two dimensional calibration curve presenting the theoretical ratios R_T and R_w as functions of temperature (T) and LOS wind (W). R_T and R_w are calculated theoretically from the Na fluorescence effective backscattering cross section σ_{eff} . The curves can be used to retrieve T and W from experimental ratios.

2. calculate the difference (δR_T , δR_w) between ratios from previous step (R_{T0} , R_{w0}) and ratios from lidar data (R_T , R_w).
3. use $\frac{dR_T}{dT} = \frac{\delta R_T}{\delta T}$ and $\frac{dR_w}{dw} = \frac{\delta R_w}{\delta w}$ to calculate δT and δw , where $\frac{dR_T}{dT}$ and $\frac{dR_w}{dw}$ are derived from σ_{eff} with T_0 and w_0 .
4. update T and w by $T = T_0 + \delta T$ and $w = w_0 + \delta w$.
5. repeat step 1 to 4 iteratively until both δR_T and δR_w are ≤ 0.01 .

By applying this numerical method, the retrieval is more efficient than searching from a constructed table.

Sodium density can also be derived from the preprocessed photon count profiles. It is possible to use only one frequency at the D_{2a} peak frequency f_0 , but a weighted average of all three frequencies is preferred for better estimate. The weighting coefficients are chosen to minimize the sensitivity of density measurement to temperature and wind. The weighted effective cross section is defined in *Chu et al.* [2005] as

$$\sigma_{\text{eff.wgt}} = \sigma_0 + \alpha\sigma_+ + \beta\sigma_- \quad (2.14)$$

where α and β are chosen so that

$$\frac{\partial \sigma_{\text{eff.wgt}}}{\partial T} = 0; \quad \frac{\partial \sigma_{\text{eff.wgt}}}{\partial W} = 0. \quad (2.15)$$

Then Na density is calculated through

$$\rho_{Na} = \rho_a(z_R) \sigma_R \frac{z^2 N_{\text{norm}}(f_0) + \alpha N_{\text{norm}}(f_+) + \beta N_{\text{norm}}(f_-)}{z_R^2 \sigma_0 + \alpha \sigma_+ + \beta \sigma_-}, \quad (2.16)$$

in which the normalized counts $N_{\text{norm}}(f)$ contains the two-way extinction as shown in eq.(2.12). The extinction $E^2(f, z)$ is updated iteratively.

Once temperature, wind, and Na density are derived, an additional adjustment is needed for the PDA frequency shift. For an ideal PDA, the output pulse should be a Fourier-transform-limited Gaussian lineshape centered at the frequency of CW input beam from diode laser. However, the actual spectrum of PDA output not only contains a broadened lineshape but also a shift of the central frequency, which is caused by the nonlinear effects associated with the pulsed amplification process in PDA. This nonlinear effect could be related to the optical phase distortion during the amplification [Eyler *et al.*, 1997]. The phase distortion causes the instantaneous frequency of PDA output to vary with time (which is called the frequency chirp), resulting in a broadened linewidth and a frequency shift of laser pulses. The root-mean-square (rms) of the ALO PDA output pulse is approximately 60 MHz changing from night to night, and sometimes during the night. Measuring the frequency shift precisely is crucial for wind and temperature measurements, especially for wind which is more sensitive to an absolute frequency shift. One method to measure the PDA frequency shift and chirp is developed by Colorado State University lidar group by using an iodine vapor cell [Yuan, 2004]. Here for ALO Na lidar, the nightly averaged vertical wind within 85 -100 km is calculated first. Then the necessary frequency adjustment is estimated so that the averaged vertical wind is very close to zero. This is based on the knowledge that the vertical wind component is much smaller than the horizontal winds, and its long term average magnitude is close to zero. The frequency adjustment is then applied to the data process by repeating the above steps iteratively until the calculated frequency adjustment is smaller enough and no more adjustment is needed.

The post-processing of lidar data analysis includes the interpolation of the data into fixed grids for all directions with smoothing both temporally and vertically. The temperature and Na density are interpolated for all three directions. The radial winds are converted into three wind components: zonal wind from east direction, meridional wind from south direction, and vertical wind from zenith direction. Vertical components for deriving hor-

horizontal winds are neglected because of their small amplitude. The entire data analysis is shown as a flow chart in Figure 2.7.

More details and an example of ALO data analysis can be found in Appendix A.

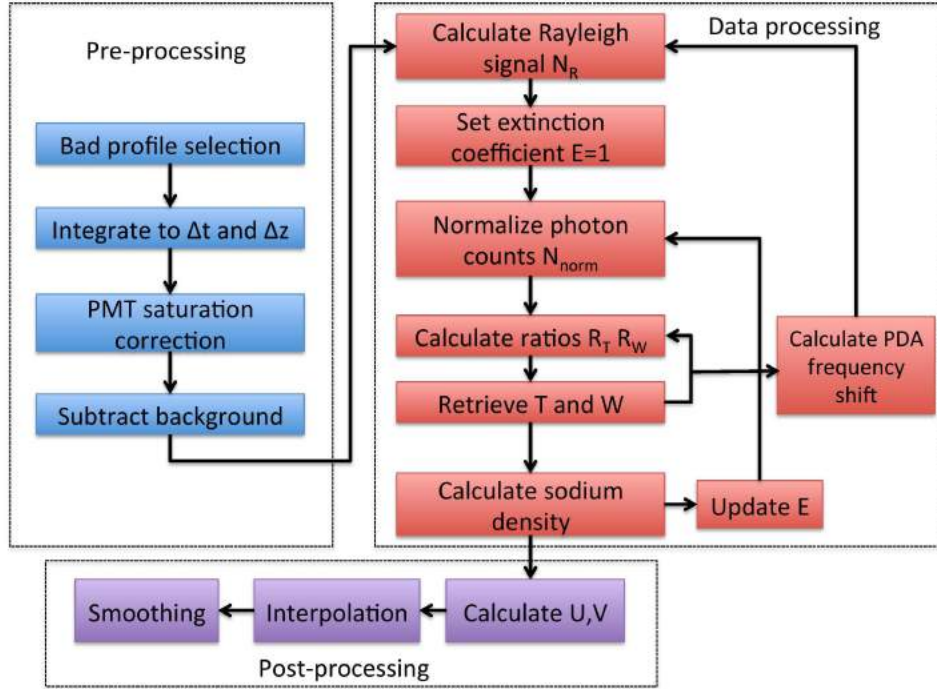


Figure 2.7: Flow chart of ALO Na lidar data processing. There are three main blocks: preprocessing, main data processing, post-processing.

2.3.3 Error analysis

The sources of measurement errors arise from two types: systematic error and random error. Systematic errors are mainly caused by the inaccurate laser frequency calibration, incorrect Na absorption cross section, imprecise laser line shape. Random errors are primarily caused by photon noise, detector shot noise, sodium density fluctuations [Chu *et al.*, 2005]. Systematic errors induce bias while random errors produce uncertainty. Here this section focuses on random error which is the dominator measurement error.

Starting from the definition of ratios R_T and R_W in eq.(2.13), the temperature error ΔT

is sensitive and related to R_T as

$$\Delta T = \frac{\partial T}{\partial R_T} \Delta R_T = \left(\frac{R_T}{\frac{\partial R_T}{\partial T}} \right) \frac{\Delta R_T}{R_T}, \quad (2.17)$$

where ΔR_T is a function of three independent variables N_0 , N_+ , and N_- . ΔR_T can be expressed as linear relations through Taylor expansion:

$$\begin{aligned} \Delta R_T &= \frac{\partial R_T}{\partial N_0} \Delta N_0 + \frac{\partial R_T}{\partial N_-} \Delta N_- + \frac{\partial R_T}{\partial N_+} \Delta N_+ \\ &= -\frac{N_+ + N_-}{N_0^2} \Delta N_0 + \frac{1}{N_0} \Delta N_- + \frac{1}{N_0} \Delta N_+ \end{aligned}$$

Then

$$\frac{\Delta R_T}{R_T} = -\frac{1}{N_0} \Delta N_0 + \frac{1}{N_- + N_+} \Delta N_- + \frac{1}{N_- + N_+} \Delta N_+$$

The rms error is defined as

$$\begin{aligned} \left(\frac{\Delta R_T}{R_T} \right)_{rms} &= \sqrt{\left(\frac{\Delta R_T}{R_T} \right)^2} \\ &\approx \sqrt{\left(-\frac{1}{N_0} \Delta N_0 \right)^2 + \left(\frac{1}{N_- + N_+} \Delta N_- \right)^2 + \left(\frac{1}{N_- + N_+} \Delta N_+ \right)^2}. \end{aligned} \quad (2.18)$$

The common statistical model for the counts of a PMT is a Poisson distribution with parameter λ equal to the square-root of the number of counts [Adamiec *et al.*, 2012], which gives $(\Delta N)^2 = N$. If we define the signal-to-noise ratio as

$$\text{SNR}(f) = \frac{N(f)}{\Delta N(f)} = \frac{N(f)}{\sqrt{N(f) + N_B(f)}},$$

$N_B(f)$ is the background counts, then eq. (2.18) becomes

$$\begin{aligned}
 \left(\frac{\Delta R_T}{R_T} \right)_{rms} &= \sqrt{\frac{N_0 + B_0}{N_0^2} + \frac{N_+ + N_- + B_+ + B_-}{(N_+ + N_-)^2}} \\
 &= \sqrt{\frac{1}{\text{SNR}_0} + \frac{N_+^2}{\text{SNR}_+(N_+ + N_-)^2} + \frac{N_-^2}{\text{SNR}_-(N_+ + N_-)^2}} \\
 &= \sqrt{\frac{1}{\text{SNR}_0} + \frac{1}{\text{SNR}_-} \frac{(N_+^2 + N_-^2)}{(N_+ + N_-)^2}} \\
 &\approx \sqrt{\frac{1}{\text{SNR}_0} + \frac{1}{2\text{SNR}_-}}
 \end{aligned}$$

Plug this into eq.(2.17) gives

$$\Delta T \approx \left(\frac{R_T}{\frac{\partial R_T}{\partial T}} \right) \sqrt{\frac{1}{\text{SNR}_0} + \frac{1}{2\text{SNR}_-}}.$$

Similar as ΔT , Δw can be written as

$$\Delta w = \frac{\partial w}{\partial R_w} \Delta R_w = \left(\frac{R_w}{\frac{\partial R_w}{\partial w}} \right) \frac{\Delta R_w}{R_w}, \quad (2.19)$$

where

$$\Delta R_w = \frac{\partial R_w}{\partial N_0} \Delta N_0 + \frac{\partial R_w}{\partial N_-} \Delta N_- + \frac{\partial R_w}{\partial N_+} \Delta N_+, \quad (2.20)$$

and

$$\begin{aligned}
 \frac{\partial R_w}{\partial N_0} &= \frac{2}{N_0} \frac{(\ln N_- - \ln N_+)}{(\ln N_+ + \ln N_- - 2 \ln N_0)^2} \\
 \frac{\partial R_w}{\partial N_+} &= \frac{2}{N_+} \frac{(\ln N_0 - \ln N_-)}{(\ln N_+ + \ln N_- - 2 \ln N_0)^2} \\
 \frac{\partial R_w}{\partial N_-} &= \frac{2}{N_-} \frac{(\ln N_+ - \ln N_0)}{(\ln N_+ + \ln N_- - 2 \ln N_0)^2}
 \end{aligned}$$

Here define a common denominator of R_w as

$$D_{R_w} = (\ln N_+ + \ln N_- - 2 \ln N_0).$$

and define

$$\ln N(-+) = (\ln N_- - \ln N_+); \ln N(+0) = (\ln N_+ - \ln N_0); \ln N(-0) = (\ln N_- - \ln N_0).$$

By using the same SNR definition, and divide eq.(2.20) by R_w , the rms is

$$\begin{aligned} \left(\frac{\Delta R_w}{R_w} \right)_{rms} &= \sqrt{\left(\frac{\Delta R_w}{R_w} \right)^2} \\ &\approx \sqrt{\left(\frac{\partial R_w}{\partial N_0} \frac{\Delta N_0}{R_w} \right)^2 + \left(\frac{\partial R_w}{\partial N_-} \frac{\Delta N_-}{R_w} \right)^2 + \left(\frac{\partial R_w}{\partial N_+} \frac{\Delta N_+}{R_w} \right)^2} \\ &\approx \sqrt{\frac{N_0 + B_0}{N_0^2} \frac{4}{D_{R_w}^2} + \frac{N_+ + B_+}{N_+^2} \frac{4 (\ln N(-0))^2}{D_{R_w}^2 (\ln N(-+))^2} + \frac{N_- + B_-}{N_-^2} \frac{4 (\ln N(+0))^2}{D_{R_w}^2 (\ln N(-+))^2}} \\ &\approx \sqrt{\frac{1}{\text{SNR}_0} \frac{4}{D_{R_w}^2} + \frac{1}{\text{SNR}_+} \frac{4 (\ln N(-0))^2}{D_{R_w}^2 (\ln N(-+))^2} + \frac{1}{\text{SNR}_-} \frac{4 (\ln N(+0))^2}{D_{R_w}^2 (\ln N(-+))^2}} \end{aligned} \quad (2.21)$$

Eqs. (2.17) and (2.19) are applied to measurement error calculations in the data analysis even in the thermospheric Na layer where Na signals are really low. The uncertainty of Na density is directly related to the photon counts. Figure (2.8) is an example of temperature and wind measurement error derived from the above equations on May 28th, 2014. In the central Na layer, the average temperature error is around 1.1 K and wind error is 1 m/s. The measurement uncertainties increase significantly when signals are low. Errors are calculated at all altitude and for each profile. Determining the error precisely is important for further data analysis.

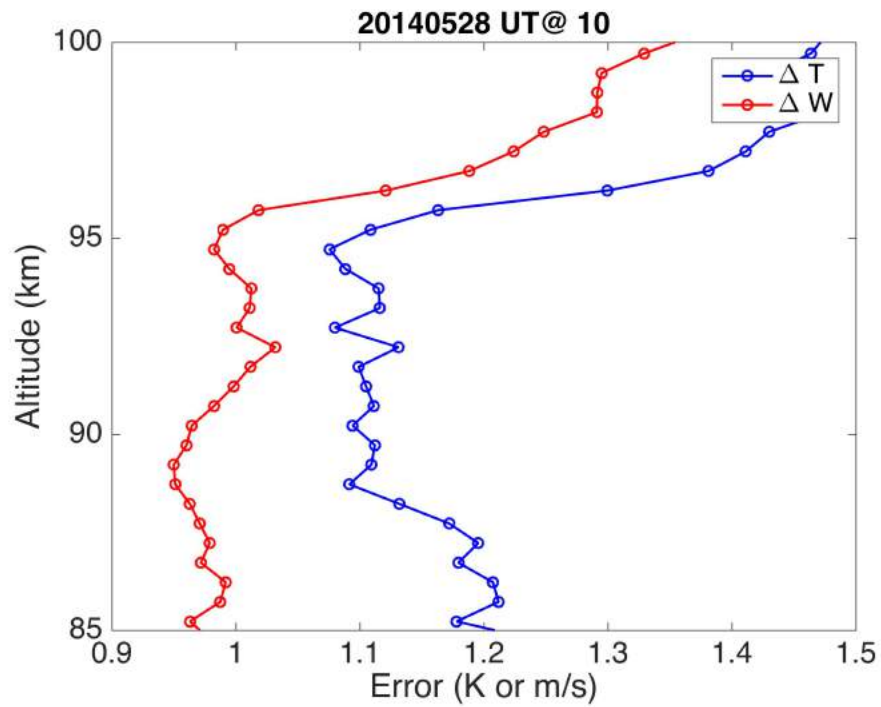


Figure 2.8: Temperature and wind measurement errors on the night of May 28th, 2014 at UT hour 10. Data was processed under the vertical and temporal resolution of 500 m and 90 s. The magnitude increases with decreasing signal levels. In the central Na layer, the average temperature error is around 1.1 K and wind error is 1 m/s.

2.4 Data Processing Updates

2.4.1 Extinction coefficient

The transmitted and backscattered photons are attenuated by the sodium layer at high altitudes and atmospheric molecules and aerosols at lower altitudes. Since the Na signals are normalized by Rayleigh signals, the attenuation caused by aerosols is neglected by chosen a Rayleigh reference altitude at around 35 km where aerosols are rare. The extinction coefficient depends on the light frequency. Previously, the upward and downward extinction coefficients are treated as the same. However, fluorescence scattering is different as elastic scattering as the backscattered light consists of six frequencies from D₂ transitions. Thus, the corresponding extinction of these backscattered photons contains the effects of different frequencies, but the upward extinction only contains the laser frequency f_L . The extinction can be characterized by the coefficient $E(\lambda, z)$ in eq.(2.22), which is defined as the ratio of the transmitted laser power to the incident laser power at the atomic Na layer.

$$E(\lambda, z) = \exp\left(-\int_{z_{\text{bottom}}}^z \sigma_{\text{eff}}(\lambda, z) \rho_{Na}(z) dz\right), \quad (2.22)$$

where z_{bottom} is the lower boundary altitude of the Na layer. In the data processing, $E(\lambda, z)$ is calculated at each altitude z considering each vertical bin Δz . The upward and downward extinction coefficient at frequency f_L and f_k can be written as

$$\begin{aligned} E_{\uparrow}(z + \Delta z, T, W) &= E_{\uparrow}(z, T, W) \exp[\sigma_{\text{eff}}(\lambda, T, W) \rho_{Na}(z) \Delta z] \\ E_{\downarrow}^k(z + \Delta z, T, W) &= E_{\downarrow}^k(z, T, W) \exp[\sigma_{\text{eff}}(\lambda_k, T, W) \rho_{Na}(z) \Delta z] \end{aligned} \quad (2.23)$$

The total effective downward extinction $E_{\downarrow}^{\text{eff}}$ can be calculated by summing $E^k(z)$ at all six frequencies weighted by a branching ratio, defined as the probability of a backscattered

photon emitted at each f_k . $E_{\downarrow}^{\text{eff}}$ is expressed to be

$$E_{\downarrow}^{\text{eff}} = \sum_{k=1}^6 \frac{\sigma_{\text{eff}}(f_k, T, W)}{\sum_{k=1}^6 \sigma_{\text{eff}}(f_k, T, W)} E_{\downarrow}^k. \quad (2.24)$$

Presented in Figure 2.9 are the derived temperature, wind, and Na density measurements with the updated extinction coefficient calculation in eq.(2.24). The plots only show a 6 km altitude range centered at the Na layer with smaller measurement errors where signals are higher (see Figure 2.8). Considering upward and downward extinction to be the same will introduce bias on the temperature and Na density measurements. The temperature is lower by an average of 0.75 K and Na density is higher by an averaged 0.54 %. For wind, the bias is too small and negligible.

2.4.2 Hanle effect bias

As mentioned earlier, the relative strength for Na D₂ transition lines are [5, 5, 2, 14, 5, 1] for incoherent and unpolarized light source. However, for Na lidar, the laser is coherent and linearly polarized, when Hanle effect is considered, the polarization of scattering light changes with external magnetic field B, as well as the relative scattering strength for Na transitions. The recalculated numbers are shown in Table 2.4 when B=0 and B at ALO. Since the dominant intensity is the transition from $F=3$ to $f=2$ with a frequency offset of 0.6212 GHz (see Table 2.1), which is close to the D_{2a} peak frequency f_0 in the three-frequency Na lidar technique, higher intensity at f_0 leads to smaller R_T and larger R_w . Therefore, it is expected that the temperature will be lower and wind be higher if Hanle effect is not included. Plotted in Figure 2.10 are the temperature and wind under three conditions mentioned above: 1) no Hanle effect, 2) with Hanle effect at B=0, and 3) B at ALO. The major difference is between (1) and (2) or (3). The influence of the Hanle effect is more obvious for temperature than wind. The averaged temperature difference for (1)

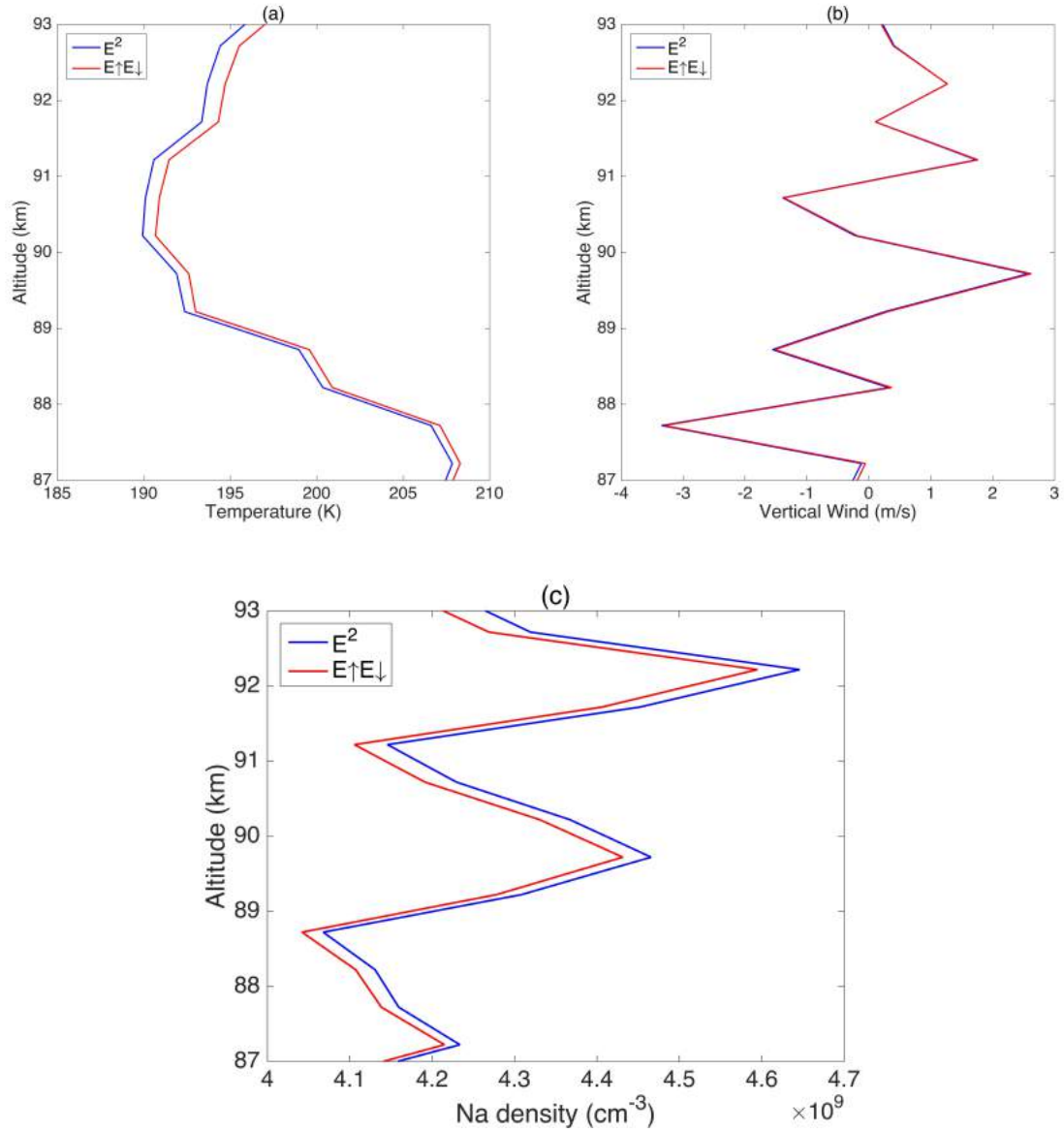


Figure 2.9: (a) Temperature and (b) vertical wind (c) Na density with updated extinction coefficient calculation. The data is on May 28th, 2014 and processed with resolutions of 500 m and 90 s. Blues lines are the results when ignoring the difference between upward and downward extinction. Red lines are the updated results calculated from eq.(2.24). The averaged biases within the this altitude range are 0.75 K, 0.03 m/s and 0.54% for temperature, wind, and Na relative density, respectively.

and (2) is -0.31 K; and 0.05 m/s for wind, same as expected. It is clear that the influence of local magnetic field is almost the same as the case with no magnetic field. Same conclusion was given in *Krueger et al.* [2015] by estimating the Hanle effect over Fort Collins with different laser configurations.

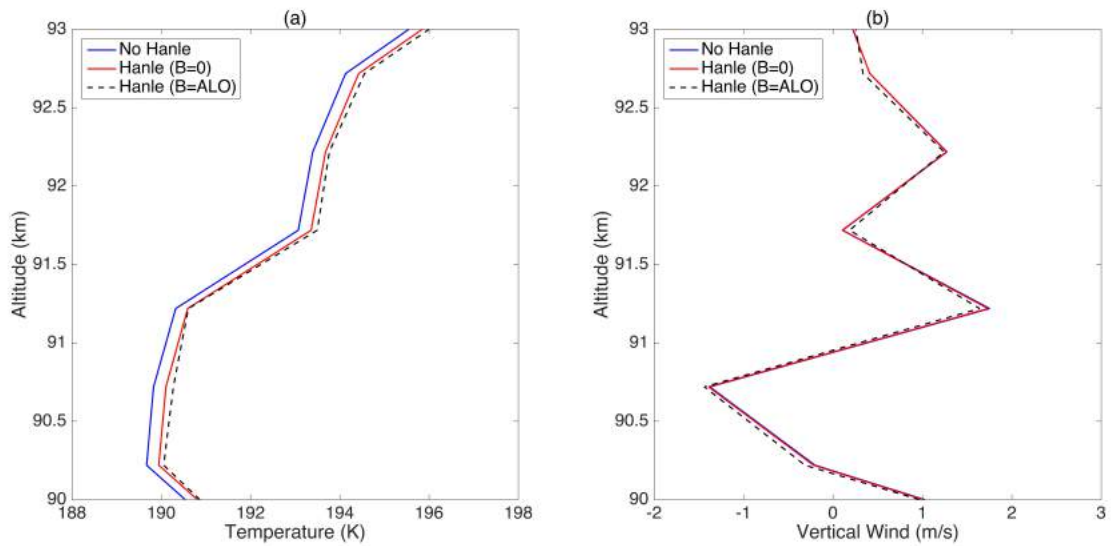


Figure 2.10: (a) Temperature and (b) vertical wind derived under three circumstances: no Hanle effect (blue solid lines), with Hanle effect when zero magnetic field ($B=0$, red solid lines) and the magnetic field at ALO ($B=ALO$, black dashed lines). The data is on May 28th, 2014 and processed with resolutions of 500 m and 90 s. The mean temperature difference for blue and red lines is -0.31 K and 0.05 m/s for wind.

Chapter 3

PMT Nonlinearity and Calibration

In this chapter, the effects of PMT nonlinearity and saturation on Na lidar measurements and heat flux calculation are studied. A method is developed to calibrate the PMT correction curve. The bias caused by the incorrect PMT nonlinearity correction is estimated both numerically and experimentally. This analysis is based upon the work by *Liu and Guo* [2016].

3.1 Introduction

As mentioned in the previous chapter, the PMT is a sensitive photon detection device that can detect low intensity light effectively. The PMT used in lidar system is normally operated on photon counting mode with wide linear range. Each photon hitting the PMT generates an electron, which is subsequently multiplied through several stages to finally generate a current pulse. The pulses are counted with a discriminator to obtain high precision measurements. However, at high signal level (higher photon incoming rate) the pulses may overlap and the discriminator cannot distinguish two or more photons arriving at nearly the same time. The output count rate from the PMT is then lower than the actual input count rate, which is called the nonlinearity of PMT. The lower limit of count rate linearity is determined by the number of dark current pulses. The maximum count rate further depends on pulse-air resolution, which is the minimum time interval at which each pulse can be separated.

At ALO, the model of the four PMTs used in four directions (ZSEW) was Hamamatsu

H7421-40. The Hamamatsu PMT model H7421-40 used at ALO has 40% QE at wavelength 589 nm, compared with 8% used during previous Maui/MALT and Starfire campaigns [Carlson *et al.*, 2005]. The pulse-pair resolution of H7421-40 is 70 ns, which gives a maximum count rate of ~ 14 MHz. The update in 2014 results in much higher signal returns. The increased signal significantly reduces the photon noise error but also leads to PMT saturation because of the relatively lower maximum count rate of H7421-40. Since then, the count rate of the backscattered photons can easily reach the severe nonlinearity and saturation range. The saturation causes the discrepancy between the actual photons received by telescopes and the photon counts PMT outputs. A laboratory measurement of this effect can determine this nonlinear relationship between input and output counts of a PMT, and such relationship is defined as saturation correction function, which can be applied to correct the PMT saturation effect.

Starting on July 15th, 2015, the PMTs in zenith and east directions were replaced with a newer model H7421-M that has shorter pulse width and higher maximum count rate, and south direction still uses old H7421-40. The correction function for H7421-40 was originally measured in UIUC for each PMT with different series number. The correction function for H7421-M was determined experimentally at university of Colorado at Boulder. Here in this study, the experimental correction functions, also referred as correction curves, are tested and calibrated with ALO lidar data from different directions. The calibration is based upon the assumption that the temperature and Na density measured in all three directions (ZSE) should have small difference, except for high frequency oscillations, because the spatial separation to zenith at around 90 km is only about 32 km, which is much smaller than the spatial scales of most low frequency variations. For zenith and east directions, they are both equipped with the new PMTs but the signal level in the east is weaker due to the longer distance between Na layer and lidar receiver and different system efficiency. Between the south and east directions, their incoming signals are comparable

but because east uses the new PMT, its temperature and Na density are considered more reliable. Based on these differences within three directions, the PMT correction curves for both old and new PMTs are adjusted (mainly in the high count rate range) from currently used curves, so the derived temperature and Na density in zenith and south directions, as well as the east direction, can match well.

Another objective is to investigate the possible bias to the heat flux calculation caused by the inaccurate PMT correction. Since the heat flux is a small quantity, care should be taken to make sure the derived heat flux is free from bias that may arise due to intrinsic correlations between T' and w' because they are all derived from the same set of signals. For example, temperature and wind errors due to photon noise are correlated, and *Su et al.* [2008] have shown that it can create a non-negligible bias in the heat flux calculation when the photon noise is large. In addition, error in the correction process can also generate a bias in the heat flux, which can be significant when the correction error is large, which is often the case at high count rates. Since the heat flux is near zero for non-dissipating waves, it is a small quantity so even a small bias can be significant. This problem was first noticed at ALO after the system upgrade in May 2014 [*Liu et al.*, 2016], which resulted in 5 to 10 times increase in signal. There have been abundance of theoretical and modeling studies of gravity wave heat flux [e.g. *Walterscheid*, 1981b; *Weinstock*, 1983; *Fritts and Rastogi*, 1985; *Liu*, 2000; *Medvedev and Klaassen*, 2003; *Becker*, 2004; *Akmaev*, 2007], and all found that dissipating gravity waves create a downward heat flux that cools the upper mesosphere. Observational evidence is less, due to the challenges in the heat flux measurement, but earlier studies from lidar measurements [*Gardner and Yang*, 1998; *Gardner and Liu*, 2007] all showed that the heat flux is indeed downward in the mesopause region (more details about gravity wave heat flux can be found in the next chapter). The heat flux measured at ALO was negative using the data before the upgrade when the signals were low, but became positive when using the high signal data after the upgrade. This discrepancy motivates this

study of the effect of PMT correction error on the heat flux calculation.

In this chapter, the relationship between the PMT correction errors and the heat flux bias is estimated quantitatively, which can be used as a guideline for future heat flux calculations. The calibrated PMT correction curves are applied for heat flux calculation with ALO data. The results are consistent with our theoretical analysis of the bias, and clearly demonstrate the existence of the bias in the heat flux due to PMT correction errors, as well as the validity of the PMT calibration process using observational data. The improved heat flux after the PMT calibration is consistent with theoretical predictions. A brief introduction of PMT nonlinearity and the correction curves is given in Section 3.2. Section 3.3 introduces a method to calibrate the PMT correction curves based on observational data, and demonstrates that with revised correction curves, the calculated heat flux indeed becomes negative. In section 3.4, numerical simulation is used to quantify the heat flux bias for idealized sinusoidal oscillations of temperature and vertical wind at different count rates and heat flux magnitudes. The results are summarized in section 3.5.

3.2 PMT Nonlinearity

3.2.1 Correction curves

Under the nonlinear circumstance, a correction formula or a curve, which relates the input and output count rate, is needed to obtain the actual counts into the PMT from the counts output from the PMT signal. The correction function given by Hamamatsu for PMT H7421-40 series is

$$N = \frac{M}{1 - M \times p}, \quad (3.1)$$

where p is the pulse-pair resolution, which is 70 ns for H7421-40, N is the true count rate and M is the measured count rate. This theoretical curve is only a reference and can only

be used when M and N are small. Each individual PMT response is different. The original correction curves of the old PMTs were determined through measurement performed at University of Illinois at Urbana-Champaign (UIUC). The nonlinear correction curve for the new H7421-M PMT was initially measured by John Smith at University of Colorado at Boulder.

Figure 3.1 shows the correction curves of the PMTs that have been applied to ALO lidar data processing, which related the output (measured) count rate with the input (true) count rate for the Hamamatsu H7421-40 series PMTs. The thin black line indicating the linear relationship is plotted for reference. The red solid line is for a newer model H7421-40-M; blue solid line is for the old PMT model H7421-40. H7421-M has larger dynamical range and maximum count rate compared with H7421-40.

It is clear that the amount of correction increases with the count rate. At large count rate, the correction amount can be very large. For example, with the ‘Old PMT’ curve (blue solid line), the input count rate of 15 MHz is corrected to near 60 MHz, an almost 300% increase. Such a huge correction is bound to have large uncertainty. A reasonable specification of the error is a constant percentage of the total correction amount. For a fixed time interval, the count rate is equivalent to the photon count. If the true photon count input to the PMT is N_{in} , and PMT output is N_{out} , the correction amount is then $\delta N = N_{in} - N_{out}$ and is always positive. The error is specified as a percentage of δN . Figure 3.1 shows two example curves (dashed lines) with $\pm 10\%$ errors. To simplify the discussion, we will refer to the PMT output count rate simply as count rate, and when not specified, it always refers to the count rate at the peak frequency.

3.2.2 Effect of PMT correction error

The inaccuracy in the PMT correction curve will introduce errors in the derived temperature and wind. To examine this effect, temperature and wind errors are calculated as a

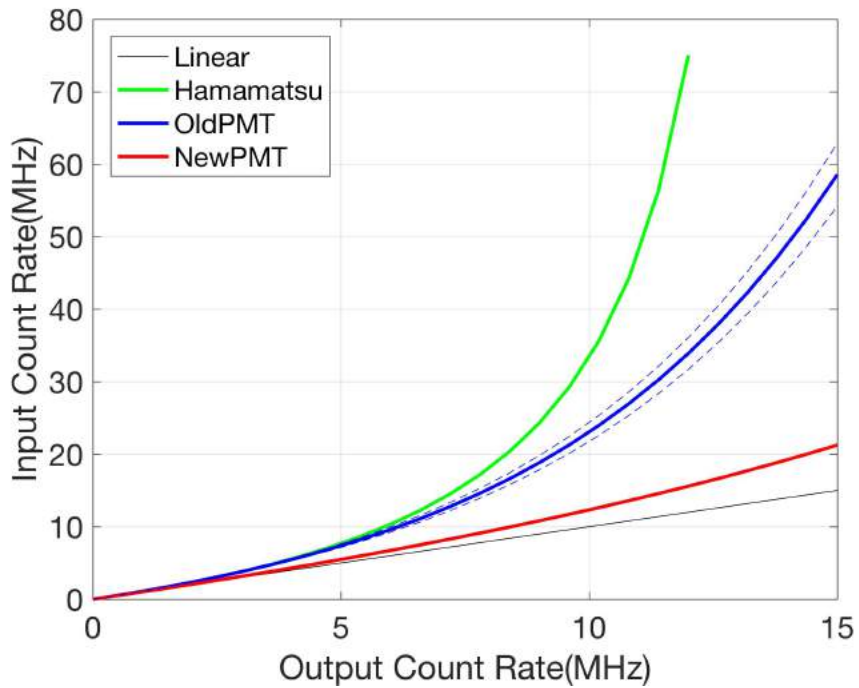


Figure 3.1: Old and new PMT correction curves. Green line is the Hamamatsu theoretical curve for an old PMT. Blue and red solid lines are laboratory measured corrections for old and new PMTs, respectively. Black line indicates linear response. Dashed lines indicate $\pm 10\%$ error on the correction amount.

function of the correction errors, represented as a percentage described in Figure 3.1, for both old and new PMTs. The photon count at f_0 is specified as a constant N_0 , assumed to be accumulated from 1000 laser shots at 6 MHz range gate, thus the corresponding count rate is $N_0/1000 \times 6$ MHz. The corresponding photon counts at f_+ and f_- , N_+ and N_- , are calculated based on T_0 and W_0 and the effective cross section σ_{eff} by using the ratios eq.(2.13), which represent the true photon counts or input photon counts of PMT. T_0 and W_0 are set to be 200 K and 0 m/s, respectively. The output photon count N^* is calculated based on the blue or red solid lines in Figure 3.1 with N for each frequency. N^* is considered as the PMT output photon counts that are subjected to the nonlinearity effect. They are then converted back to input photon counts using the same curve but with errors added (e.g. blue dashed lines).

Temperature and wind are calculated based on the newly converted photon counts at three frequencies and compared with T_0 and W_0 to obtain their biases. Figures 3.2 and 3.3 show these biases as functions of percentages of the correction errors and the count rate ($N_0^*/1000 * 6$ MHz).

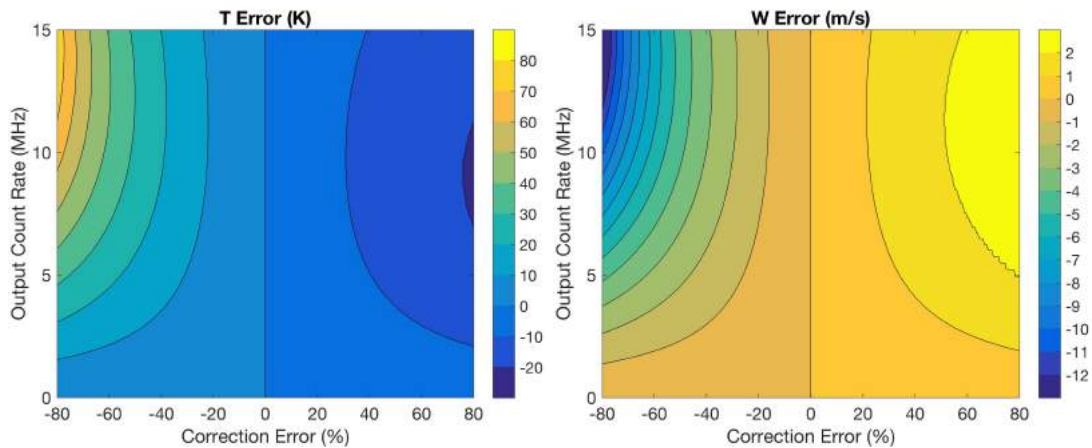


Figure 3.2: Temperature (left) and wind (right) errors as functions of the percentage of the PMT correction error (abscissa) and the count rate (ordinate) for the old PMT.

The signs of the temperature and wind biases can be understood from the relative errors

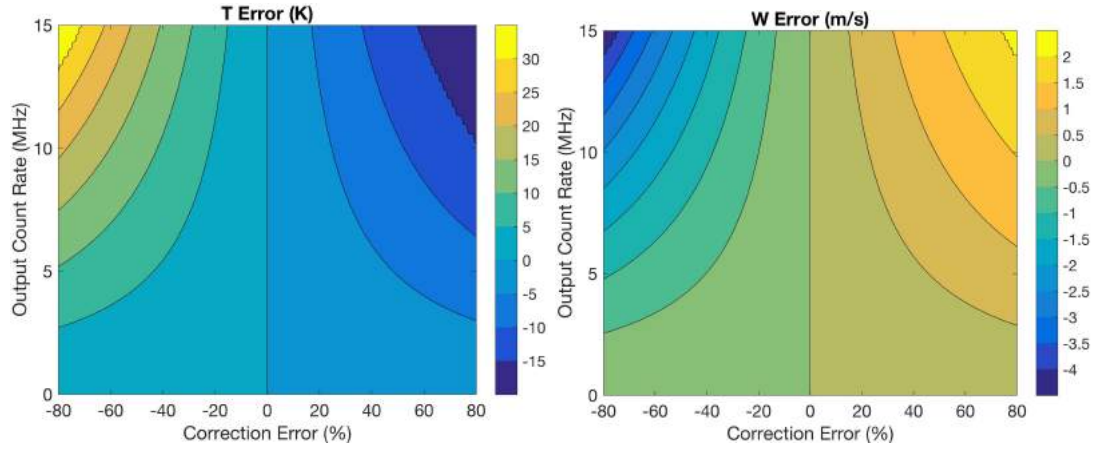


Figure 3.3: Same as Figure 3.2 but for the new PMT.

in the peak and side frequencies. Since N_+ and N_- are less than N_0 , they have smaller absolute correction amounts and smaller absolute errors. When there is an over correction (positive correction error), more positive error occurs in N_0 than in N_+ and N_- , which is equivalent to a narrower D2a spectral line, resulting in a negative temperature bias. With the same argument, since $N_+ > N_-$ (see Figure 2.2), there is more positive error in N_+ than in N_- , which is equivalent to a positive shift of the D2a line, inducing a positive bias in the wind. The opposite happens when there is an under correction (negative correction error). Figures 3.2 and 3.3 show that the magnitude of bias generally increases with count rate, as the nonlinear effect becomes more severe and the absolute correction amount becomes larger. Because of the larger difference between N_0 and N_{\pm} than between N_+ and N_- , the bias is larger in temperature than in wind. For example, for the old PMT, at 6 MHz peak frequency count rate, the biases are -8.5 K ($+11.0$ K) in temperature but only 1.0 m/s (-1.4 m/s) in the wind for PMT correction error of 30% (-30%). The temperature and wind biases are also larger for negative correction errors than for positive correction errors.

This calculation assumes that the errors in the PMT correction curve have the same percentage at all count rates. This is a reasonable assumption but is certainly not exact because the error depends on how well this correction curve is measured at different count

rates. The errors also depend on the temperature and wind, because they affect the effective cross section. Further calculations (not shown) indicate that, compared with the biases at 200 K and 0 m/s, positive (negative) wind has larger (smaller) wind bias but negligible difference in the temperature error; higher (lower) temperature has larger (smaller) bias in both temperature and wind. The PMT correction error also affects the calculated Na density. Since Na density is directly proportional to the photon counts, the two errors are also proportional to each other.

3.3 Correction of ALO Measurements

3.3.1 Evidence of error in PMT correction

The operation mode of the Na lidar at ALO is to sequentially point the laser to zenith, 20° off-zenith to south and east in a sequence, with 60 or 90 sec integration time in each direction to obtain photon count profiles used to derive temperature and line-of-sight wind. In recent ALO lidar campaigns, the PMTs used in the lidar system are the new H7421-M in east and zenith directions, and the old H7421-40 in the south direction. This provides an opportunity to cross-calibrate the PMT correction curves based on measurements from different PMTs at different signal levels.

To demonstrate the necessity for calibrating the PMT nonlinearity correction, the data on the night of November 6th in 2015 is chosen. The originally derived Na density and vertical wind measured in zenith are shown as Figure 3.4, and measured temperatures in three directions as Figure 3.5. These are derived with the corresponding PMT correction curves shown in Figure 3.1. On this night, there was a sporadic Na layer between 90-95 km during 2-4 UT. The Na density in this region exceeds 15000 cm^{-3} , much higher than the background density of about 4000 cm^{-3} . The high signals received from this

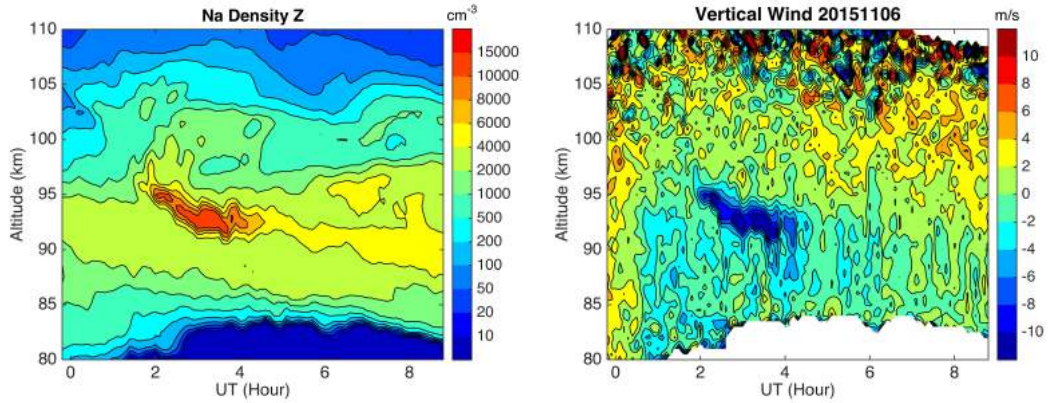


Figure 3.4: Na density (left) and vertical wind (right) in the zenith direction measured on the night of 6 November 2015. Data is processed in 60 s temporal and 500 m vertical resolutions, then smoothed with 15 min and 0.5 km full width hamming windows.

sporadic layer resulted in high PMT output count rate, therefore strong PMT nonlinearity. The temperature at zenith shows a large positive anomaly and a large negative anomaly appeared in vertical wind in the same region. These are consistent with an under correction (negative error) of the new PMT curve, which would result in positive temperature error and negative wind error (see Figure 3.2). In the south direction, there is a small negative temperature anomaly in the same region (compared with that from east), which suggests an over correction of the old PMT curve.

3.3.2 Calibration of PMT correction curve

The calibration is based on the assumption that the temperature measured in all three directions (ZSE) should be similar at large vertical and temporal scales, because the spatial separation between zenith and off-zenith directions at around 90 km is only about 32 km, much smaller than the spatial scales of most low frequency variations. Therefore, temperature is selected as the calibration quantity since it is more sensitive to the nonlinear correction than the wind (see e.g. Figure 3.3). Between the zenith and east directions, which are both equipped with the new PMTs, the measurement error caused by PMT cor-

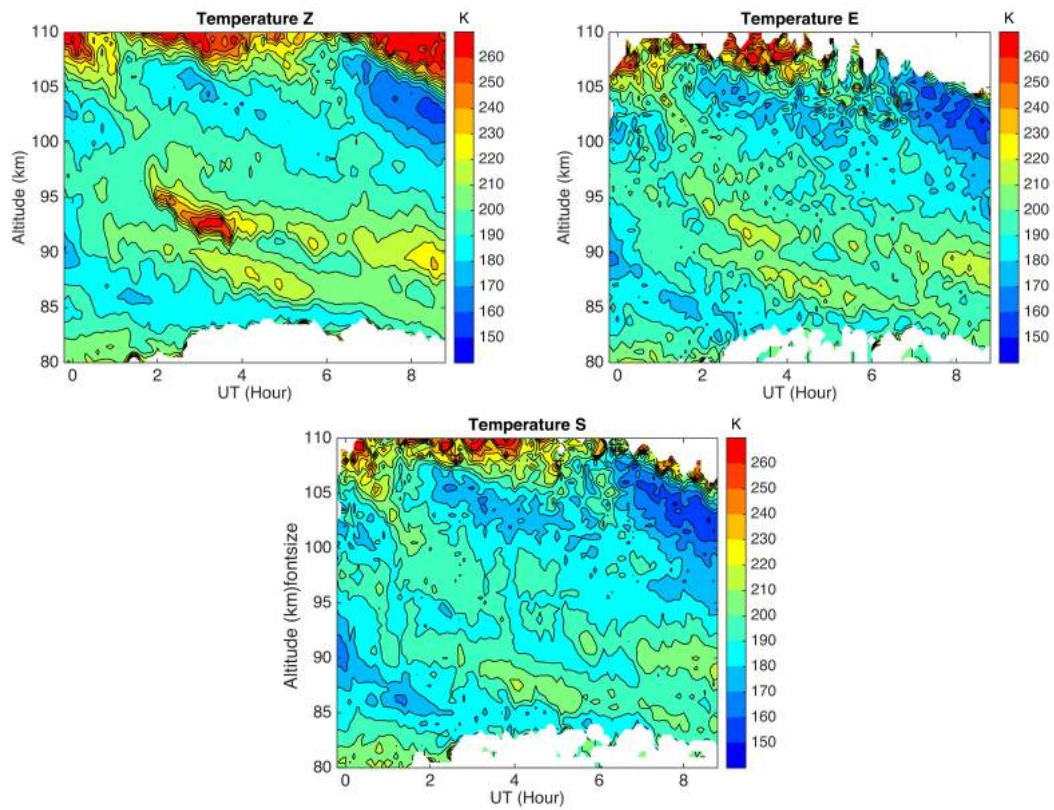


Figure 3.5: Same as Figure 3.4 but for temperatures in zenith (left), east (middle) and south (right) directions.

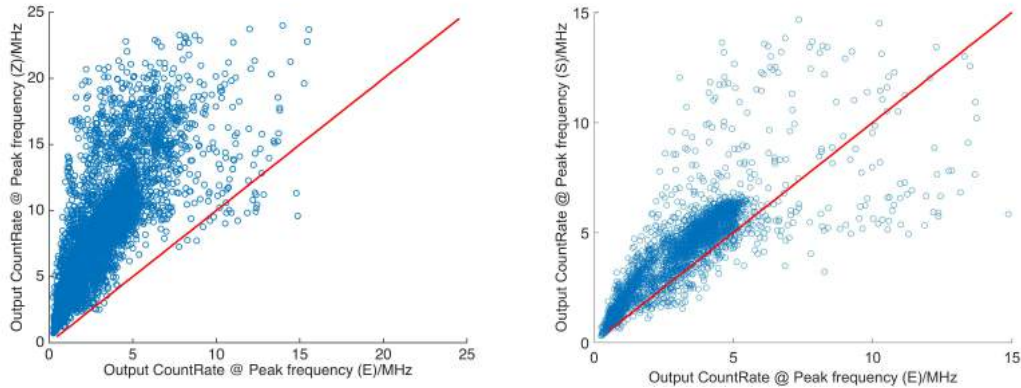


Figure 3.6: Scatter plots of the count rate at zenith vs. at east (left) and at south vs. at east (right) for same altitudes and times.

rection is smaller in east because the signal level in the east is weaker mainly due to the longer distance from the Na layer to the receiver. Between the south and east directions, the east direction is also more reliable because the PMT in the south is the old model that has stronger nonlinear effect and the signal from east is also slightly smaller due to better alignment at south. These signal differences are clearly shown in Figure 3.6, which depicts scatter plots of the PMT count rates at the same time and altitude between zenith and east and between south and east on November 6th 2015.

Therefore, we consider the east direction measurements as correct, and examine the temperature difference between zenith and east, and between south and east. Figure 3.7 shows scatter plots of the temperature difference of zenith minus east, and south minus east, as functions of the output count rate at peak frequency. These are based on the measurements between 85-100 km, at 500 m, 1 min resolutions. It is clear that there is a positive error in zenith and negative error in south, and the temperature error increases with increasing count rate. This is again a clear indication that there are PMT correction errors in zenith and south.

In order to remove the temperature errors indicated from the scatter plot trends, an exponential curve is fitted to both scattered plots to obtain an analytical relationship between

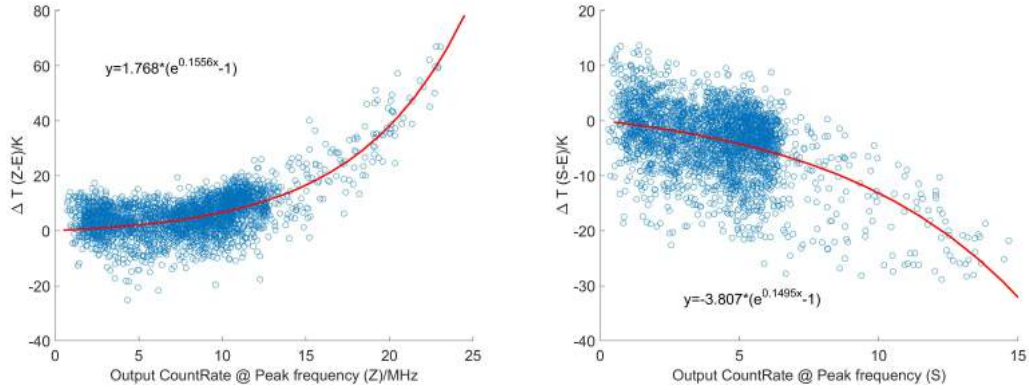


Figure 3.7: Scatter plots of the temperature differences of zenith minus east (left) and south minus east (right) vs. the output count rates. Exponential fittings and the fitting parameters are also shown.

the temperature error and the count rate. These exponential curves and their parameters are also presented in Figure 3.7. Note that for each temperature error, there are three count rates, corresponding to f_0 and f_{\pm} , that can all affect the temperature therefore related to the temperature error. However, since the count rates at f_{\pm} are always smaller than that at f_0 , they are always more accurate than the peak count rate. Based on this, we use the following procedure to derive the PMT curve. Start from a small output count rate at 0.5 MHz, where the PMT linearity is very good, as the output count rate at f_0 . The original PMT curve is used to obtain the PMT input count rates at all three frequencies, then applied to calculate the temperature. Then adjust the input count rate at f_0 , while keep the input count rates at f_{\pm} fixed, until the temperature derived eliminates the error represented by the exponential fit at this count rate. The new input count rate at f_0 gives the revised PMT correction at this output count rate. In the next step, the output count rate at f_0 is increased to 1 MHz. The input count rate at f_0 is again adjusted to eliminate the error at this output count rate, and the final input count rate gives the revised PMT correction at 1 MHz. This process is repeated with 0.5 MHz increment until maximum count rate measured in the data. The adjusted curves are plotted in Figure 3.8a as solid blue and red lines, together with the

original curves as dashed lines. It shows that the old PMT is indeed over corrected, and the new PMT is under corrected. The percentages of correction errors are shown in Figure 3.8b. They are not constant, with maxima at about -30% and 40% for the new and old PMTs, respectively. These revised curves were then applied to reprocess the lidar data and

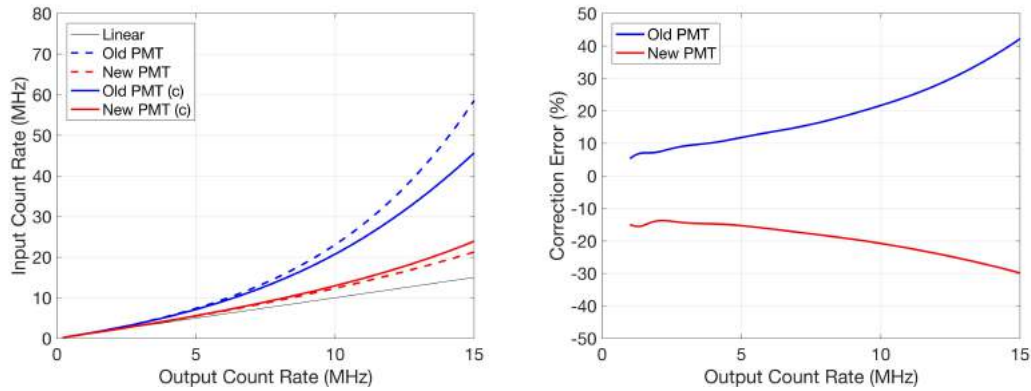


Figure 3.8: Top: Old (blue) and new (red) PMT correction curves. Dashed lines are laboratory-measured correction curves. Solid lines are the adjusted curves based on measured temperature errors. The thin black line indicates the linear relationship. Bottom: The error percentages of the original old (blue) and new (red) PMTs correction curves.

the results are shown in Figures 3.9 and 3.10. The extremely high temperature and downward velocity do not exist anymore, and the temperature between zenith and south are in very good agreement with that at east. This demonstrates that this calibration process is successful in identifying and eliminating errors in PMT curves.

Since the adjusted curve for the new PMT also affects the results at east, it may be necessary to repeat above process to further revise the PMT curve based on the newly processed data. However, it is found experimentally that the change in temperature at east is very small so no second revision is needed. The revised curves are then applied to reprocess the data on other nights, and all of them produced more consistent results.

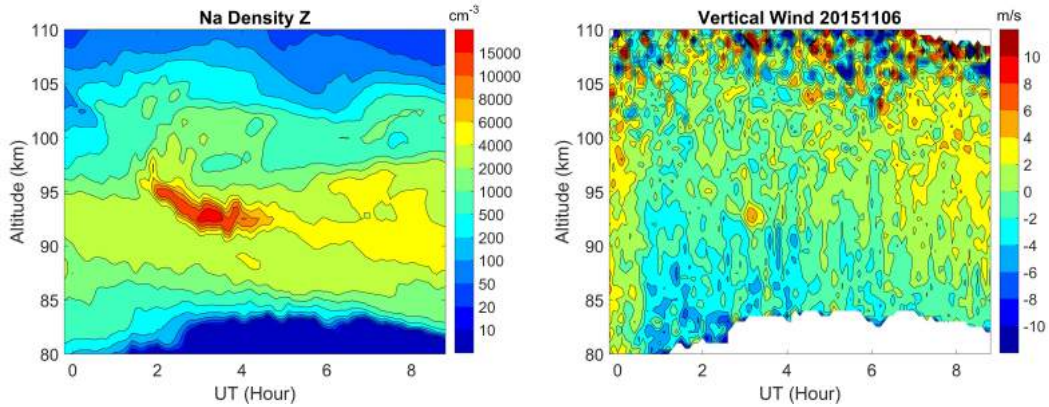


Figure 3.9: Same as Figure 3.4 but with revised PMT correction curve.

3.4 Heat Flux Bias due to PMT Correction Error

It is clear from the above analysis that the PMT correction error significantly affect the derived temperature and wind. Because the errors in temperature and wind are related through the effective cross section, their correlation is non-zero. This correlation will create a bias in the heat flux, which is the covariance of temperature and vertical wind perturbations, $\langle w'T' \rangle$, where the brackets represent ensemble average.

3.4.1 Numerical method

To assess this bias quantitatively, a numerical method is employed. The simulation repeats the process described in section 3.2.2, but with temperature and wind specified as sinusoidal functions of time instead of actual observational data. Temperature and wind are expressed as

$$T(t) = T_0 + A_T \cos \omega t, \quad (3.2)$$

$$W(t) = W_0 + A_W \cos(\omega t + \phi), \quad (3.3)$$

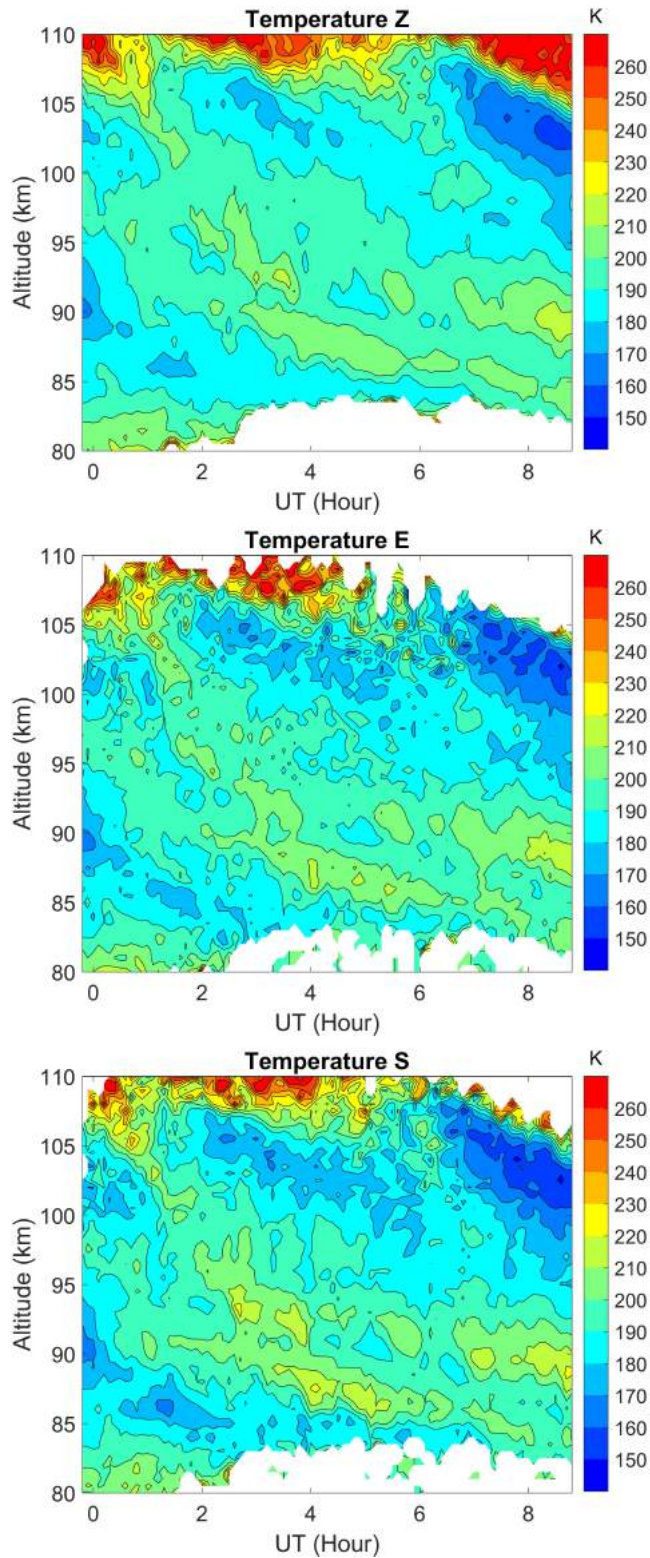


Figure 3.10: Same as Figure 3.5 but with the revised PMT correction curves.

where $A_T = 5$ K, $A_W = 1$ m/s, and ϕ varies from -15° to 45° . The heat flux is calculated from

$$\langle w'T' \rangle = \frac{1}{2\pi} \int_0^{2\pi/\omega} (W - W_0)(T - T_0) dt. \quad (3.4)$$

For the above parameters, $\langle w'T' \rangle$ varies from -1.77 K m/s when $\phi = 45^\circ$ to $+0.64$ K m/s when $\phi = -15^\circ$. By adding errors to the PMT correction curve, the heat flux is recalculated for different peak frequency count rates. The difference in heat flux is the bias resulted from the error in PMT correction.

Figure 3.11a shows the specified sinusoidal oscillation of T and W , with 5 min period and phase difference $\phi = 20^\circ$. For this parameter set, the heat flux is -1.25 K m/s. The specific value of the period used is irrelevant for the heat flux. Figures 3.11b and c show the temperature and wind errors after +30% error is added to the PMT correction, at 6 MHz and 12 MHz peak count rate, respectively. It is clear that the positive error results in negative temperature error and positive wind speed error. In addition however, there are also sinusoidal variations of the errors, related to the sinusoidal variations of the original temperature and wind. Comparing with Figure 3.11a, we can see that the errors are generally opposite to the temperature and wind variations. This results in reduction of both temperature and wind perturbations, leading to a reduction of the heat flux magnitude. The heat flux is changed from -1.25 K m/s to -1.06 K m/s at 6 MHz and to -1.02 K m/s at 12 MHz. Since the heat flux is negative, this creates a positive bias of 0.19 K m/s and 0.23 K m/s, respectively

A more complete description of the bias as a function of both the heat flux and the count rate with +30% error in PMT correction is shown as a contour plot in Figure 3.12. The bias is always positive with positive error (over correction). As expected, the bias is larger when the peak count rate is larger. It's interesting to note that the bias is larger for negative heat flux than for positive heat flux. Unfortunately, in a stable atmosphere, the heat flux is

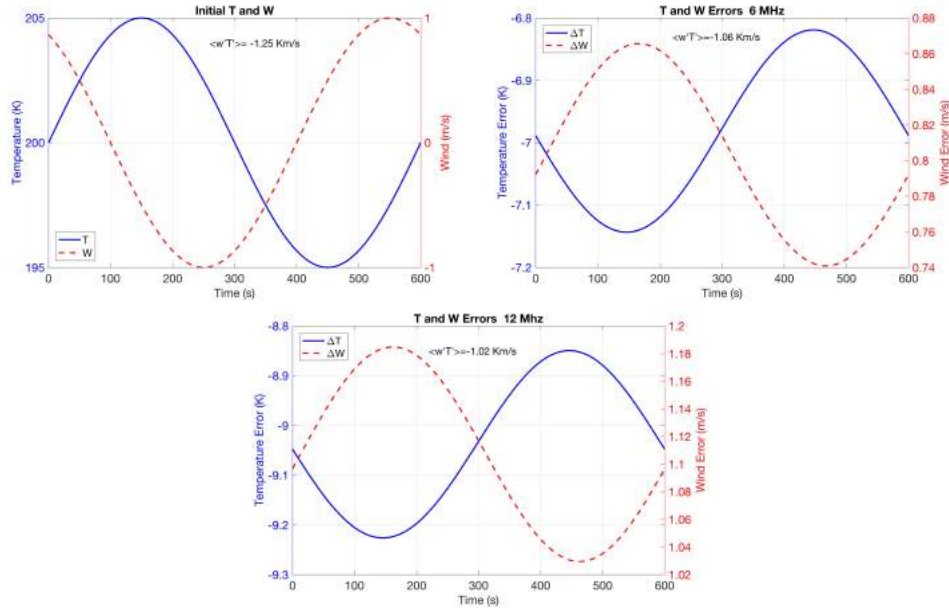


Figure 3.11: Left: Initial temperature and wind. Middle: Temperature and wind errors when +30% error is added to the PMT correction amount, with peak frequency count rate at 6 MHz. Right: Same as the middle except with peak frequency count rate at 12 MHz.

generally negative [Walterscheid, 1981b], which does not help to alleviate this bias. Since the heat flux is generally small, the bias at large peak count rate is not negligible. It can be expected that if the PMT correction error is negative, it would result in a negative bias in the heat flux.

3.4.2 ALO heat flux correction

The heat flux due to dissipating gravity waves is calculated from the temperature and vertical wind perturbations in the same way as described in Gardner and Liu [2007]. Initial attempt to use the ALO lidar data to calculate the heat flux at Cerro Pachón yielded positive heat flux throughout the entire Na layer. The calculation was made using zenith measurements from May 2014 to Apr 2015 when the old PMT was used. As seen in Figure 3.8a, the original PMT curve (blue dashed line) over-corrected the nonlinear effect, and such over

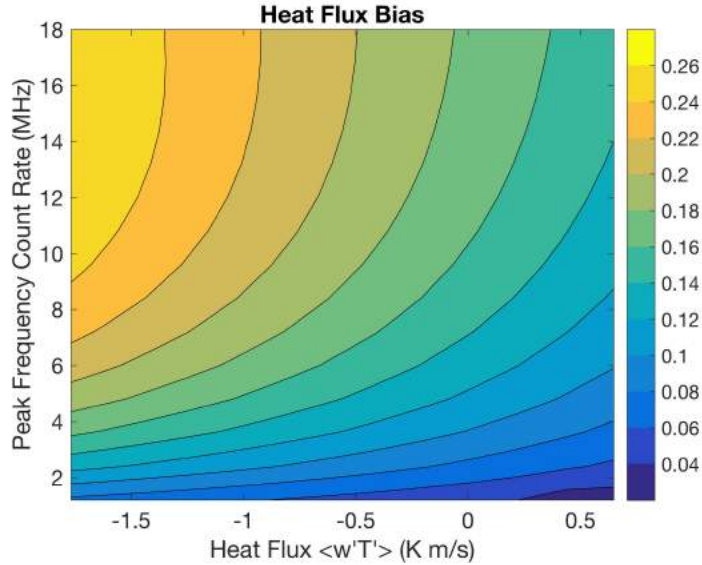


Figure 3.12: Heat flux bias as a function of count rate and the heat flux for a +30% error in PMT correction. See text for details.

correction resulted in a positive heat flux bias as demonstrated in our simulation shown in Figure 3.12. After reprocessing the lidar data using the revised PMT curve (blue solid line in Figure 3.8a), we recalculated the gravity wave heat flux. Both the original and the revised heat flux are shown in Figure 3.13. The heat flux has a significant shift towards negative values with the revised PMT curve, consistent with a positive bias in the original calculation. Further more, the revised heat flux is similar to that obtained in *Gardner and Liu* [2007] (Figure 7(a)) at Starfire.

The magnitude of bias shown in Figure 3.13 is much larger than that shown in Figure 3.12, primarily due to larger amplitudes of temperature and vertical wind perturbations than used in the simulation. The largest bias is around 89 km, where both the Na density and the heat flux magnitude is large. This is expected since Figure 3.12 shows that the bias is larger with larger count rate and larger downward heat flux.

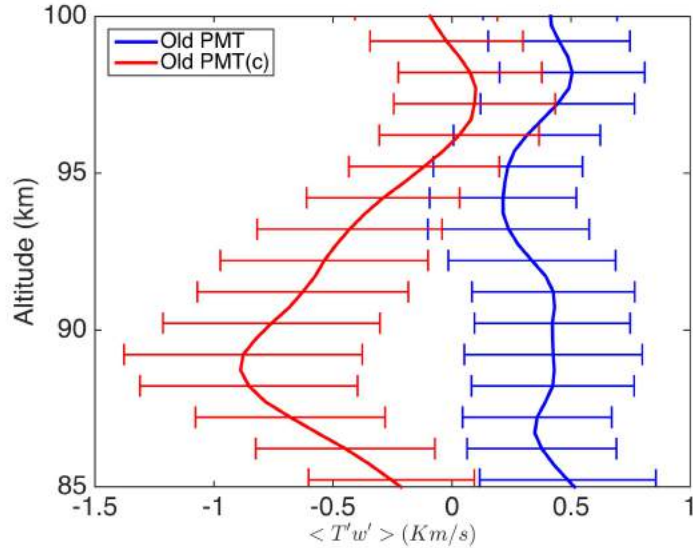


Figure 3.13: Gravity wave heat flux calculated from 26 nights of zenith measurement of vertical wind and temperature from May 2014 to Apr 2015. Blue is the original heat flux profile and red is the profile obtained after the data were reprocessed using the revised PMT curve.

3.5 Summary

The PMT saturation is a well known effect and for most applications, a laboratory measured correction will be sufficient because a PMT normally operates at low count rates not too far beyond the linear range. However, for Na lidar operations, the Na density, hence the signal, has a very large dynamic range, varying by 4 orders of magnitude. To detect low signals with low noise, a high QE PMT is desired. Unfortunately, current high QE PMTs such as the Hamamatsu models have a small linear range, and are therefore prone to severe saturation at high count rates. The laboratory-measured correction curve at high count rates in the strong nonlinear region is prone to errors because the input rates changes quickly with a small change in the output rates.

In this work, a practical method is demonstrated to calibrate the PMT correction curves, since the existence of obvious error has been observed from lidar measurements. By com-

paring the measurements made with different PMTs, a revised curve is obtained based on the relationship between temperature errors and count rates. The revised PMT correction curve produced by this procedure guarantees the consistency of temperature (and wind) measured with at different directions. The requirement for this procedure to work is to have measurements of the same quantity with different PMTs, and preferably with one PMT known to be more reliable than the other. However, even with a single PMT measurement, some obvious artifacts from erroneous PMT correction (as shown in Figure 3.5) can also be used to obtain an improved correction curve, though with less accuracy.

It is also shown theoretically and with observational data that such correction errors can introduce a significant bias in heat flux calculation, due to intrinsic correlations between temperature and wind errors. With the calibration process, the heat flux bias can be largely eliminated and the corrected heat flux is more consistent with theoretical expectations.

Chapter 4

Dissipating Gravity Wave Induced Vertical Fluxes

This Chapter focuses on characterizing the seasonal vertical heat flux induced by gravity wave dissipation with over 400 hours of concomitant vertical wind and temperature measurements made by ALO lidar. The work is based upon the work in *Guo and Liu* [2017].

4.1 Introduction

Atmospheric gravity waves are well known for their important roles in establishing the atmospheric mean circulation and thermal structure in the mesosphere and lower thermosphere through their deposition of energy, momentum, and heat into the background when dissipated [e.g. *Hines*, 1960; *Hodges*, 1969; *Hines*, 1970; *Lindzen*, 1981; *Holton*, 1983; *Fritts and Alexander*, 2003]. Over the last few decades, numerous studies have contributed to our understanding of the dynamical impact of GW dissipation through their momentum flux, but their direct thermal impact through heat transport is not widely studied. Even though dissipating GWs are expected to deposit energy in the MLT resulting in a source of heating within the atmosphere [*Hines*, 1965], *Walterscheid* [1981a] pointed out that GWs dissipated through a diffusive process induce a downward sensible heat flux regardless of their propagating directions. This heat flux therefore creates a cooling effect in the upper region of wave dissipation. On the other hand, GW dissipation can also occur through non-linear interactions and wave breaking, leading to turbulence [*Fritts and Alexander*, 2003].

Weinstock [1983] demonstrated a derivation of heat flux with nonlinear GW theories and showed that heat flux is also downward and brings substantial cooling to the mesopause where waves are highly saturated. Many numerical simulations were also carried out to study the heat flux by dissipating GWs [e.g. Liu *et al.*, 2000; Medvedev and Klaassen, 2003; Becker, 2004; Yiğit and Medvedev, 2009; Hickey *et al.*, 2011], which all confirmed the GW downward heat flux and its cooling effect.

Observational measurements of the GW heat flux in the MLT are rare, largely due to the challenges of accurately measuring the small vertical wind perturbations needed for heat flux calculation, as well as the fact that heat flux is such a small quantity to be non-zero only when gravity waves dissipate. A narrow band Na lidar is capable of making continuous, simultaneous measurements of vertical wind (w), temperature (T), and resolving GW scale perturbations. Thus it is currently the only instrument that can provide the direct measurement of sensible heat flux. The sensible heat flux, $\langle w'T' \rangle$, where the angle brackets denote the mean over time and the primes denote GW perturbations, can be readily calculated if the measurements are of high enough resolutions to resolve GWs and with small enough noise. Early attempts of calculating sensible heat flux [Tao and Gardner, 1995; Gardner and Yang, 1998] using Na lidar measurements were limited by the requirements of long observation time to reduce the large uncertainties since the variance of instantaneous flux is large and the mean flux is very small. Technology advancement has significantly increased lidar signals from two decades ago, such that GW perturbations can be resolved reliably at high enough temporal (~ 1 min) and vertical (≤ 1 km) resolutions for accurate heat flux measurement. More recent studies by Liu and Gardner [2005] and Gardner and Liu [2007] (hereinafter referred to GL07) using the Na lidar measurements at Starfire Optical Range (SOR), NM (35°N, 106.5°W) and Maui, HI (20.7°N, 156.3°W) have shown a predominantly downward sensible heat flux at both locations, with a magnitude on the order of 1 K ms^{-1} and a cooling rate of several tens of K per day. These results are consis-

tent with theoretical predictions. The amount of cooling due to this downward heat flux is significant since they are comparable to other heating/cooling mechanisms in this region. Since the heat flux is expected to vary depending on wave sources and dissipation processes, more measurements are needed to understand its variabilities at different locations and for different GW sources.

According to the linear GW theory, GW heat flux (also called enthalpy flux) $\langle w'\theta' \rangle$, vanishes for freely propagating GWs, where θ' is the potential temperature perturbation and conserved for adiabatic motions. When waves dissipate, w' and θ' are no longer in quadrature [Plumb, 1979; Liu, 2000; Fritts and Alexander, 2003; Akmaev, 2007], so $\langle w'\theta' \rangle$ becomes non-zero. $\langle w'\theta' \rangle$ is also referred as the flux of potential temperature. Hence the heat flux $\langle w'\theta' \rangle$ is also a measure of GW dissipation. Since Na lidar measures T' directly, not θ' , only the sensible heat flux $\langle w'T' \rangle$ can be directly calculated, but not $\langle w'\theta' \rangle$. Nevertheless, $\langle w'T' \rangle$ and $\langle w'\theta' \rangle$ are related through the GW energy flux. From the definition of potential temperature

$$\theta = T(p_0/p)^\kappa,$$

where $\kappa = R/C_p$, R is the dry air constant, c_p is the specific heat at constant pressure, p is pressure and $p_0 = 1000$ hPa, $\langle w'\theta' \rangle$ can be expressed as:

$$\frac{\langle w'\theta' \rangle}{\bar{\theta}} = \frac{\langle w'T' \rangle}{\bar{T}} - \kappa \frac{\langle w'p' \rangle}{\bar{p}}, \quad (4.1)$$

where $\langle w'p' \rangle$ is the kinetic energy flux carried by GWs. In the mesopause region, most GWs propagate upward so the average $\langle w'p' \rangle$ is positive. Therefore, for freely propagating GWs, $\langle w'\theta' \rangle = 0$ and $\langle w'T' \rangle > 0$. They both become negative when waves are strongly dissipated, and are identical when the Boussinesq approximation is applicable (p' is negligible), which is often not the case in the mesopause region.

The main purpose of this study is to investigate the enthalpy flux due to GWs over the

Andes, based on newly acquired Na lidar data at the Andes Lidar Observatory (ALO). The Andes is a region where strong waves are generated due to the steep terrain. Heat flux measurement in this region is a valuable addition to the only two heat flux measurements at Maui and SOR in the literature. In this analysis, we not only calculated the sensible heat flux $\langle w'T' \rangle$, but also derived $\langle w'\theta' \rangle$ for the first time by estimating $\langle w'p' \rangle$ from measured GW frequency and vertical wavenumber spectra. The spectral measurements are made possible with the high quality lidar measurements. The derived $\langle w'\theta' \rangle$ is a more accurate measure of GW dissipation and thermal effect. The energy flux also provides additional insight to the GW propagation and energy transfer in this region.

The chapter is organized as follows. Section 2 describes the Na lidar dataset and the method applied to derive gravity wave perturbations. Section 3 presents the algorithm for calculating energy flux from GW temperature spectra. In section 4, we present the seasonal variations of heat and energy flux, and the associated heating/cooling rate. In section 5, we consider the contributions of GWs at different scales to these vertical fluxes. The conclusion is given in section 6.

4.2 Observations

The narrow band Na lidar is located at ALO (30.25° S, 70.74° W) in Cerro Pachón, Chile, providing nightly measurements of temperature, light-of-sight (LOS) winds, and Na density between 80 to 105 km. The ALO lidar is equipped with four 75-cm diameter telescopes in zenith (Z) and 20° off-zenith to the north (N), south (S), and east (E) directions. The lidar system was upgraded in May 2014 with the old Coherent Ring Dye Laser replaced by a high-power amplified diode laser (TA-SHG from Topica Photonics. Inc.) as the master oscillator [Liu *et al.*, 2016]. Meanwhile, the receiver system was also improved with a more accurate design to increase the efficiency [Smith and Chu, 2015]. These improvements

result in a much more reliable and stable system with several times higher signals, which makes it possible for higher temporal and spatial resolution measurements.

Since the upgrade, the ALO lidar has been operated for nine campaigns with 105 total observation nights up to November 2016. Data is available in every calendar month except December. Several laser beam pointing modes were used during the campaigns, such as zenith only, zenith and off-zenith in a sequence of ZSZE or ZSE. In this study, since we focus on the vertical transport, the zenith measurements on each night, despite the operation mode, with over 400 hours of concomitant temperature and vertical wind data are used to derive the associated GW perturbations. The data in each month is summarized in Table 4.1. Because of the different operation modes, the number of nights and hours are not necessarily related. For example, the lidar was operated in zenith direction only in May, so the total number of hours (31) is comparable to the other months even though there were only 4 nights of lidar operation in this month.

Table 4.1: Nights and hours of lidar vertical measurements for each month since the upgrade in May 2014, no data in December.

Month	Jan	Feb	Mar	Apr	May	Jun	Jul	Aug	Sep	Oct	Nov	Dec	Total
Nights	14	7	14	13	4	6	11	4	7	10	15	0	105
Hours	70	21	34	49	31	20	18	30	63	32	38	0	406

The raw data was obtained in 6-s temporal and 25-m range resolutions, then reduced to 60-s integration time and 500-m vertical resolution to derive the LOS winds and temperature. At these resolutions, the typical root mean square errors for temperature and LOS winds are respectively 1.4 K and 1.1 ms^{-1} at the center of Na layer and 2.2 K and 2.0 ms^{-1} at 85 km and 100 km. The errors grow quickly beyond this altitude range. Here we focus on the height range between 85 and 100 km, where Na density is higher and measurement errors caused by photon noise are relatively small. The typical observation duration for

each night is 9 to 10 hours in winter and ~ 8 hours in summer.

Preprocessed temperature and wind profiles on each night were first smoothed with a 5-min and 1-km full width Hamming window to remove small scale fluctuations. Perturbations associated with GWs were then derived by first applying a Hamming window with 6-hour full width at each altitude, the remaining is considered to be fluctuations associated with larger period waves such as tides. The smoothed out fluctuations are the GW perturbations. The vertical mean was then subtracted for each profile to remove waves whose vertical wavelength are longer than the profile altitude range (~ 15 km). Therefore, the derived perturbations contains waves roughly with scales between 1 and 15 km in vertical wavelengths, and 5 min to 6 hours in periods. An iterative process to remove outliers was applied, which discard perturbations larger than 3 times the standard deviations. The derived perturbations are grouped into different calendar months for seasonal variation analysis.

Since the downward heat flux are related to GW activities and wave dissipation, it can be used to examine how different scale waves contribute to the heat transport and how wave dissipation differs at different scales and altitudes. In order to analyze the heat flux for waves at different scale, three band-pass filters are applied to the temperature and wind profiles. The periods corresponding to the lower cut-off frequencies of the three band-pass filters are 5 mins, 1 hours and 3 hour, respectively; the periods corresponding to the higher cut-off frequencies are 1 hours, 3 hours, and 6 hours. With these filters, GW perturbations are derived into three groups with periods from 5 m to 1 h, 1 h to 3 h, and 3 h to 6 h. Notice that filtering is only applied in the temporal direction because the altitude range of 15 km is already small. The contributions of the three different group GWs are separately analyzed.

4.3 Energy Flux

As discussed in Section 4.1, the heat flux $\langle w'\theta' \rangle$ is exactly zero for non-dissipating GWs, because θ' is a conserved quantity in energy equation [Plumb, 1979]. However, the lidar measures temperatures (T) directly instead of θ , and without pressure measurements, only $\langle w'T' \rangle$ can be directly calculated.

The GWs observed in the mesopause are generally originated from lower atmosphere and propagate upward with increasing amplitudes, then experience breaking and dissipation due to instabilities and viscosity at higher altitudes. The deposition of energy and momentum by GWs plays an important role in establishing the thermal and zonal mean wind structure in the mesopause region. Gravity wave momentum flux has been studied extensively with observations from radar, lidar, airglow imager, and also from global circulation models. In contrast, energy flux has not yet been widely acknowledged because of the challenge in measuring pressure and vertical velocity at the same time. Only a few numerical simulations and models [e.g. Hickey and Cole, 1988; Yu and Hickey, 2007; Walterscheid and Hickey, 2011; Ehard et al., 2016], and some limited observations [e.g. Gossard, 1962; Vincent, 1984] contribute to our understanding of GW energy flux. The GW energy flux is not negligible and must be taken into account when evaluating the influences of GWs [Becker and Schmitz, 2002; Becker, 2004; Walterscheid and Hickey, 2011].

Although the vertical energy flux is difficult to measure directly, Liu [2009] derived an approximate expression for relative energy flux ($\langle w'p \rangle / \bar{p}$) based on GW polarization relations. The relative energy flux basically can be related to the temperature variance over a broad spectrum of GWs that lidar can observe. This approximation requires the power spectra of a wave's intrinsic frequency ($\hat{\omega}$) and vertical wavenumber (m). Numerous studies during the last several decades have contributed to our understanding of GW spectral characteristics [e.g. Hines, 1991; Senft and Gardner, 1991; Dewan, 1994; Gardner, 1994; Zhu,

1994; Dewan, 1997; Zhang *et al.*, 2012; Lu *et al.*, 2015b; Zhang *et al.*, 2017]. Both existing observations [Senft and Gardner, 1991; Beatty *et al.*, 1992; Senft *et al.*, 1993] and theories [Weinstock, 1990; Gardner, 1994] suggest that the spectra of temperature, horizontal winds, and density usually exhibit a spectral structure with logarithmic slopes varying between -3 to -2 for m and a typical value of -2 for intrinsic frequency $\hat{\omega}$. However, the slopes do not exactly follow these values all the time under conditions such as strong shear [e.g. Eckermann *et al.*, 1995] and enhanced saturation [e.g. VanZandt and Fritts, 1989]. The spectral characteristics also depend on the source, wave propagation and dynamics, and vary between different altitudes, seasons and locations [e.g. Allen and Vincent, 1995; Nastrom *et al.*, 1997]. Here we calculated the GW spectra over ALO in different seasons and applied the results to the energy flux calculation in order to obtain $\langle w'\theta' \rangle$. The frequency measured by ALO lidar is non-intrinsic, which is the case for most ground-based instruments since the frequency is not observed in a frame moving with the background wind. Doppler shifting of the intrinsic frequencies by the horizontal winds can have significant impacts on the observed frequency spectrum, as energy is shifted to frequencies higher than the buoyancy frequency and lower than the inertial frequency. These effects could change the spectral slopes by as much as 10-20 % decreasing and increasing the slope, depending on whether waves are propagating along or against the background winds. The flux measurement errors caused by this discrepancy between intrinsic and observed frequencies will be discussed later. Assume the GW spectrum is separable for ω and m joint spectra according to the linear instability theory [Hodges, 1967; Dewan and Good, 1986], and the indices for ω and m spectra are p_1 and p_2 , following Liu [2009], the energy flux can be expressed as

$$\begin{aligned} \frac{\langle w'p' \rangle}{\bar{p}} &= \int_{m_1}^{m_2} \int_{\omega_1}^{\omega_2} |\tilde{w}\tilde{p}^*| d\omega dm \approx -\frac{g}{N^2 H} \iint \frac{\omega}{m} |\tilde{T}|^2 d\omega dm \\ &= -\frac{gT'^2}{N^2 HT^2} \frac{m \iint \omega^{1+p_1} |m|^{-1+p_2} d\omega d|m|}{\iint \omega^{p_1} |m|^{p_2} d\omega d|m|}, \end{aligned} \quad (4.2)$$

where H is the scale height, g is the gravitational acceleration, N is the buoyancy frequency, and $\overline{T'^2}$ is the temperature variance. From GW linear theory we know that m is negative for upward propagating waves. The limits of two integrals (ω_1, ω_2) and (m_1, m_2) depend on the data resolutions and the scale range of perturbations, where (m_1, m_2) were absolute value of vertical wavenumber. Here in our study, the period and vertical wavelength corresponding to ω and m extend from 5 minutes to 6 hours and 1 to 15 km because the smallest and largest scale waves are smoothed out during data processing. Therefore, the integration limits are chosen as follows: $\omega_1 = 2\pi/6 \text{ hour}^{-1}$, $\omega_2 = 2\pi/10 \text{ min}^{-1}$, $m_1 = 2\pi/15 \text{ km}^{-1}$, and $m_2 = 2\pi/1 \text{ km}^{-1}$.

The ω and m power spectra density (PSD) of T' are derived based on each night, then nights in the same calendar month are averaged to obtain the seasonal spectrum. The ω -spectrum is calculated with all of the profiles at each altitude and averaged through the entire region, and the m -spectrum is calculated between 85 to 100 km for each profile and then averaged though the entire night. Slopes are obtained by linear regression fitting to the PSDs under the logarithmic coordinates after the photon noise floors are subtracted. Figure 4.1 shows the monthly variation of ω and m . The annual slopes are -1.90 ± 0.14 and -2.75 ± 0.31 , respectively, for ω and m , which are quite close to the measurements in SOR with -1.98 for ω and -2.74 for m [Gardner, 1998]. Our calculated ω and m are shallower compared with the theoretical slopes of -2 for ω and -3 for m , but are generally consistent with other measurements in the mesopause region [e.g. Senft and Gardner, 1991; Gardner et al., 1998; Yang et al., 2008; Lu et al., 2015b]. Notice that ω has smaller uncertainties than m , which is more data points in the temporal direction. The narrow region (~ 15 km) and rather lower resolution (500 m) in the vertical direction limits the data points for the fitting as well as the vertical scale range that lidar can resolve. ω varies from -2.01 ± 0.17 in March to -1.69 ± 0.16 in October, and is larger at equinoxes and smaller around solstices. For m , the maximum -2.91 ± 0.24 appears in June, which is the southern

hemisphere winter. These results are then applied to eq. (4.2) for energy flux calculations. In addition to the spectral characteristics of temperature perturbations, temperature vari-

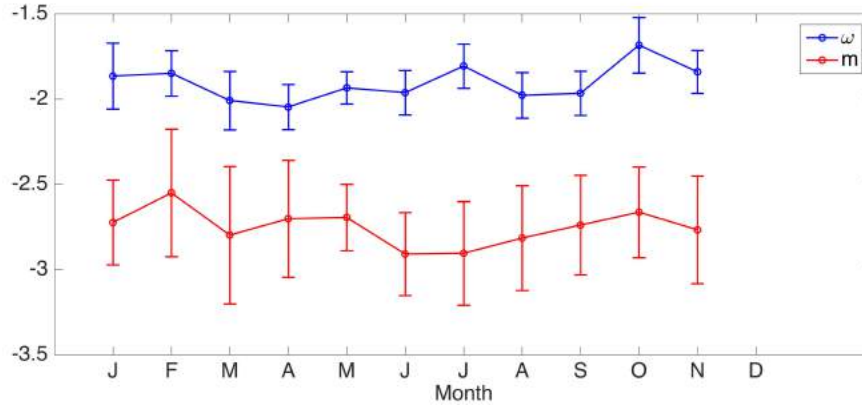


Figure 4.1: Seasonal variation of T' power spectra slopes. Blue line is frequency and red is for vertical wave number. The error bars represent the standard deviations calculated from linear fitting uncertainties.

ance is also required for energy flux estimation. The atmospheric parameters in eq. (4.1) including buoyancy frequency (N), scale height (H), and temperature variance ($\overline{T'^2}$) were all derived from mean temperature and perturbations. Contour plots shown in Figure 4.2 are the monthly temperature variance and vertical energy flux. Temperature measurements with error larger than 10 K due to photon noise at the Na layer boundaries are excluded. The minimal temperature variances occur in March at 85 and 92 km with values of 40 K^2 approximately. It is recognized that GW variances usually correspond to wave activities in the mesopause region. The weak GW activity also shows up around October. Largest variance ($\sim 80 \text{ K}^2$) appears during southern hemisphere winter in August. Overall, GW activities are stronger during solstices and weaker during equinoxes, which is consistent with the results observed in SOR by GL07. The magnitudes are comparable for both locations between 85 to 100 km.

The energy flux illustrated in Figure 4.2(b) is inferred from relative energy flux defined in eq. (4.2). The mean pressure (\bar{p}) is obtained from the atmospheric model MSISE-00

[Picone *et al.*, 2002]. Monthly profiles are smoothed with a 5 km full width hamming window. The most prominent feature in $\langle w'p' \rangle$ is that the magnitude varies in three orders of magnitude from 10^{-2} Wm^{-2} to 10^{-4} Wm^{-2} and decreases exponentially with altitude. The maximal energy flux is observed in July at 86 km and the minimal is during March, which are consistent with the variation of temperature variances.

4.4 Seasonal Heat Flux

As mentioned in Section 4.1, the ALO Na lidar measures temperature and vertical wind, so sensible heat flux $\langle w'T' \rangle$ can be derived directly. Characterizing vertical heat flux has been challenging for modern techniques because it's a small quantity and the variation of instantaneous flux is large. Therefore, long term observations are required to reduce the uncertainties. Assuming the measurement errors caused by photon noise for T and w are ΔT and Δw , then the unbiased sensible heat flux is

$$\langle w'T' \rangle_{(unbiased)} = \langle w'T' \rangle + \langle \Delta w \Delta T \rangle, \quad (4.3)$$

where the second term on the right hand side is the flux bias caused by photon noise. In lidar data processing, T and w are derived based on the ratios of signals from three frequencies, with the peak frequency f_0 locked at Na D2a line, and two side frequencies (f_- and f_+) are ± 650 MHz off the peak. Because T and w are derived from the same set of photon count profiles, ΔT and Δw are correlated, which will induce a bias to the measured heat flux. This bias can be estimated with linearized system equations that relate atmospheric parameters to three-frequency photon count profiles [Gardner and Vargas, 2014] and then subtracted from the calculated flux to obtain the unbiased heat flux. The magnitude of $\langle \Delta w \Delta T \rangle$ is in an inversion relationship with photon counts, so data with higher signal-to-noise ratios will generate smaller heat flux bias [Gardner and Yang, 1998]. The ALO lidar was upgraded in

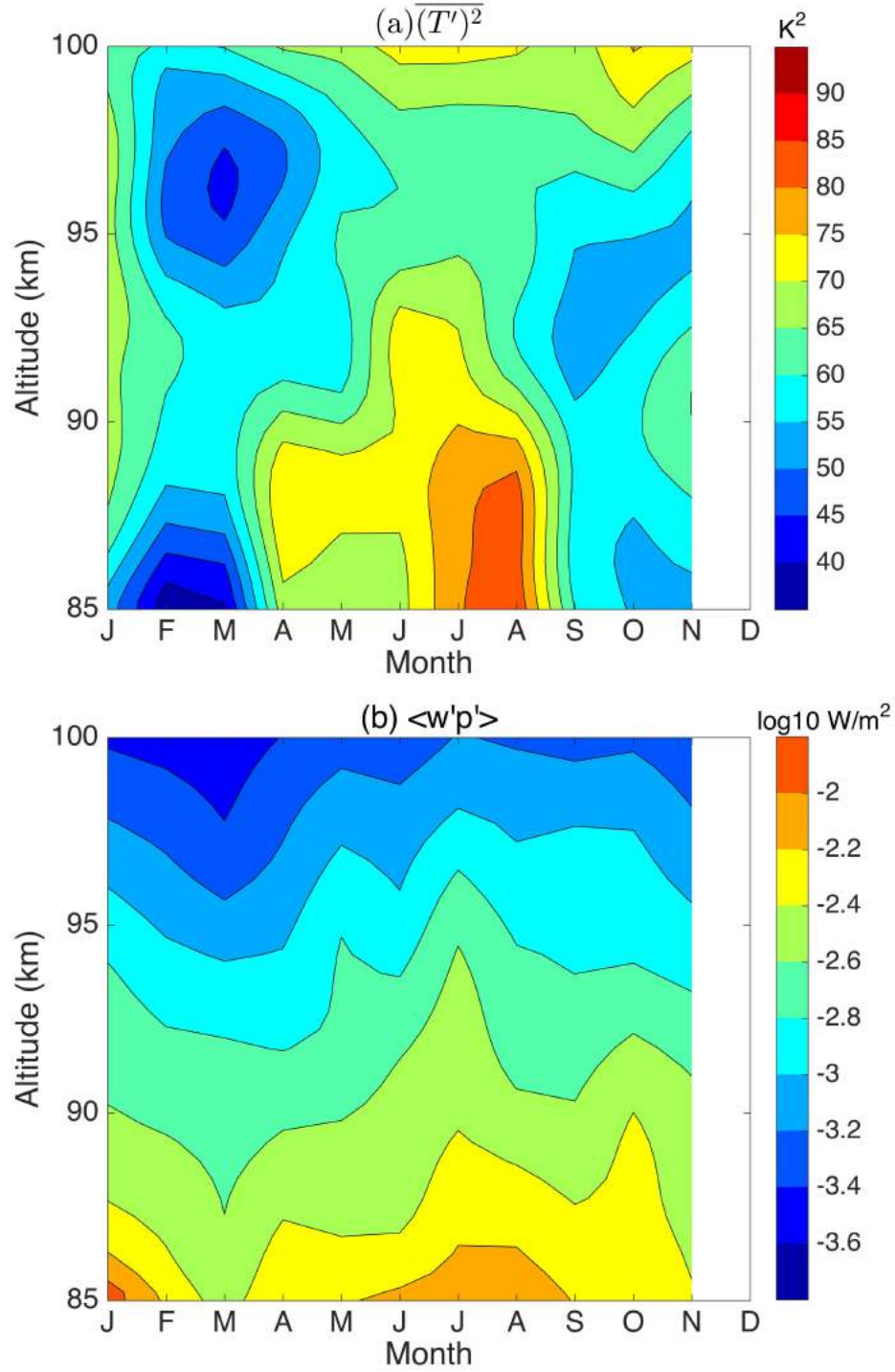


Figure 4.2: Seasonal variation of gravity wave (a) temperature variance and (b) vertical energy flux inferred from eq. (4.2).

May 2014 resulting in several times higher signal levels. Under the resolutions of 60 s and 500 m, the raw photon count at peak frequency can exceed 5×10^4 and the corresponding bias is less than 0.05 Kms^{-1} , which is negligible for heat flux calculation. For lidar systems with much lower signal levels, such as the ALO data before upgrade, heat flux bias can reach a few 0.1 Kms^{-1} with relative error as large as 50% and affect the heat flux results substantially.

Apart from the bias caused by the correlation of lidar measurement errors, we also found out that the nonlinearity of Photomultiplier Tube (PMT) would introduce bias to the vertical heat flux calculation as well [Liu and Guo, 2016]. A PMT is a device implemented in the lidar receiving system that counts the number of incoming photons at very low levels. The high signal reduces the heat flux bias but the nonlinearity of the PMT increases at the same time. This nonlinearity influences the retrieved wind and temperature from lidar data directly. We used both analytical and numerical methods to calibrate the PMT and estimated the possible flux bias induced by the PMT nonlinearity. With the calibrated PMT curves obtained in Liu and Guo [2016], it is possible to eliminate the bias and get an unbiased estimation of vertical heat flux. Since we only use the high quality data after the upgrade, all the nights were reprocessed with the new PMT curves and the updated temperature and winds profiles are applied to calculate fluxes.

In this work, we derived $\langle w'\theta' \rangle$ by considering the contribution of vertical energy flux as in eq. (4.1), which has not been well addressed before. A comparison between the two heat fluxes is presented in Figure 4.3, where (a) is the monthly mean $\langle w'T' \rangle$ computed from wind and temperature perturbations directly and (b) is the monthly mean $\langle w'\theta' \rangle$ estimated from (a) and Figure 4.2(b) by using eq. (4.1). The contour color bar is not symmetric with respect to zero because of the downward heat transport and negative heat flux [Walterscheid, 1981a]. To achieve a better comparison between the two heat flux calculations, same color bar is chosen so the difference between two heat flux definitions are more ob-

vious. The sensible heat flux $\langle w'T' \rangle$ is mostly downward below 95 km throughout the year. The monthly profiles exhibit some dominate seasonal features. The maximum downward flux appears at the top boundary with values exceeding -3 Kms^{-1} in the southern hemisphere winter. There are two downward transport regions around 88 km in May and Aug. Overall the results agree well the flux reported in SOR by GL07 except that the seasons are reversed since these two locations are in different hemispheres. The positive values above 96 km with a maximum in September exceeding 1 Kms^{-1} are proportional to the relative energy flux where waves are not dissipating. Shown in Figure 4.3(b) is the flux of potential temperature $\langle w'\theta' \rangle$ (also referred as heat flux or enthalpy flux). We can see obviously that the heat flux is downward throughout the region and year. Strong transport happens in several months at different altitudes, which agrees well with the strong wave activities inferred from large temperature variance in Figure 4.2(a). This downward heat flux is generally larger during solstice and smaller during equinoxes. The altitudes where heat flux is maximum varies between seasons. For example, from January to February, the maximum moves down from 95 km to 90 km, and from July to August, it moves down from 98 km to 88 km. The results are consistent with our knowledge that dissipating GWs induce a downward $\langle w'\theta' \rangle$ and a mostly downward sensible heat flux shown in eq. (4.1).

The net thermal effects of dissipating and/or breaking GWs include the heating from irreversible conversion of mechanical wave energy [e.g. *Pitteway and Hines*, 1963; *Hines*, 1965; *Gavrilov*, 1990; *Medvedev and Klaassen*, 2003] and a cooling by the downward transport of sensible heat [e.g. *Walterscheid*, 1981a; *Schoeberl et al.*, 1983; *Gardner and Liu*, 2007; *Hickey et al.*, 2011]. In terms of the heating caused by energy deposition, *Hickey and Brown* [2000] pointed out that the wave energy flux may be transferred to kinetic energy of the mean winds instead of being fully deposited as heat in the background atmosphere as considered in *Matcheva and Strobel* [1999]. Thus, the heating associated with the energy flux is more complicated and will not be discussed here. This dynamical cooling ef-

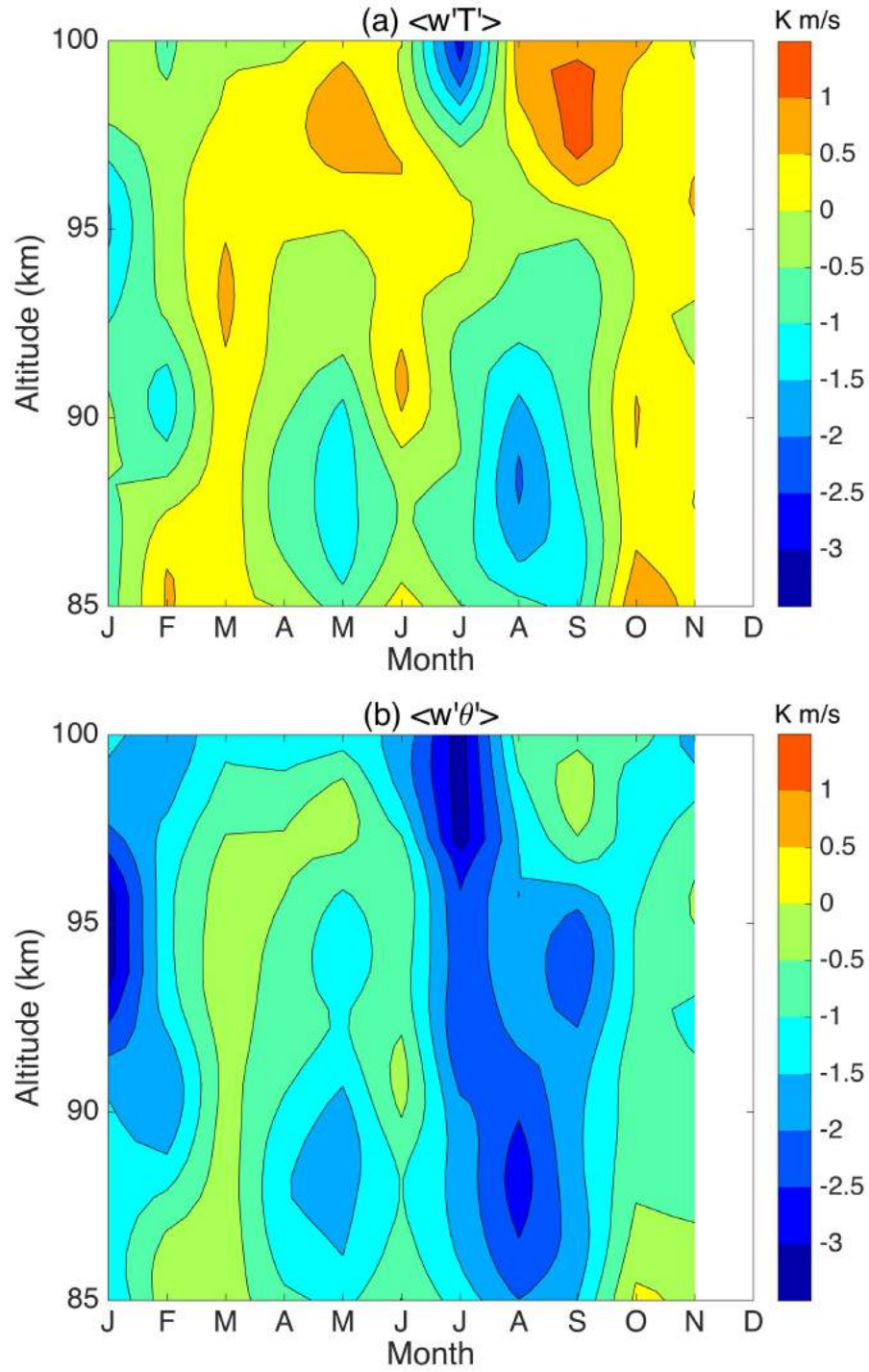


Figure 4.3: Seasonal variation of gravity wave vertical heat fluxes $\langle w'T' \rangle$ (a) and $\langle w'\theta' \rangle$ (b). The two heat flux are related through eq. (4.1).

fect generated by wave dissipation is characterized as the heating rate that can be calculated from sensible heat flux divergence:

$$\left. \frac{\partial T}{\partial t} \right|_{HF} = -\frac{1}{\bar{\rho}} \frac{(\bar{\rho} \overline{w'T'})}{\partial z} = -\frac{\partial \overline{w'T'}}{\partial z} + \left(\frac{g}{R} + \frac{\partial \bar{T}}{\partial z} \right) \frac{\overline{w'T'}}{\bar{T}}. \quad (4.4)$$

where ρ is the atmosphere density.

The seasonal and annual dynamical heating rates are shown in Figure 4.4. Monthly heating rate is calculated from Figure 4.3a. The strong cooling happens around southern hemisphere winter time between 87 to 97 km where substantial GW dissipation occurs. The local cooling rate due to heat flux divergence can exceed 30 Kd^{-1} during equinox in September. In the lower region of wave dissipation, the large upward sensible heat flux generates strong heating. The net effects can be seen from the annual profile in Figure 4.4b. In general, the heat transport caused by GW dissipation induces heating at the boundaries and considerable cooling in the mesopause region. The GW generated in the lower atmosphere and propagated upward reaching the mesosphere will experience dissipation because of the instabilities. Thus, the sensible heat flux maximizes at the altitude where the wave amplitude is the maximum. In consequence, the flux divergence results in cooling above this altitude and heating below. The net cooling can significantly influence temperature structure and cools down the mesopause, also the cooling is balanced by other heating sources, such as radiative heating, energy deposition, etc.

4.5 Heat Flux due to Different Scale Waves

In the mesopause region, atmospheric perturbations vary from small scale turbulence and gravity waves to large scale tides and planetary waves. These different scales contribute to the transports of heat, constituent, and momentum through different mechanisms, such as turbulent mixing, convective or dynamical instabilities [Gardner and Liu, 2014]. Knowing

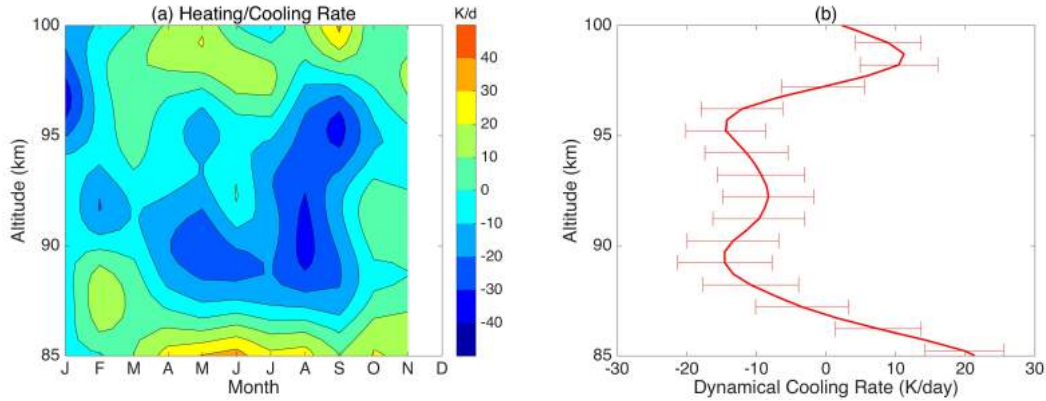


Figure 4.4: (a) seasonal and (b) annual dynamical heating/cooling rate associated with dissipating gravity wave induced heat transport. Mean dynamical cooling rate throughout the region is -6.7 Kd^{-1} with a uncertainty of 1.1 Kd^{-1} .

the contribution due to each mechanism will help us understand how waves influence the atmosphere. In the previous section, we have analyzed the transport induced by dissipating GWs over a relative broadband of spectrum. The derived GW perturbations applied to seasonal heat flux calculation consist of scales from a few minutes to 6 hours for periods and 1 km to 15 km for vertical wavelengths. Besides the total thermal impact of GWs on the atmosphere, understanding the fluxes caused by different scale GWs will also help with our knowledge of how different the wave activities and dissipations are for various frequency GWs in the mesopause region. In addition, for GWs, wave propagation depends on the wave frequency [Nappo, 2013]. High frequency waves tend to propagate more horizontally and air parcels oscillate more vertically, and vice versa. Based on this motivation, we derived the GW perturbations in terms of three different period intervals from the same dataset as describe in Table 4.1. The three intervals correspond to wave periods from 5 minutes to 1 hours, 1 hours to 3 hours, and 3 hours to 6 hours, where 5 minutes and 6 hours are the cut-off periods of for derived GW perturbations, same as the seasonal flux analysis. Vertical scale remains the same for each period interval in order to keep one dimensional consistent and get better comparison results, and also because vertical wavelength span

(~15 km) is more limited due to the thin Na layer. The method used to extract these three sets of perturbations is described in Section 4.2.

Shown in Figure 4.5 are the annual vertical fluxes calculated from three sets of GW perturbations with different periods. $\langle w'\theta' \rangle$ is calculated from the same algorithm as seasonal flux except that the integral intervals (ω_1, ω_2) in eq.(4.2) depend on the period intervals of extracted wave perturbations. Profiles in each plot represents the annual fluxes averaged through 105 nights of lidar observations. As seen from Figure 4.5b, $\langle w'\theta' \rangle$ are negative and exhibit downward heat transports for all three period intervals. The smallest enthalpy flux is from the long and medium period GWs with an average of -0.1 Kms^{-1} , while the heat flux induced by small period waves is much larger and contributes the most to the total heat flux.

Another dominate feature in the heat flux is that the altitudes where the maximum is located varies for different scale waves, which can be used to indicate wave propagation and dissipation characteristics. Table 4.2 summarizes the magnitudes and altitudes for the maxima in the heat fluxes in Figure 4.5a and Figure 4.5b. Since the vertical fluxes represent wave activities in the mesopause region, it is assumed that the downward flux is larger where strong wave dissipation happens. From the table we see that shorter period GWs contribute more to the heat transport and dissipate at higher altitude in the mesopause region, which means small scale waves propagate more upward into the MLT. The small and medium period waves, corresponding to higher frequency waves, have larger heat fluxes than long period waves, which is consistent with the theory that high frequency GWs oscillate more vertically.

Apart from the heat transport by gravity waves, the energy transport can be related to the wave total energy and energy flow velocity. The total energy density per unit volume is defined as

$$E_v = \frac{1}{2}\bar{\rho} \left[\overline{u'^2} + \frac{g^2}{N^2} \overline{\left(\frac{T'}{T}\right)^2} + \frac{1}{c_s^2} \overline{\left(\frac{p'}{\bar{p}}\right)^2} \right], \quad (4.5)$$

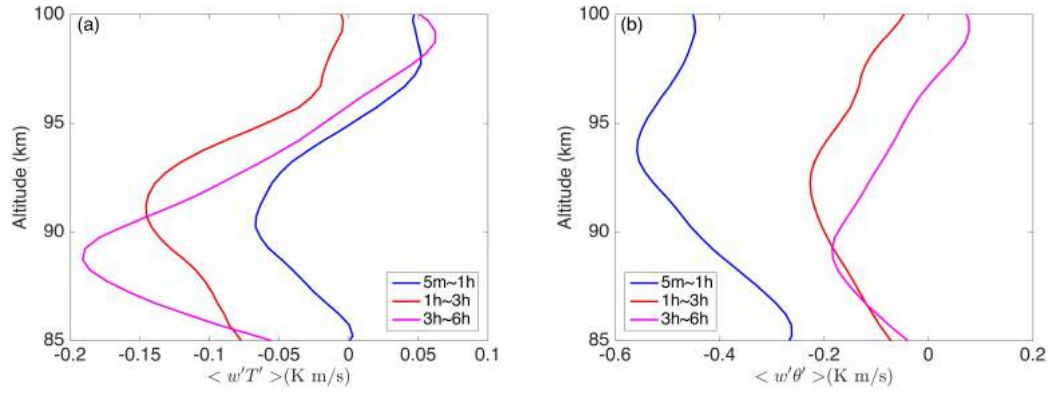


Figure 4.5: (a) sensible heat flux $\langle w'T' \rangle$ and (b) heat flux of potential temperature $\langle w'\theta' \rangle$ induced by gravity waves with different periods. Blue, red, and pink are related to waves with periods from 5 min to 1 hour, 1 to 3 hour, and 3 to 6 hour, respectively.

Table 4.2: Magnitudes and altitudes of downward maxima for vertical heat fluxes induced by gravity waves with different periods.

	5 m~1 h	1 h~3 h	3 h~6 h
$\langle w'T' \rangle$ (K m/s)	-0.07 @ 90 km	-0.15 @ 91 km	-0.19 @ 89 km
$\langle w'\theta' \rangle$ (K m/s)	-0.56 @ 93 km	-0.23 @ 92 km	-0.19 @ 89 km

where $\mathbf{u} = (u, v, w)$ is the velocity vector, u as the zonal wind, v as the meridional wind, $c_s^2 = \gamma R \bar{T}$ is the sound speed, and $\gamma = c_p/c_v$, c_p and c_v are the specific heats at constant pressure and volume, respectively. The first term on the right hand is the kinetic energy, the second term is the potential energy, the third term is the elastic potential energy, which is quite small compared to the other two terms [Walterscheid and Schubert, 1990; Walterscheid and Hickey, 2011]. The total energy per unit volume is $E_m = E_v/\bar{\rho}$. With the wave vertical energy flux F_z , the vertical component of energy flow velocity, which is equal to the wave vertical group velocity c_{gz} in the mesopause region [Vincent, 1984; Walterscheid and Hickey, 2011], can be calculated from:

$$c_{gz} = W = \frac{F_z}{E_v} = \frac{F_z}{\bar{\rho} E_m}. \quad (4.6)$$

Among the 105 nights of lidar observations, 81 nights are operated with off-zenith directions, so zonal and meridional winds (u and v) are calculated based on the LOS winds in the East and South directions. The horizontal wind perturbations (u' and v') are derived from the approach as vertical wind and temperature perturbations. (u', v', w') are then applied to calculate the kinetic energy and T' is used to calculate potential energy. Summarized in Table 4.3 are the mean energy per unit volume E_v , energy flux per unit volume $F_z/\bar{\rho}$, and vertical group velocity c_{gz} that are averaged through 85 to 100 km for three different scale range waves. Since F_z is exponentially decreasing with altitude due to the decreasing density (see Figure 4.2b), it is more straightforward to exclude the effect by calculating $F_z/\bar{\rho}$. It is obvious that the energy flux is largest for high frequency waves and smaller for low frequency waves. Energy decreases with wave period. The vertical group velocity can also be derived from the derivative of intrinsic frequency with respect to vertical wavenumber as [Fritts and Alexander, 2003]:

$$c_{gz} = \frac{\partial \hat{\omega}}{\partial m} = -\frac{m(\hat{\omega}^2 - f^2)}{\hat{\omega} \left(k^2 + l^2 + m^2 + \frac{1}{4H^2} \right)} \quad (4.7)$$

where k and l are horizontal wavenumber, f is inertial frequency, H is the scale height. Our results in Table 4.3 shows a good agreement with eq.(4.7) that c_{gz} increases with frequency. The average c_{gz} for high frequency, medium frequency, and small frequency waves are 3.9 ms^{-1} , 0.9 ms^{-1} , and 0.3 ms^{-1} , respectively. The group velocities are also consistent with the other observations [e.g. Vincent, 1984; Chen et al., 2013; Lu et al., 2015a].

Table 4.3: Mean vertical energy flux, total energy density per unit volume, and group velocity for gravity waves with different periods.

	5 m~1 h	1 h~3 h	3 h~6 h
$F_z/\bar{\rho}$ (J/kg· m/s)	426	78	22
E_m (J/kg)	113	93	76
c_{gz} (m/s)	3.9	0.9	0.3

The transport generated by waves can also be characterized by an effective velocity. This transport velocity is different for heat, energy, and constituents. In order to illustrate the importance of considering the energy flux term in heat flux calculation and the significant difference between the two heat fluxes, the three velocity terms in eq.(4.1) are calculated from annual fluxes and plotted in Figure 4.6. \bar{T} and $\bar{\theta}$ are calculated from temperature perturbations. \bar{p} is obtained from model MSIS-00. All three parts play important roles in the vertical transport in the mesopause region, which suggests that it is necessary to include the energy transport in evaluating the heat flux caused by dissipating GWs.

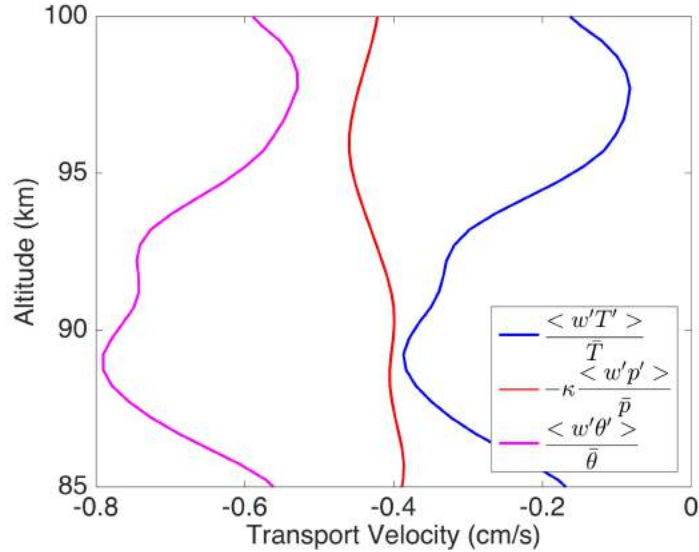


Figure 4.6: Transport velocities corresponding to three terms in eq. (4.1). Blue, red, and pink are corresponding to the first term, second term on the right side, and the left side, respectively.

4.6 Summary

In this chapter, we have presented the calculation of vertical heat and energy flux of dissipating GWs with a Na lidar at ALO. This is the first time that heat fluxes are measured in the southern hemisphere around the mesopause. Compared with the results reported in GL07, despite the reversed seasons, the same feature appears in both locations, the sensible heat flux is maximum during solstices and minimum around equinoxes, but the altitudes and magnitudes of maximal sensible heat flux are different. We have also analyzed the seasonal flux of potential temperature ($\langle w'\theta' \rangle$, enthalpy flux) and energy flux ($\langle w'p' \rangle$) for the first time. When the wave field consists primarily of upward propagating waves, the energy flux is positive, the enthalpy flux is either negative or zero depending on waves are dissipated or not. The sensible heat flux is also generally downward, except when there is no dissipation and then it is upward and proportional to the relative energy flux. Our

results show that the heat flux is downward throughout the region, which is consistent with the well known studies [Walterscheid, 1981a; Weinstock, 1983]. The downward heat transport generated by wave dissipation results in a significant cooling to the mesopause with a cooling rate at a maximum of 15 Kd^{-1} .

We have also investigated the contribution of different scale gravity waves in downward heat transport. Our results suggest that smaller period waves generate larger heat fluxes and dissipate at higher altitudes. The energy densities are largest for long period waves. However, the the largest vertical energy fluxes are found for short period waves. The upward energy flux decreases from 10^{-2} Wm^{-2} at 85 km to 10^{-4} Wm^{-2} at 100 km. This is probably the upper limit for the energy flux because it's calculated under the assumption that all waves are upward propagated. However, waves generated by instabilities in the mesopause region, reflected waves, ducted waves, and secondary waves can have downward energy flux. In general, gravity waves propagate upward with positive energy fluxes. The vertical group velocities inferred from energy flow velocity are consistent with the knowledge that high frequency waves propagate more vertically. The magnitudes of vertical group velocities are also the typical values that are observed by other instruments in the mesopause.

Overall, the thermal effects of dissipating gravity waves in the mesopause region have not been well established into wave parameterizations in general circulation models, which are primarily focusing on the wave drag of momentum flux. The measured heat flux and associated cooling rate, together with the vertical energy flux, can help us better understand the impacts of wave dissipation in the MLT and provide references for future wave parameterization in global models.

Chapter 5

Atmospheric Turbulence and Turbulent Heat Flux

This Chapter shows the first measurement of turbulence heat flux and turbulent key parameters in the mesopause region using the high-resolution ALO Na wind/temperature lidar. It is for the first time that the turbulence heat flux and associated cooling effect are calculated in the mesopause. The spectral characteristics and statistics of turbulence are analyzed as well. This study is based upon the work published in *Guo et al.* [2017].

5.1 Introduction

Turbulence is commonly generated by wave breaking in the MLT through convective and dynamic instabilities [e.g. *Hodges*, 1969; *Lindzen*, 1981; *Zhao et al.*, 2003; *Liu et al.*, 2004; *Williams et al.*, 2006; *Hecht et al.*, 2014]. Vertical transport by turbulence plays a fundamental role in establishing the thermal structure, composition and circulation of the mesosphere and lower thermosphere (MLT) below the turbopause [e.g. *Akmaev*, 2001; *Qian et al.*, 2009; *Zhu et al.*, 2010; *Garcia et al.*, 2016; *Meraner and Schmidt*, 2016]. This transport process is described as a mixing effect characterized by diffusion coefficients (also called diffusivity). Many studies have contributed to our knowledge of turbulence and its influence on the atmosphere. It is difficult to directly measure turbulence in the upper atmosphere because the turbulent eddies are small, with scales ranging from a few tens of meters to a few km, and the temperature, wind and density fluctuations associated with them are

too small to be observed from instruments. For the same reason, most atmospheric models cannot resolve turbulence scale motions, except with direct numerical simulation [Fritts *et al.*, 2014].

As mentioned in Chapter 1, the energy cascade process of turbulence is characterized by energy dissipation rate ϵ , a measure of how fast energy is dissipated to molecular scale. The transports of constituents, heat, momentum, and their mixing effects along with the process are represented by the diffusion coefficients often denoted as k_{zz} , k_H , and k_M , respectively. Until now, only the diffusion coefficient for inert constituents (k_{zz}) and turbulent energy dissipation rate (ϵ) have been measured, primarily by in situ observations of neutral density fluctuations and their power spectra such as rocket-borne ionization gauges [e.g. Lübken, 1997; Das *et al.*, 2009], by observations of the expansion of chemiluminescent trails released by rockets [e.g. Bishop *et al.*, 2004], and by measuring the spectral broadening of radar pulses caused by turbulence-induced wind fluctuations [e.g. Fukao *et al.*, 1994; Hocking, 1996]. The ionization gauge and radar techniques use turbulence theory to relate the observations to k_{zz} and ϵ , while the rocket trail technique is a direct measurement of the turbulent mixing of constituents. The thermal (k_H) and momentum (k_M) diffusion coefficients are usually inferred from k_{zz} by ignoring chemical effects and so that $k_H \approx k_{zz}$ and by assuming a value for the turbulence Prandtl number Pr so $k_M = k_H/Pr = k_{zz}/Pr$. Because of the large variabilities of these turbulence parameters [Lübken *et al.*, 1987], there is still considerable uncertainty about their values in the MLT.

In this work we show the first direct measurements of turbulence heat flux and the associated thermal diffusion coefficient with a narrow-band Na wind and temperature lidar located at Andes Lidar Observatory (ALO) in Cerro Pachn, Chile (30.25° S, 70.74° W). 150 h of lidar data from 19 nights of observations are used to derive the turbulence fluctuations associated with temperature and vertical wind. Turbulence heat flux and thus k_H are derived to characterize the heat transport and heating/cooling effect by turbulence. Energy

dissipation rate and associated heating are also calculated. These are also compared with the heat flux from dissipating gravity wave derived from the same data set. The capability to simultaneously measure both the wave- and turbulence-induced heat transport processes can provide important insights on the relationship between wave breaking and turbulence generation and their combined effects on the thermal balance of the mesopause region.

The results can provide innovative knowledge on the energy distribution of turbulence and the diffusive process relates to the wave breaking theory. The measured eddy heat flux and diffusion coefficient can be applied as reference values for the parameterization of gravity waves in general circulation models.

5.2 Key Parameters of Turbulence

Turbulence transport is usually modeled as a diffusive process, a larger-scale analogue of molecular diffusion. The vertical turbulence flux of sensible heat ($\overline{w'T'}$), is defined as the covariance between vertical wind (w') and temperature (T') perturbations induced by turbulence, same as the gravity wave sensible heat flux. The thermal diffusion coefficient k_H is defined in terms of the potential temperature θ as

$$\overline{w'\theta'} = -k_H \frac{\partial \bar{\theta}}{\partial z} = -k_H \left(\Gamma_{ad} + \frac{\partial \bar{T}}{\partial z} \right) \frac{\bar{\theta}}{\bar{T}}, \quad (5.1)$$

where $\Gamma_{ad} = g/C_p$ is the dry adiabatic lapse rate. $\overline{w'\theta'}$ can be expressed as eq.(4.1) through sensible heat flux $\overline{w'T'}$ and energy flux $\overline{w'p'}$.

Results from previous Chapter 4 show that $\overline{w'p'}$ plays important role in estimating the $\overline{w'\theta'}$. However, for turbulence, since $\overline{\theta'^2}/\bar{\theta}^2 \approx \overline{T'^2}/\bar{T}^2$ [Tatarskii, 1971; Gavrilov *et al.*, 2005], the second term on the right is assumed to be negligible [Becker and Schmitz, 2002].

Hence with eq. (5.1), k_H can be expressed as

$$k_H \approx -\frac{\overline{w'T'}}{\Gamma_{ad} + \partial\overline{T}/\partial z} = -\frac{g}{N^2} \frac{\overline{w'T'}}{\overline{T}}. \quad (5.2)$$

Thus k_H can be calculated from measured $\overline{w'T'}$.

In addition to $\overline{w'T'}$, the variance profiles of w' and T' ($\overline{w'^2}$ and $\overline{T'^2}$) can also be directly calculated from lidar measurements. These quantities have been applied to estimate turbulence parameters in observations based on turbulence theories [e.g. *Gavrilov et al.*, 2005; *Alexander and Barnet*, 2007; *Clayson and Kantha*, 2008; *Zhang et al.*, 2012]. Here we can use the variances and the turbulence heat flux measured from lidar to verify the consistency between them. *Weinstock* [1981] showed that for stably stratified turbulence, ε can be related to the variance of w' as

$$\varepsilon = C_0 \overline{w'^2} N, \quad (5.3)$$

where C_0 is a dimensionless constant with a theoretical value of $C_0 \approx \alpha^{-3/2} \approx 0.5$, and $\alpha \approx 1.5$ is the Kolmogorov constant.

With the assumption of $k_H \approx k_{zz}$, ε can be related to k_H according to *Weinstock* [1978] as

$$k_H \approx \frac{\pi^{1/2}}{4C_0} \frac{\varepsilon}{N^2}. \quad (5.4)$$

The variance of relative temperature perturbation $\overline{T'^2}$ is also related to ε according to *Gardner and Liu* [2016]

$$\frac{\overline{T'^2}}{\overline{T}^2} \approx \frac{4N}{g^2} \varepsilon. \quad (5.5)$$

Using these equations, we can then derive ε from eq. (5.3) and compare the measured $\overline{w'^2}$ and $\overline{T'^2}$ with those predicted by eq. (5.4) and eq. (5.5).

Similar to dissipating gravity waves, turbulent mixing also transports heat downward,

which generally cools the atmosphere. The associated heating rate is

$$-\frac{1}{\bar{\rho}} \frac{\partial (\bar{\rho} \overline{w'T'})}{\partial z} \quad (5.6)$$

and can be combined with the heating rate due to turbulence energy dissipation ε/C_p to derive the net heating or cooling of the atmosphere caused by turbulence.

5.3 Observations

The ALO Na Doppler lidar located in Cerro Pachón, Chile uses the three-frequency technique [Krueger *et al.*, 2015] to measure line-of-sight wind, temperature and Na density by detecting the thermal broadening and Doppler shift of sodium D2 line. The design architecture and performance specifications for this instrument are summarized in Liu *et al.* [2016]. For this study we employed 150 h of observations acquired during 19 nights when the lidar was pointed exclusively at zenith. The nights cover campaigns on May 2014 (2 nights), Aug 2014 (4 nights), Sep 2014 (7 nights), Jan 2015 (6 nights). Photon count signals were obtained at a temporal resolution of 6 s and a vertical resolution of 25 m. The procedures to derive turbulence fluctuations T' and w' are named as Signal Perturbation Method, which is modified from the method proposed by Gardner and Liu [2014]. The details are described in Section 5.4.

Even though the signal levels acquired by the ALO Na lidar are high, at these high resolutions required to resolve the turbulence fluctuations, the photon noise errors (Δw and ΔT) are still much larger than w' and T' . For example, the rms of w' is about 2 ms^{-1} , while the rms photon noise errors are $10\text{-}12 \text{ ms}^{-1}$. However, since we are interested in measuring the second order statistics of w' and T' (viz. covariance and variances), not their instantaneous values, the significant photon noise can be reduced by averaging long enough data to reduce the uncertainties of these statistics to acceptable levels.

Because the wind and temperature are derived from the same set of signals, their photon noises are correlated, which introduces a significant bias to their covariance. This bias, however, can be easily eliminated by cross-multiplying measured temperature and vertical wind perturbations, $T' + \Delta T'$ and $w' + \Delta w$, at two consecutive samples instead of from the same sample [Gardner and Liu, 2014], because the photon noises at two different times are uncorrelated. Variances of w' and T' are also calculated with the same approach. A trade off of this approach is the time resolution is reduced by a factor of two with an effective resolution of 12 s.

Although this technique eliminates the photon noise biases from the heat flux and variance calculations, unbiased photon noise is still the dominant error source for the measurements reported here. The uncertainties (in standard deviations) are

$$\begin{aligned}\text{Std}(\Delta w' T') &= \sqrt{\frac{\Delta z \Delta t}{2L\tau}} \text{Std}(\Delta w) \text{Std}(\Delta T), \\ \text{Std}(\Delta T'^2) &= \sqrt{\frac{2\Delta z \Delta t}{L\tau}} \text{Var}(\Delta T), \\ \text{Std}(\Delta w'^2) &= \sqrt{\frac{2\Delta z \Delta t}{L\tau}} \text{Var}(\Delta w),\end{aligned}\tag{5.7}$$

where $L = 2.5\text{km}$ is the vertical resolution of the final smoothed profiles and $\tau = 150\text{h}$ is the averaging period, while $\Delta z = 100\text{m}$ and $\Delta t = 6\text{s}$ are the sample resolutions of the turbulence heat flux and variances. Note, the factor of 2 arises in the heat flux uncertainty because two instantaneous heat flux estimates can be derived from the two sets of w' and T' values measured during the adjacent time bins.

5.4 Signal Perturbation Method

5.4.1 Theory

The modern three-frequency ratio technique is to tune the laser frequency to each of the three frequencies at f_a , $f_a + \Delta f$, and $f_a - \Delta f$, where f_a is the Na D_{2a} line peak frequency and $\Delta f = 630$ MHz (see details in Section 2). The raw lidar data is acquired under temporal and vertical resolutions of 6 s and 25 m, respectively, then integrated to 60 s and 500 m to derive temperature and light-of-sight wind with typical measurement errors of 1 K and 1 m/s. Temperature and wind are retrieved from the ratios defined as:

$$\begin{aligned} R_T &= \frac{N_+ + N_-}{N_0} \\ R_w &= \frac{\ln(N_-/N_+)}{\ln(N_-N_+/N_0^2)} \end{aligned} \quad (5.8)$$

where N_0, N_-, N_+ are photon count profiles at three frequencies. The definition of ratios are designed to be sensitive enough to obtain better temperature and wind measurements.

Gravity wave perturbations can be derived directly from temperature and wind profiles under 60 s and 500 m resolutions with rather high signal levels [*Gardner and Liu, 2007*]. However, for turbulence, it requires much higher temporal and vertical resolutions since turbulences are in the scales of seconds and meters to a few minutes and hundreds of meters. A new method was developed to derive the wind, temperature, density turbulent perturbations directly from the concomitant photon count perturbations with linearized system equations [*Gardner and Liu, 2014*]. Here the method proposed in *Gardner and Liu [2014]* is revised by using the fluctuations of ratios instead of photon counts, which is more reasonable considering the conventional scheme to derive temperature and wind in lidar data processing. This new method also eliminated the effects of sporadic Na layers and

named as Signal Perturbation Method (SPM).

Due to the dependence of R_T and R_w on temperature and wind, it is possible to write the ratios through Taylor expansion as follows:

$$\begin{aligned} R_T &= \overline{R_T} + \frac{\partial R_T}{\partial T} T' + \frac{\partial R_T}{\partial w} w' + \frac{1}{2} \frac{\partial^2 R_T}{\partial T^2} T'^2 + \frac{1}{2} \frac{\partial^2 R_T}{\partial w^2} w'^2 + \frac{\partial^2 R_T}{\partial w \partial T} w' T' \dots \\ R_w &= \overline{R_w} + \frac{\partial R_w}{\partial T} T' + \frac{\partial R_w}{\partial w} w' + \frac{1}{2} \frac{\partial^2 R_w}{\partial T^2} T'^2 + \frac{1}{2} \frac{\partial^2 R_w}{\partial w^2} w'^2 + \frac{\partial^2 R_w}{\partial w \partial T} w' T' \dots \end{aligned} \quad (5.9)$$

where prime denotes the perturbation. If we only consider the first derivatives and the relationships become linear:

$$\begin{aligned} R'_T &= R_T - \overline{R_T} = \frac{\partial R_T}{\partial T} T' + \frac{\partial R_T}{\partial w} w' \\ R'_w &= R_w - \overline{R_w} = \frac{\partial R_w}{\partial T} T' + \frac{\partial R_w}{\partial w} w'. \end{aligned} \quad (5.10)$$

Thus, T' and w' can be solved as:

$$\begin{bmatrix} R'_T \\ R'_w \end{bmatrix} = \begin{bmatrix} \frac{\partial R_T}{\partial T} & \frac{\partial R_T}{\partial w} \\ \frac{\partial R_w}{\partial T} & \frac{\partial R_w}{\partial w} \end{bmatrix} \begin{bmatrix} T' \\ w' \end{bmatrix} \Rightarrow \begin{bmatrix} T' \\ w' \end{bmatrix} = \begin{bmatrix} \frac{\partial R_T}{\partial T} & \frac{\partial R_T}{\partial w} \\ \frac{\partial R_w}{\partial T} & \frac{\partial R_w}{\partial w} \end{bmatrix}^{-1} \begin{bmatrix} R'_T \\ R'_w \end{bmatrix}, \quad (5.11)$$

where R_T and R_w are first calculated from N_0 , N_- , N_+ with equation (5.8). Then ratio fluctuations R'_T and R'_w are derived by first applying a two dimensional Hamming window with temporal FWHM of 2.5 min and spatial FWHM of 500 m on R_T and R_w profiles, and the remaining is considered as fluctuations associated with small scale structures. The inversed matrix based on effective cross section is defined as sensitivity coefficients that can be calculated from lower resolution profiles with gravity wave scales. Then the coefficients are interpolated into the same grids of as R'_T and R'_w for multiplication. Thus, the turbulent fluctuations contain scales smaller than 5 min and 1 km. The gravity waves are derived from a similar approach but the filtering is applied directly on temperature and vertical

wind with scales larger than 5 min and 1 km, which makes the separation for gravity wave and turbulence at 5 min and 1 km.

The 5 min and 1 km are chosen based on the fact that the smallest GW vertical (and horizontal) wavelengths are ~ 1 km and the highest frequencies are near buoyancy frequencies in the mesopause region [*Blix et al.*, 1990; *Gardner et al.*, 1993; *Lu et al.*, 2015b]. Even though it is certainly possible to have gravity wave fluctuations with earth-fixed frequencies larger than the Brunt-Väisälä frequency (N) because of the Doppler shift effects, observations have shown that in the mesopause region, most high frequency gravity waves propagate against the background wind. Their observed frequencies are therefore smaller than N , the upper limit of their intrinsic frequency. For the small fraction of GWs with higher than N ground frequencies, the effect of including them in the turbulence calculation is very small. This is best illustrated by the observed frequency spectrum of GW vertical winds plotted in Figure 2 of *Gardner et al.* [1993]. This plot was derived by assuming that the GW propagation directions are isotropic and therefore it represents a worst case because it is now well known that GWs tend to propagate against the mean flow. This means that there is a strong bias towards shifting GW energy to lower, not higher frequencies. However, as seen in this figure (note this is a log-log plot), for a worst-case isotropic wave spectrum and horizontal velocities as high 80 m/s (i.e. ≈ 2 where $N/m^* \sim 12$ km/300 s=40 m/s), only a very small fraction of the vertical wind energy (\sim several %) is shifted to frequencies higher than N . At Cerro Pachón, the horizontal winds are typically about 20 m/s so that ~ 0.5 . Thus at most, our measured vertical wind variance and ε , the turbulence energy dissipation rate, are enhanced by a few % because of the Doppler shifted GW energy. Note that the vertical wind variance associated with turbulence (~ 4 m²/s²) is comparable to the vertical wind variance associated with GWs (~ 4 m²/s²) so a few % of the GW w variance is comparable to a few % of the turbulence w variance. The same is true for the eddy heat flux contamination by GWs.

Its also worth noting that not only the contamination is small, but this small contamination does not affect the combined heat flux of GWs and turbulence, which is ultimately what we are interested in. While a clear-cut separation between GWs and turbulence is not possible, and may result in a few % error in the estimate of each flux, it does not affect the total flux due to both.

For the vertical wavelength of GWs, our choice of 500 m is suitable according to other observational studies. For example, *Lu et al.* [2015b] found out that GWs with wavelengths larger than 2 km could contribute up to 75% of the total potential energy between 85 to 100 km. *Blix et al.* [1990] showed that the transition between -3 and $-5/3$ is at around 500 m in the region of 63.7-72.1 km. So its reasonable to assume that wavelength at 1 km is an appropriate cutoff number for gravity waves and turbulence. Again, a clear separation is not possible and the contamination to either the GW or turbulence flux is very small.

5.4.2 Verification

In order to verify the SPM in deriving wind and temperature perturbations, SPM is applied to the lidar under gravity wave scales, and compared with the traditional derived perturbations. For this test, R_T and R_w were smoothed with 3 hour and 3 km FWHM Hamming windows and the residuals R'_T and R'_w are associated with GW fluctuations and used to calculate GW T' and w' , which are compared with the directly calculated T' and w' from T and w using the same smoothing scales. Figure 5.1 shows the direct comparison between gravity wave temperature and vertical wind perturbations by using the two different methods. The perturbations are on Sep 6th 2014 at 92 km where signal is the highest. It is clear that the perturbations derived from both methods are very consistent. Shown in Figure 5.2 are the scatter plots of the same data in Figure 5.1. Results present strong correlation between these two methods. The magnitude of temperature perturbations is within 10 K; vertical wind perturbations are less than 5 m/s.

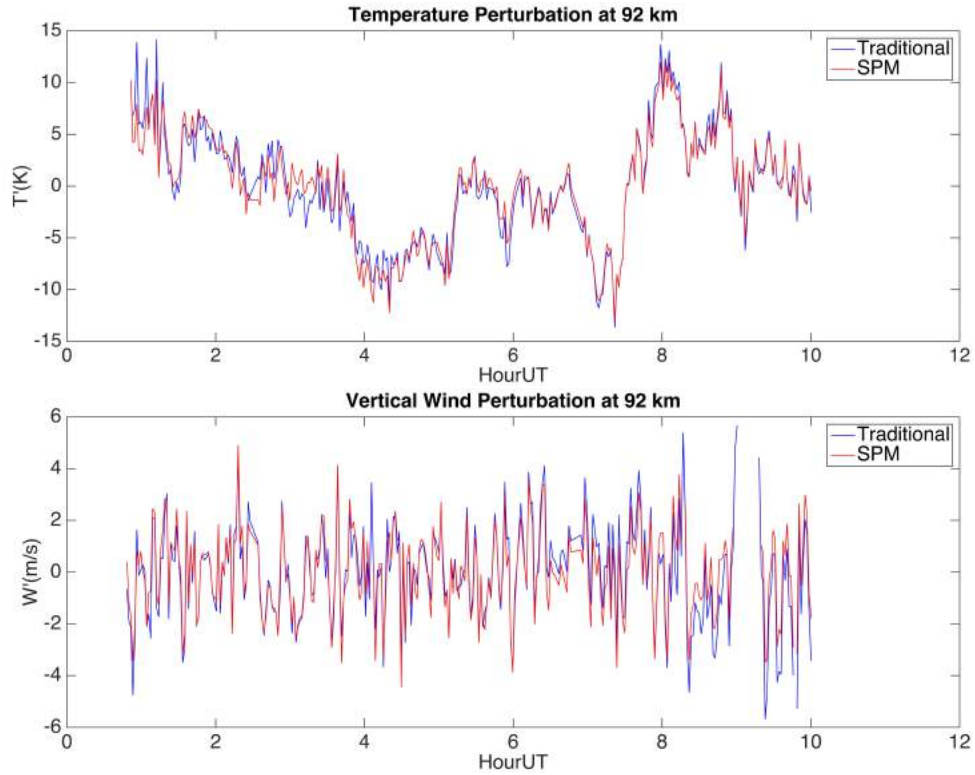


Figure 5.1: Gravity wave temperature (top) and vertical wind (bottom) perturbations derived from traditional (blue) and SPM (red) throughout the night on September 6th, 2014 at 92 km. The overall structure matches well between the two different methods.

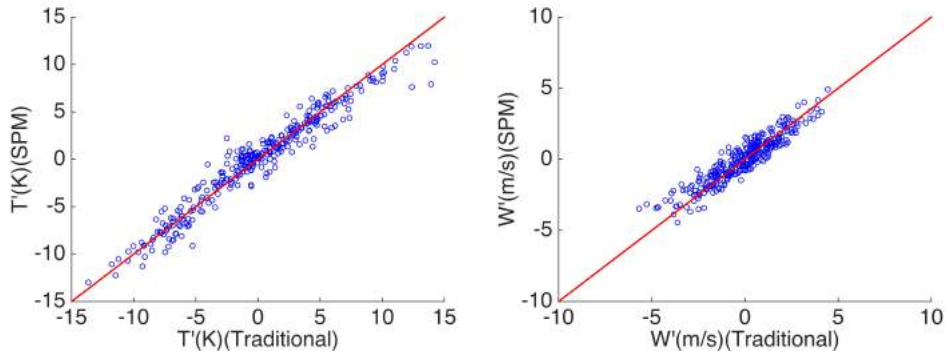


Figure 5.2: Scatter plot of gravity wave temperature (left) and vertical wind (right) perturbations derived from traditional (blue) and SPM (red) on September 6th, 2014 at 92 km.

To further verify this method, the temperature frequency spectra of the perturbations are also examined as shown in Figure 5.3. It shows that in the lower frequency region, all spectra are similar. The SPM can extend the spectra further to higher frequencies, and thus help identify the noise floor in the high frequency region. This is useful for error analysis.

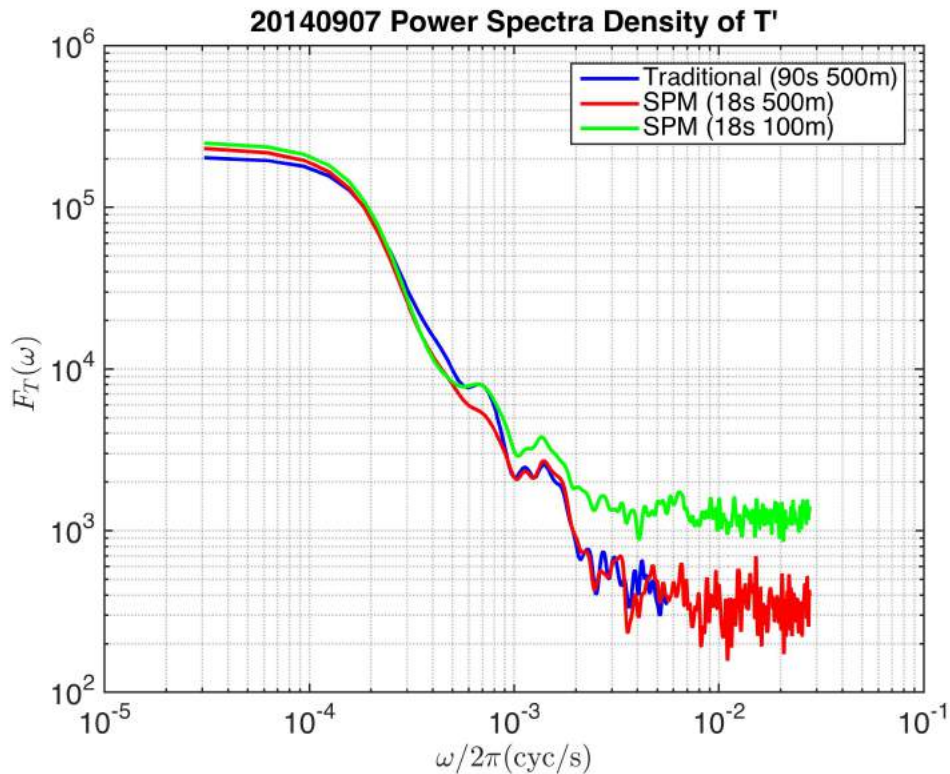


Figure 5.3: Power spectra density of temperature perturbation (T') on Sep 7th, 2014. The curves represent the frequency spectra derived from SPM and traditional method in three different sets of resolutions.

5.5 Turbulence Power Spectra

Several theoretical models have been developed for the gravity wave spectra, including the linear stability [Dewan and Good, 1986], Doppler spreading theory [Hines, 1991], and the diffusive theory [Weinstock, 1990]. There are numerous observations of gravity wave spectra made with a variety of techniques including balloon-borne sensors in the

troposphere and lower stratosphere [e.g. Zhang *et al.*, 2006], mesosphere-stratosphere-troposphere (MST) radar [e.g. Fritts *et al.*, 1988], VHF radar [e.g. VanZandt *et al.*, 1991; Larsen *et al.*, 1987], and Na lidar [e.g. Senft and Gardner, 1991] in the mesosphere. Here we show that the Na lidar can extend the spectra measurement into the turbulence scales.

The high-resolution ALO Na lidar measurements cover the ranges of frequency (ω) and vertical wave number (m) that include both gravity wave and turbulence scales. The temporal and vertical resolutions are 60 s and 500 m for gravity waves and 6 s and 25 m for turbulence. The ω -spectrum was calculated from temperature perturbations on each night averaged from all altitudes, and the m -spectrum was calculated in the 85-100 km altitude range for each profile, then averaged for the entire night.

Shown in Fig.5.4 are the turbulence spectra on 6 selected nights for relative temperature perturbations. Spectra are plotted as single-sided power spectra in the units of $(\text{cycles/km})^{-1}$ and $(\text{cycles/s})^{-1}$ for m and ω , respectively. Because turbulence has a large variety on different nights and different seasons, also photon noise depends on signal levels and changes nightly, it is common to see turbulence spectra with various magnitudes. However, overall the spectra follows a power law distribution with similar slopes for all nights. Noise floor are subtracted for further fittings.

Figure 5.5 shows the comparison between theoretical spectra (dashed colored lines) from theoretical models [Gardner *et al.*, 2014] and the observational spectra (solid colored lines) from lidar measured fluctuations (i.e. relative temperature fluctuations). The observed spectra were averaged from all nightly mean spectra after the noise floors were subtracted. Slopes and their uncertainties were estimated by linear regression. Black dashed lines represent the data points applied to the linear fitting. The Buoyancy frequency N ($\sim 2\pi/5$ min) in the ω -spectra plot represents the separation between gravity waves and turbulence.

The gravity wave spectra agree well with the theoretical m^{-3} and ω^{-2} power laws,

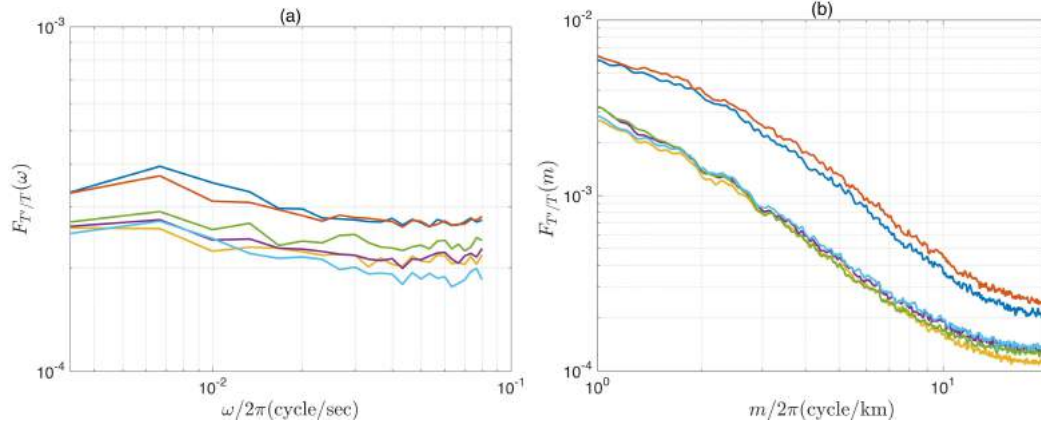


Figure 5.4: Nightly (a) temporal frequency (ω) and (b) vertical wave number (m) spectra of relative temperature turbulent perturbations. Each colored line represents spectra on one night.

with the slope for ω slightly steeper than the theoretical value. In the turbulence spectra, the noise floor starts at about 10 km^{-1} (or 100 m) in the m -spectrum and 0.05 s^{-1} (or 20 s) in the ω -spectrum. Both turbulence m -spectrum and ω -spectrum are consistent with the theoretical value of $-5/3$ with slopes of -1.73 ± 0.01 and -1.71 ± 0.14 , respectively. Overall, there is a good agreement between the measured and theoretical spectra. The fact that the slopes can be clearly identified in the turbulence scales indicate that the ALO Na lidar is sensitive to turbulence perturbations and can detect them well above the noise floor.

5.6 Turbulence Measurements

The measured turbulence heat flux $\overline{w'T'}$ is shown in Figure 5.6(a). It is negative throughout the region, indicating that turbulent mixing transports heat downward. The magnitude in general decreases with increasing altitude from about -0.5 Kms^{-1} at 85 km to -0.1 Kms^{-1} at 100 km , with a local maximum at 93 km of -0.6 Kms^{-1} . The k_H profile shown in Figure 5.6b also exhibits a general decrease with increasing altitude, from $52 \text{ m}^2 \text{ s}^{-1}$ at 85 km to $10 \text{ m}^2 \text{ s}^{-1}$ at 100 km , with a local maximum of $71 \text{ m}^2 \text{ s}^{-1}$ at 93 km .

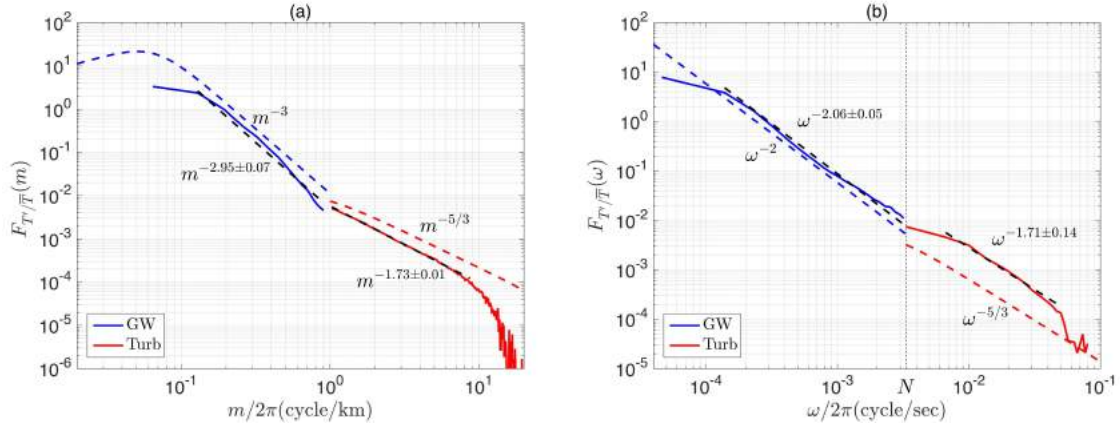


Figure 5.5: (a) Vertical wave number (m) and (b) temporal frequency (ω) spectra of relative temperature perturbations due to gravity waves (blue) and turbulence (red). Blue and red dashed lines represent the spectra predicted from theoretical models; solid lines are measured from high resolution lidar measurements; black dashed lines represent the data used for fitting.

These measured k_H values are generally consistent with the k_{zz} values measured by other techniques in other latitudes [e.g. *Lübken, 1997; Das et al., 2009; Bishop et al., 2004*] and larger than the k_{zz} values used in WACCM (Whole Atmosphere Community Climate Model) which has a maximum of about $20\text{m}^2\text{s}^{-1}$ [*Smith, 2012, Fig.7*]. ϵ was calculated based on eq.(5.3) and is shown in Figure 5.6c. The average ϵ between 85 and 100 km is about 37mWkg^{-1} , which corresponds to an average heating rate of about 3.2Kd^{-1} .

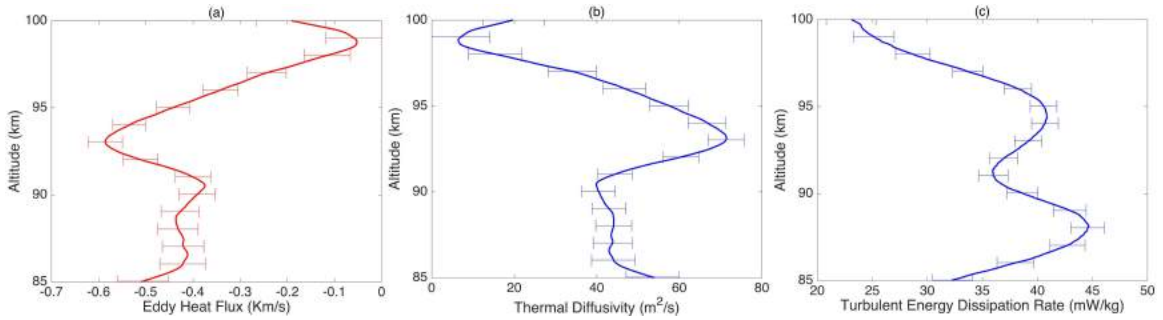


Figure 5.6: (a) Vertical eddy heat flux, (b) thermal eddy diffusion coefficient k_H , and (c) energy dissipation rate ϵ calculated from lidar measurements.

With the measured variances, we can examine the suitable value of C_0 in eq.(5.3). We calculated the variances $\overline{w'^2}$ and $\overline{T'^2}$ predicted by eqs. (5.4) and (5.5) using k_H in Figure 5.6(b) and compared them with directly measured variances. The Brunt-Väisälä frequency is calculated with the mean temperature. We found that when the theoretical value $C_0 = 0.5$ was used, the predicted variances are too small compared with observed values. *Weinstock* [1981] obtained an empirical value of $C_0 = 0.37$ based on experimental data from *Heck et al.* [1977]. We also found that using $C_0 = 0.37$ gives a better agreement with the measured variances. The results are plotted in Figure 5.7. Overall, the agreement is good for both $\overline{T'^2}$ and $\overline{w'^2}$, and the differences are smallest around 93 km where the flux and k_H are the largest. Our observation therefore supports the notion that the actual C_0 is likely less than 0.5 for the mesopause region.

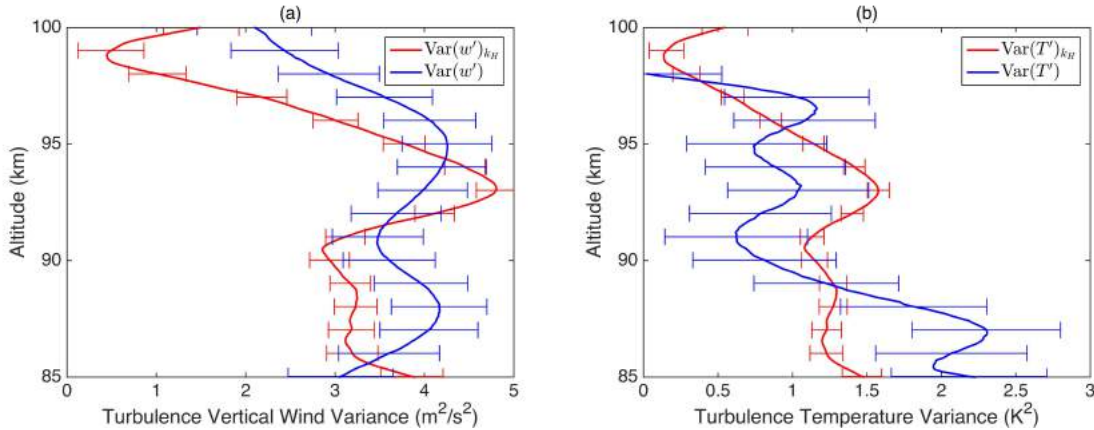


Figure 5.7: (a) Turbulence-induced vertical wind variance and (b) turbulence-induced temperature variance measured from lidar observations (blue) and calculated using the k_H values (red) in Figure 5.6b and eq.(5.5) with a C_0 value of 0.37.

To place the turbulence measurements in perspective, the profiles of gravity wave-induced heat flux, wind and temperature variances were also calculated from the same dataset and plotted in Figure 5.8. As expected the gravity wave sensible heat flux is also downward [*Walterscheid, 1981a*]. Its magnitude is similar to the eddy heat flux but the profile shape is different. The gravity wave heat flux increases from about -0.4 Kms^{-1} at

85 km, reaching a maximum of about -0.9 Km s^{-1} near 89 km and then decreases to essentially zero above 96 km. This behavior is similar to that observed at the Starfire Optical Range, NM (35.0° N , 106.5° W) [Gardner and Liu, 2007]. The wave- and turbulence-induced vertical wind variances (Figure 5.7a and Figure 5.8b) are comparable but the wave-induced temperature variance (Figure 5.8c) is about 50 times larger than turbulence-induced variance (Figure 5.7b). Although the magnitudes of temperature variances are much different, the overall profiles are similar. Both temperature variances exhibit maximum near 87 and 88 km and minimum above 96 km. This is probably related to the convective or static stability of the atmosphere, which is generally more stable above the mesopause where the vertical temperature gradient becomes positive. The turbulence-induced temperature perturbations are strongest at about the same altitude range where wave activity is the most energetic, and are weakest where wave activity is the least energetic, which is consistent with the notion that turbulence is mostly generated by wave breaking.

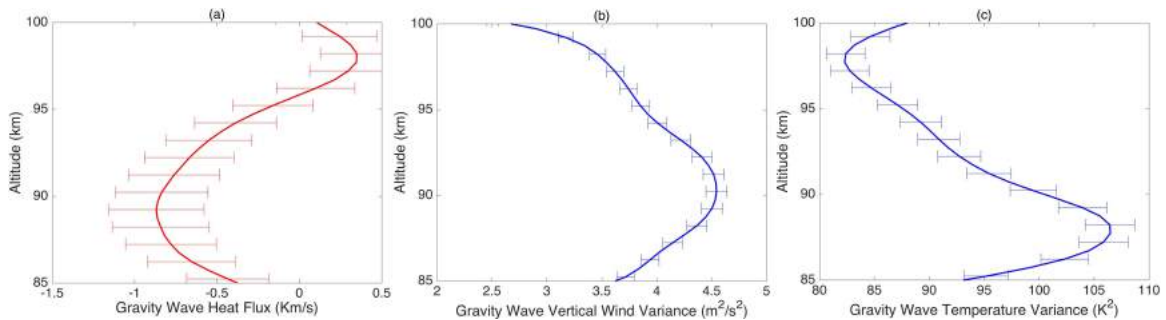


Figure 5.8: (a) Vertical gravity wave heat flux, (b) wave-induced vertical wind variance and (c) wave-induced temperature variance computed from the same lidar measurements used to derive the turbulence parameters shown in Figure 5.6.

In terms of the thermal effect of turbulence, it is well known that the turbulent energy deposition induces a heating to the background atmosphere. By using in situ rocket measurements, Lübkens [1997] found out that the heating rates corresponding to energy dis-

sipation rate ε is stronger in summer mesopause and much smaller in winter, varying from 1 Kd^{-1} to $10 \sim 20 \text{ Kd}^{-1}$. He also pointed out that this heating has to be compensated by other cooling mechanisms. While the cooling effect caused by gravity wave downward heat transport has been studied with simulations and observations [e.g. *Gardner and Yang, 1998; Gardner and Liu, 2007; Hickey et al., 2011*], the cooling caused by turbulence has only been estimated by a few numerical simulations [*Liu, 2000; Zhu et al., 2010*]. Our results show that the downward heat flux induced by turbulence induces a significant cooling effect to the MLT as well. Shown in Figure 5.9 are the cooling/heating rates due to turbulence and gravity wave heat transport (eq. (5.6)) and turbulent energy dissipation. The flux convergence associated with turbulence heat transport results in a cooling of the atmosphere with an average of -8.1 Kd^{-1} . This cooling more than balances the heating caused by turbulent energy dissipation of about 3.2 Kd^{-1} so that the total effect of turbulence is a cooling of the mesopause region of -4.9 Kd^{-1} . Wave-induced heat transport also causes a more significant cooling between 87.5 and 98 km. However, the large wave flux convergence below 87.5 km results in a strong heating of the atmosphere. Thus, the net effect of gravity waves and turbulence between 85 and 100 km is primarily dynamical cooling, with a maximum of about -32 Kd^{-1} near 95 km, and a mean of -12.8 Kd^{-1} .

5.7 Summary and Discussion

The transport of heat, momentum, and constituents by turbulence diffusion in the MLT region plays a very significant role in establishing the general circulation and thermal structure of atmosphere. It is well recognized that different chemical species are well mixed by this eddy diffusion process below turbopause and the eddy diffusivity k_{zz} is the same for all species. Currently, numerous ground-based and in situ observational techniques estimate k_{zz} indirectly from measuring the energy dissipation rate (ε) with uncertainties remain in

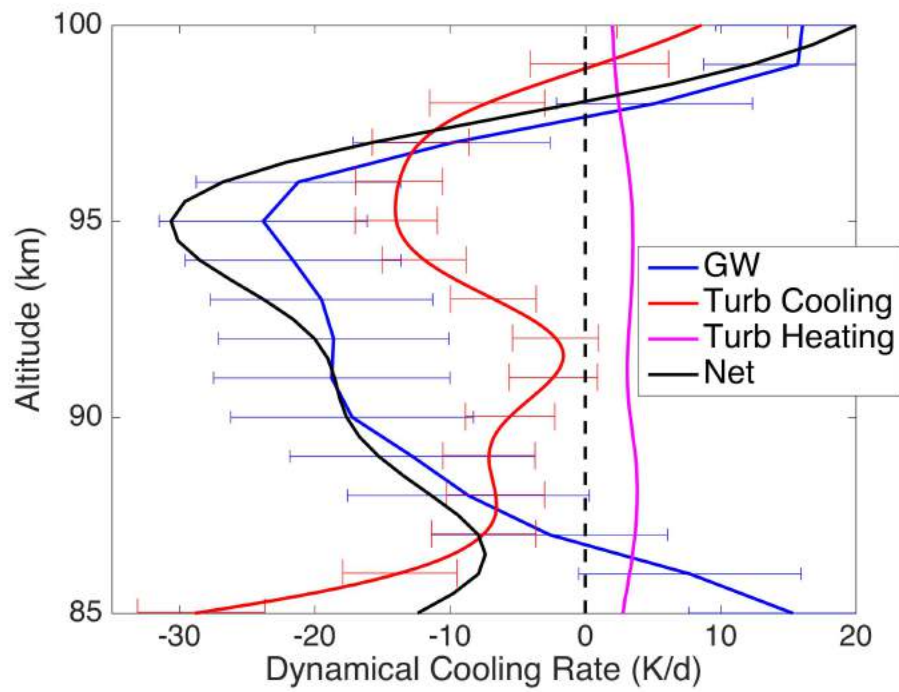


Figure 5.9: Atmospheric heating/cooling rates associated with vertical heat transport by turbulence (eq. (5.6)) and waves.

estimating ε and determining the dependence of k_{zz} on ε . These uncertainties can affect the measurements of k_{zz} by 2 – 3 orders of magnitude [Vlasov and Kelley, 2014, 2015]. Also the discrepancies between these observational coefficients and coefficients used in general circulation models suggest the necessity for a more effective way to determine k_{zz} .

In this chapter we showed that the Na wind/temperature lidar at ALO is now capable of detecting turbulence scale perturbations and providing direct measurements of the eddy heat flux and thermal diffusion coefficient k_H . For the first time, k_H is directly derived from eddy heat transport. Other key parameters such as the energy dissipation rate and the associated heating rate are also derived from the measurements without resorting to complex turbulence theory. The measured k_H has an average of $43 \text{ m}^2 \text{ s}^{-1}$ and a maximum of $72 \text{ m}^2 \text{ s}^{-1}$ at 93 km, and generally decreases with altitude above, which is consistent with some other results of k_{zz} measured by balloons and rockets. These results could provide significant references for the gravity wave parameterization in general circulation models such as WACCM, in which the k_{zz} varies between 10 to $20 \text{ m}^2 \text{ s}^{-1}$ in the mesopause region [Smith, 2012], much less than our results.

Another advantage of this high-resolution lidar technique is that both turbulence and gravity waves perturbations can be measured at the same time so that the transport induced by gravity wave and turbulence can be easily compared, as well as the characteristics of both gravity waves and turbulence (i.e. variance). Our results suggest that the downward heat fluxes are comparable for waves and turbulence, and the corresponding net cooling rate of 12.8 K d^{-1} can bring substantial cooling effects to the mesopause region, which was only studied by numerical simulations before.

The spectral analysis, along with the temperature and wind variance, confirmed the consistency between measured turbulent parameters and turbulence theory, also suggests that the value of the undetermined constant C_0 in the turbulence theory is likely to be smaller than the theoretical value of 0.5, supporting the value of 0.37 suggested by We-

instock [1981]. Note that it is not possible to have a clear cut separation between gravity waves and turbulence. In this analysis, our choice of 1 km is based both on past observational studies, as well as our spectral analysis (Fig. 5.5a). Furthermore, the turbulence outer scale, estimated using eq.(7) in *Gardner and Liu* [2014] with our derived energy dissipation rate of about 40 mW/kg (Fig. 5.6c) and $N^2 = 4 \times 10^{-4} \text{ s}^{-2}$, is about 700 m, which is consistent with the 1-km breakpoint between gravity waves and turbulence. These results further prove that the lidar measurements can indeed capture at least a large portion of turbulence fluctuations. This is an important advancement that will enable the studies of neutral atmosphere turbulence processes and gravity wave dynamics and their impacts on the atmosphere in the MLT region.

Charactering turbulence from observations has always been a challenge due to the large variation of gravity wave activities. The turbulent parameters also exhibit strong seasonal variations [e.g. *Lübken*, 1997; *Hall et al.*, 1999; *Sasi and Vijayan*, 2001]. Thus relatively long averaging periods (~ 100 h) are necessary to measure turbulence parameters, especially the second-order statistics such as flux and variance. The current ALO Na lidar is equipped with 70 cm diameter telescopes and with a power-aperture product of 0.6 W m^2 , which is typical for modern lidar systems. Here in this work, we only use 150h observational data on 19 nights. With more data acquired through different seasons in the future, the results are expected to vary. By employing larger telescope receiving systems with efficient optical designs [*Smith and Chu*, 2015] and higher power lasers, the required averaging times and uncertainties can be reduced substantially, and the data will have a more complete coverage of turbulence spectra. The current results show that even existing lidar systems are now capable of characterizing the seasonal variations of the vertical eddy heat transport and the diffusion coefficient, and its impacts on the thermal balance in the mesopause region.

Finally, assuming the turbulence fluctuations are approximately isotropic, the radial

wind variance would be comparable to the vertical wind variance. Therefore, our results also indicate that it is possible for existing Doppler lidars to measure turbulence momentum flux and turbulent Prandtl number by using off-zenith measurements to retrieve turbulence horizontal wind perturbations with the same data processing technique used in this study.

Chapter 6

Conclusion

6.1 Summary

The dynamics of MLT are dominated by the effects of atmospheric waves, including planetary waves, tides and gravity waves with sources from lower atmosphere. The basic structure of MLT is driven by its general circulations, which are largely influenced by these wave motions. Transport induced by gravity waves, tides, and planetary waves has long been an important research subject and plays significant roles in establishing the thermal structure and composition distributions in the MLT. Gravity waves that originated from lower atmosphere contribute to the transport by depositing energy and momentum into the background atmosphere as they propagate upward into the MLT where instabilities and breaking happen. Consequently, the forcing generated by the momentum deposition drives the circulation from the summer to winter pole in the MLT while the energy deposition leads to a heating effect on the atmosphere. In addition, dissipating gravity waves typically induce a downward heat transport resulting in substantial cooling of the middle atmosphere as heat is transported to lower altitudes. The wave breaking also generates turbulence that can transport momentum, energy, heat and constituents through turbulent mixing, which can influence the MLT structure as well.

In order to better understand the thermal effects of dissipating and breaking gravity waves, the heat transport and energy deposition by gravity waves and turbulence are investigated here. Research presented in this dissertation has been focused on characterizing

the vertical heat transport induced by different scale gravity waves and turbulence. The observations were made using data from the Na lidar located at ALO (30.25° S, 70.74° W) in Cerro Pachón, Chile between 2014 and 2016. These data were acquired with newly upgraded high-power lidar system with high temporal and vertical resolutions. The results shown here demonstrates the new capabilities of ALO Na lidar system in making continuous high quality measurements to enable a more comprehensive understanding of the effects of gravity waves and turbulence on the MLT thermal structures and dynamics.

There are three parts of this work as described in chapters 3 to 5. The first part is the calibration of the photo-multiplier tube (PMT) and the effects of PMT nonlinearity in calculating the vertical heat flux from lidar observations. The data applied to the analyses of vertical heat fluxes consist of observations made after the significant upgrades in May 2014, when the old ring dye laser was replaced with a high-power solid state laser and a more effective receiving system was installed. The upgrades resulted in great improvements of the signal levels, accompanied with the severe saturation effects of the PMT nonlinearity. The original PMTs installed in the lidar receiver are Hamamatsu H7421-40 models for signals at all three directions. On July 17th, 2015, the PMTs in Zenith and East were replaced with two newer PMTs of model H7421-M, while the South direction is not changed. The new PMT is equipped with higher maximum count rate and larger linear range, which is necessary for the updated lidar system with much higher signals. For most applications, a laboratory-measured correction will suffice because PMTs normally operate at low count rates not too far beyond the linear range. Under high count rates, inaccurate calibration of PMT nonlinear effect will bring bias into the lidar measurements of temperature, wind, and Na density. Strong correlation between large Na density (equivalent to the signal level) and temperature/wind anomalies are observed frequently in the data, suggesting that the PMT nonlinearity were not properly-corrected. With the new PMT settings at different directions, it is possible to first calibrate the PMT saturation effects on the measurements

and obtain more accurate correction to be applied for data processing. Apart from the significant error in the lidar measurement when severe saturation occurs, this inaccurate PMT nonlinearity correction curves can also cause bias in the heat flux calculations, because of the intrinsic correlation between temperature and wind errors. A numerical method was used to investigate this bias. Key results are summarized below:

- Starting from the laboratory-measured PMT correction curves, the relationship between temperature bias and PMT count rate can be determined analytically with traditional data processing. Then the relationship is applied to the lidar data to calibrate the laboratory-measured curves.
- An over-corrected curve will induce higher temperature and more negative winds, while a under-corrected curve will cause lower temperature and shift winds to positive direction. The comparison between original and reprocessed temperature and wind measurements show that the old PMT with model H7421-40 was originally over-corrected, while the new PMT H7421-M was under-corrected.
- The heat flux bias introduced by the PMT correction error is significant and tends to be negative, which will lead to positive heat flux calculation. The bias is theoretically estimated through simulations with the original and calibrated PMT correction curves and also showed up in the observational measurements.

With the calibrated PMT corrections curves, the lidar data was reprocessed and used for further analysis. The second work in Chapter 4 studies the vertical transports of heat and energy generated by dissipating gravity waves in the mesopause region with over 400 hours of vertical wind and temperature lidar measurements. Multiple observations, numerical simulations, and theoretical analysis have shown that the dissipating gravity waves can lead to substantial downward heat transport in the MLT where gravity waves experience

instability and breaking frequently. The associated cooling can reach tens of K per day. Besides the vertical heat flux, energy flux is also an important quantity used to characterize the gravity wave propagation and dissipation. The energy deposition process caused by wave breaking transfers the energy from waves into heat and deposit into the background. The combined heating and cooling effects can influence the atmospheric thermal structure and are one of the key features needed to be accounted during gravity waves parameterizations in the general circulation models. The gravity wave heat flux is a statistical parameter and calculated as the covariance between vertical wind and temperature perturbations. Perturbations are derived from nightly lidar wind and temperature measurements. Observations are grouped into different months for seasonal variation analysis. Furthermore, since heat flux can be used to study the dissipation of gravity waves, knowledge of the contribution of gravity waves with various scales will help us understand how different the wave activities and dissipations are for different scale waves.

The key points of this study are listed below:

- The sensible heat flux $\langle w'T' \rangle$ is mostly downward below 95 km throughout the year and wave dissipation is negligible above 95 km. The magnitude is maximum during solstices and minimum around equinoxes.
- The enthalpy flux $\langle w'\theta' \rangle$ is downward throughout the region and year. Strong transport appears in several months at different altitudes, which agrees well with the strong wave activities inferred from large temperature variance.
- The energy flux $\langle w'p' \rangle$ varies in three orders of magnitude from 10^{-2} Wm^{-2} to 10^{-4} Wm^{-2} and decreases exponentially with altitude.
- Monthly heating rate shows strong cooling around southern hemisphere winter between 87 to 97 km where substantial GW dissipation occurs. The local cooling rate

due to heat flux divergence can exceed 30 Kd^{-1} during equinox in September. In the lower region of wave dissipation, the large upward sensible heat flux generates strong heating.

- Shorter period gravity waves contribute more to the heat transport and dissipate at higher altitude, which means small scale waves propagate more upward into MLT, which is consistent with the knowledge that high frequency gravity waves oscillate more vertically.

The last part of the dissertation (Chapter 5) is focused on the measurements of turbulence in the mesopause region with the high resolution ALO Na lidar. Turbulence has always been a challenge to measure in the MLT because of their small scales into seconds and meters. Modern observational techniques are required to possess the capability of resolving these small scale fluctuations associated with neutral densities, temperature, and winds. The upgrade of the ALO lidar system enables the data acquisition of raw data with high temporal and vertical resolutions at 6 s and 25 m, respectively, which makes it possible to study the turbulence and gravity wave at the same time. Unlike gravity wave perturbations, a new method is developed to derive the turbulence from raw data. The method relates the turbulence temperature and wind fluctuations to the raw photon count fluctuations through linearized system equations. Over 100 h observations on 19 nights are chosen for turbulence derivation. The derived turbulence are then used to calculate the turbulence spectra, heat flux, thermal diffusivity, energy dissipation rate, and the corresponding heating rate. This is the first time that turbulence heat flux and thermal diffusivity are directly measured with a Na lidar. The results can provide significant references for the energy distribution of turbulence and the diffusive process relates to the wave breaking theory. The measured eddy heat flux and diffusion coefficient can be applied as reference values for the parameterization of gravity waves in general circulation models.

The main results of this work are listed as follows:

- The power spectra of both frequency (ω) and vertical wavenumber (m) exhibit a power law distribution with slopes of -1.71 ± 0.14 and -1.73 ± 0.01 , respectively, consistent with the theoretical value of $-5/3$. Combined with the gravity wave spectra, it can be concluded that modern lidar system is capable of detecting gravity waves and turbulence within a large range of scales.
- The downward heat fluxes are comparable for waves and turbulence, and the corresponding net cooling rate of 12.8 K d^{-1} can bring substantial cooling effects to the mesopause region.
- The thermal diffusivity k_H is directly measured for the first time with an average of $43 \text{ m}^2 \text{ s}^{-1}$ and a maximum of $72 \text{ m}^2 \text{ s}^{-1}$ at 93 km, and generally decreases with altitude above, which is consistent with some other results of k_{zz} measured by balloons and rockets.
- The turbulence outer scale, estimated from energy dissipation rate ϵ ($\sim 40 \text{ mW/kg}$), is about 700 m, which is close to the 1 km chosen as the separation scale for gravity waves and turbulence.

6.2 Future Work

The work in this dissertation can be expanded into several future research topics. Now the current results have shown that the ALO Na lidar is capable of studying turbulence for multiple scales. By employing larger telescope receiving systems and higher power lasers, the required averaging times and uncertainties of the measured turbulence parameters can be reduced substantially, and the data will have a more complete coverage of turbulence spectra. With more observations in the future, it is also possible to characterize the seasonal

variation of turbulence fluxes, parameters, and statistical occurrences. Additionally, since the buoyancy frequency N applied to estimate the energy dissipation rate ε from eq. (5.4) is an average through all the profiles because of limited data, ε could be under- or over-estimated. Thus with higher quality data in the near future, the requirement of long period time average will be reduced and more accurate nightly profiles will be available.

Another analysis that can be done further by the lidar data is the turbulence momentum flux. Different as gravity waves, turbulence fluctuations are approximately isotropic, the radial wind variance would be comparable to the vertical wind variance. Therefore, the results also suggest that it is possible for existing Doppler lidars to measure turbulence momentum flux and turbulent Prandtl number by using off-zenith measurements to retrieve turbulence horizontal wind perturbations with the same data processing technique used in this study. Prandtl number is one of the most crucial parameters in computational dynamics of the MLT to simulate the energy, heat, and momentum deposition. Now with the thermal diffusivity presented in this dissertation, direct measurements of Prandtl number is highly possible by deriving the momentum diffusivity from eddy momentum flux calculations.

Na lidar measures wind, temperature, and Na density between 80 and 105 km simultaneously. In addition to the vertical heat flux, vertical flux of atomic Na can also be directly calculated. It is known that vertical transport of atmospheric species through mixing, displacement, chemistry and advection, plays a crucial role in establishing the constituent structure in the MLT. Similar as heat flux, wave-induced dynamical transport arises when dissipating but non-breaking waves induce a net vertical displacement in the constituent as they propagate through the region. Chemically induced transport appears when winds alters the chemical production and loss of the species and can be contributed by both dissipating and non-dissipating waves. Following [*Gardner and Liu, 2010*], the seasonal transport of atomic Na and its effect on the Na layer over the ALO can be derived and compared with SOR.

Appendix A

Data Processing Procedures

A.1 Graphical User Interface

The lidar data processing is composed of three main parts as illustrated in Figure 2.7 including pre-processing, the retrieval of temperature, wind, and Na density, and the post-processing. A Graphical User Interface (GUI) is designed to achieve the signal processing of ALO Na lidar from raw photon counts as in Figure A.1.

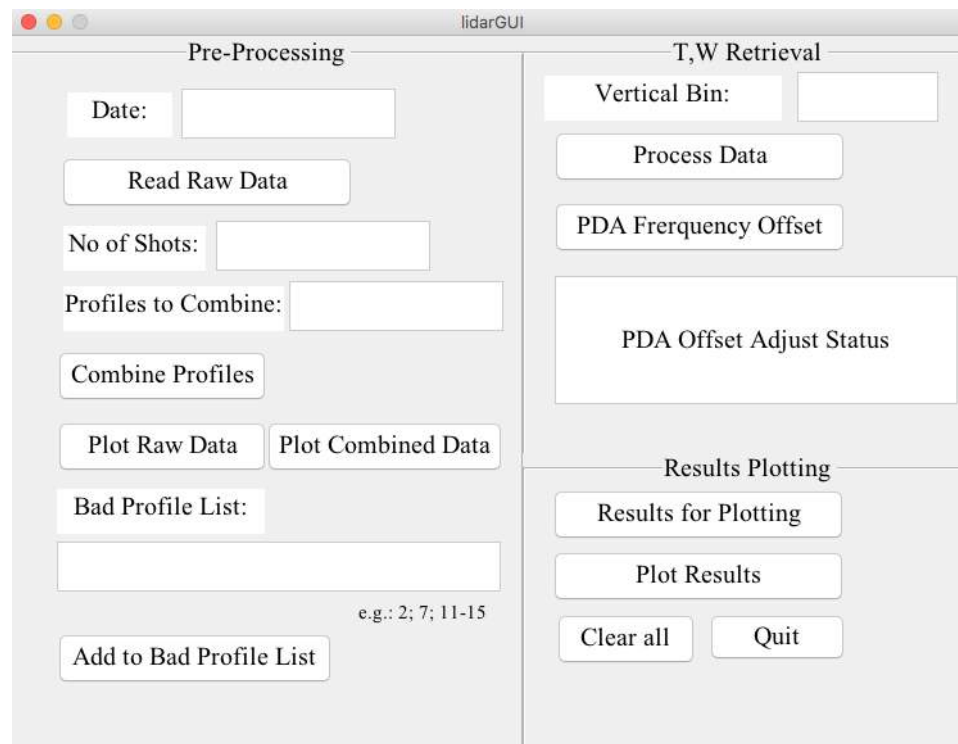


Figure A.1: The graphical user interface used to process the raw data of ALO Na lidar. Three modules are included: Pre-Processing, Parameter Retrieval, and Results Plotting

A.2 Procedures

The data processing programs are written in MATLAB. Here are the list of the files applied to process the raw ALO lidar data.

1. *readrawdata_nc.m* Read raw data on one night in ASCII format and save the information of photon counts, number of shots per profile, laser beam direction, etc. into a NetCDF format file.
2. *combine_ALO_rawdata_nc.m* Add multiple raw signal data profiles collected in sequence into a single profile. This is used to increase the signal level in each individual profile. Especially when the integration time is short. For example, with 6-sec integration time, 10 consecutive profiles can be added up together to construct a profile with 60-sec integration time. Only profiles in the same direction can be added up.
3. *plotrawstat_nc.m* Calculate the statistics of raw data for one night, include signals in background, Rayleigh layer, Na layer, and count-per-shot for all 3 frequencies. The results are saved in a file under Stats folder, and are also plotted. It's used for plotting both original and combined raw data. According to the statistics, profiles that do not meet certain criteria are treated as bad profiles. The numbers of bad profiles are saved in an ASCII file.
4. *Process_ALO_nc.m* Loop through all profiles to process in 3 steps: saturation correction, background subtract, and process. The parameters used in the processing along with the retrieved temperature, wind, and Na density are saved as results in a NetCDF file.
5. *PDA_Offset_adjust_nc.m* After one night's data is processed, this program reads in the results and calculates the mean vertical wind. Based on the value, it calculates

the required PDA offset adjustment that can make the mean vertical wind close to zero. This adjustment is saved in the result file. The next run of `Process_ALO.m` will read in this new parameter and produce updated results. This program will then be run iteratively to check if any further PDA offset adjustment is needed.

6. *ResultsforPlotting.m* Reads the result file saved in the NetCDF file and converts the light-of-sight winds into vertical and horizontal winds. Interpolate all the parameters into grid points vertically and temporally for plotting. When lidar is operated on zenith and off-zenith mode, the temperature and Na density from all direction are merged. New results are saved into a MATLAB data file.
7. *plotcontour_1.m* Plot the nightly temperature, vertical wind, zonal and meridional winds, and Na density in contours and save the plots.

The following are some key functions used in the above programs.

- *saturationCorrection_p.m* Correct the saturation effect PMT on all frequencies and altitudes.
- *BGSubtract_ALO.m* Remove the background from the signal. The input signal is a 2-d array for different altitudes and all three frequencies.
- *ReferenceDensity_new.m* Obtain the atmospheric density at the Rayleigh reference altitude from MSISE-00 model for each profile.
- *EffCross.m* Calculate the Na effective cross section, given laser frequency, temperature and wind.
- *dEffCrossT.m* Calculate the derivative of the effective cross section with respect to temperature.

- *dEffCrossW.m* Calculate the derivative of the effective cross section with respect to wind.
- *findT.m, findW.m, findTW.m* Find temperature, LOS wind, or both of them through iterative method from the ratios R_T and R_W .
- *dratioT3fdT.m, dratioT3fdW.m, dratioW3fdT.m, dratioW3fdW.m* Calculate the derivatives of the two ratios R_T and R_W with respect to temperature and wind. These are used for calculating temperature and wind from R_T and R_W using Newtons Method.

A.3 Data Processing Example

Here is an example of the ALO lidar data processing on April 24th, 2017. The data was acquired under 6 s integration time, which corresponding to The original Na layer and Rayleigh signals are plotted in Figure A.2.

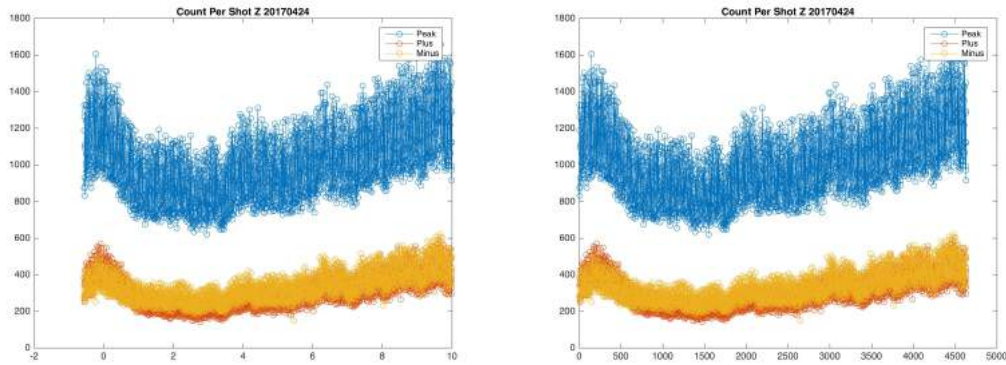


Figure A.2: The count-per-shot in Zenith direction for peak (blue), plus (red), and minus (yellow) frequencies on April 24th, 2017. Left is in time-series, right is in the sequence of profile number.

It can be seen that the signal is stable throughout the night, with a total observation of 10.5 hours and 4631 profiles. Since the integration time of the raw data is 6 second, under which the signal to noise ratio is not high enough to derive the temperature and wind

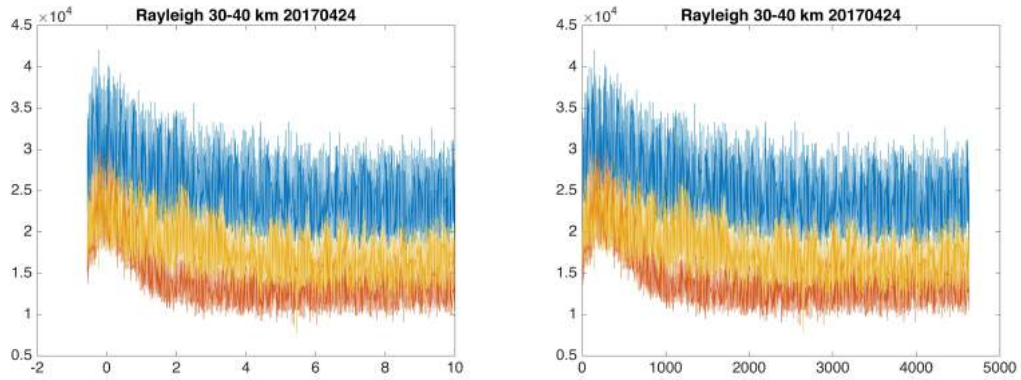


Figure A.3: Same as Figure A.2 but for Rayleigh signal.

directly, profiles are combined into a 60-second integration time for every 10 profiles from the same direction. These new profiles are plotted in Figure A.4.

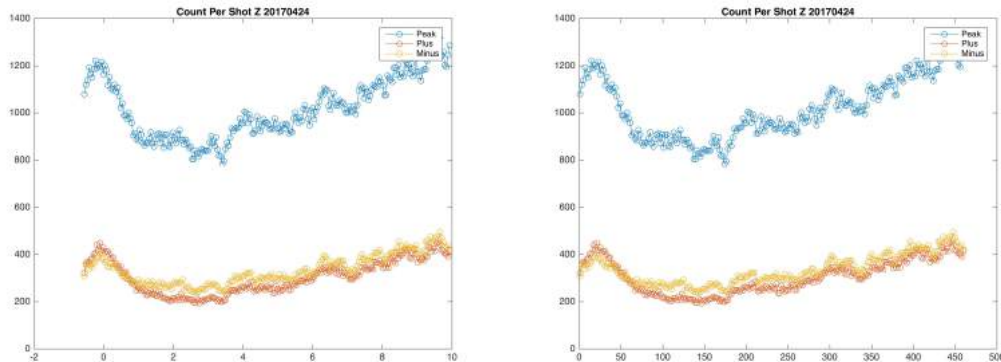


Figure A.4: Same as Figure A.2 but for combined profiles with 60 s integration time.

The processed Na density, temperature, and winds are shown in Figure A.5. The thermospheric Na layer appears at 4 UT around 160 km and then merge into the main Na layer at 8 UT, showing a clear downward phase progression.

The routine ALO Na Lidar data between 80-105 km and contour plots are available at <http://lidar.erau.edu/data/nalidar/>.

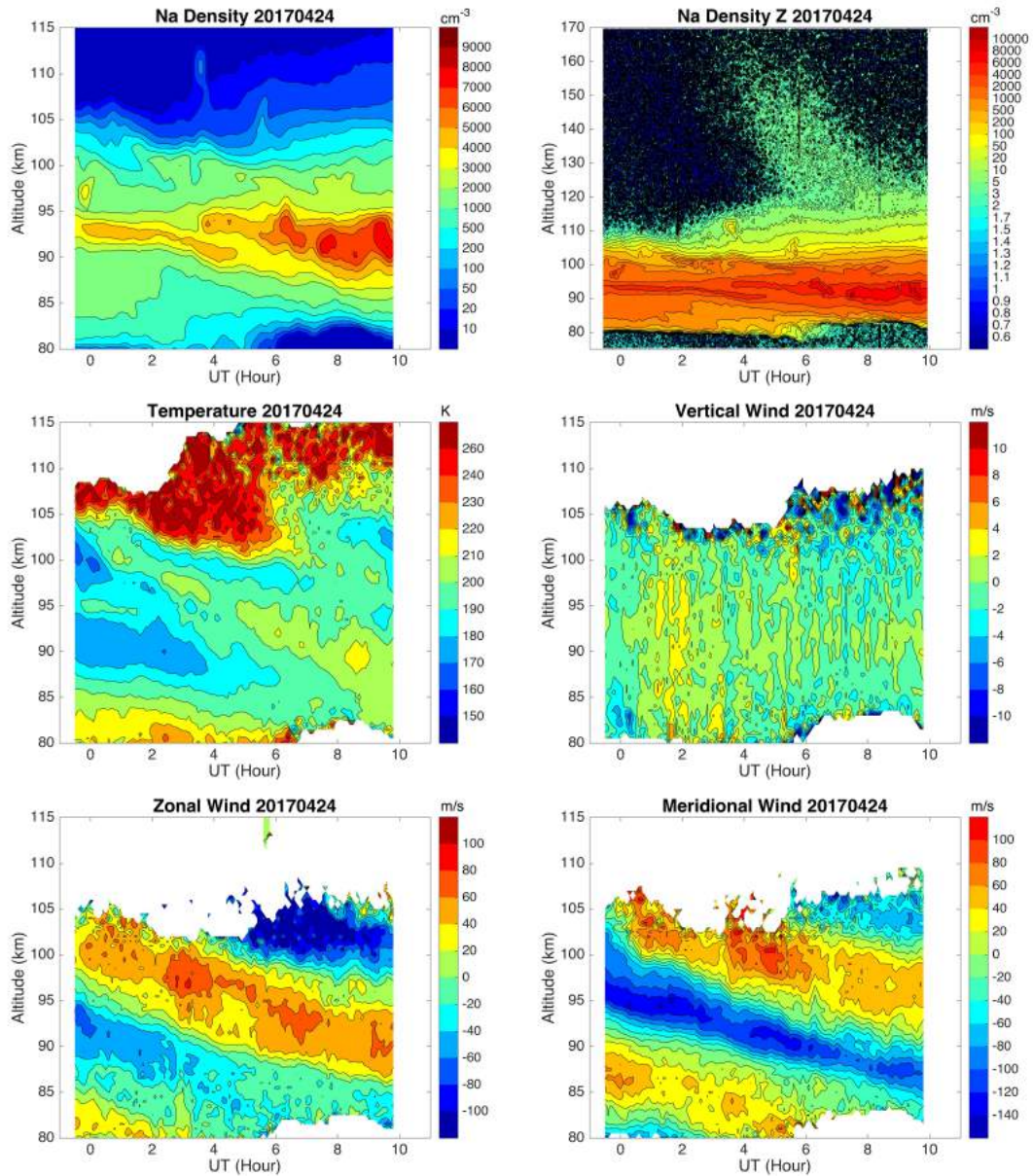


Figure A.5: From left to right, top to bottom are the Na density, thermospheric Na layer, temperature, vertical wind, zonal wind, meridional wind on April 24th, 2017. The resolutions are 60 s in temporal and 500 m in vertical.

Bibliography

- Acott, P. E., She, C.-Y., Krueger, D. A., Yan, Z.-A., Yuan, T., Yue, J., and Harrell, S. (2011). Observed nocturnal gravity wave variances and zonal momentum flux in mid-latitude mesopause region over Fort Collins, Colorado, USA. *J. Atmos. Sol.-Terr. Phys.*, 73(4):449–456.
- Adamiec, G., Heer, A. J., and Bluszcz, A. (2012). Statistics of count numbers from a photomultiplier tube and its implications for error estimation. *Radiation Measurements*, 47(9):746 – 751. Proceedings of the 13th International Conference on Luminescence and Electron Spin Resonance Dating, 10–14 July, 2011, Toruń, Poland.
- Akmaev, R. A. (2001). Simulation of large-scale dynamics in the mesosphere and lower thermosphere with the doppler-spread parameterization of gravity waves 2. eddy mixing and the diurnal tide. *J. Geophys. Res.*, 106(D1):1205–1213.
- Akmaev, R. A. (2007). On the energetics of mean-flow interactions with thermally dissipating gravity waves. *J. Geophys. Res.*, 112(D11):D11125.
- Albertson, J. D., Parlange, M. B., Kiely, G., and Eichinger, W. E. (1997). The average dissipation rate of turbulent kinetic energy in the neutral and unstable atmospheric surface layer. *Journal of Geophysical Research: Atmospheres*, 102(D12):13423–13432.
- Alexander, M. J. and Barnet, C. (2007). Using satellite observations to constrain parameterizations of gravity wave effects for global models. *J. Atmos. Sci.*, 64(5):1652–1665.
- Alexander, M. J., Geller, M., McLandress, C., Polavarapu, S., Preusse, P., Sassi, F., Sato, K., Eckermann, S., Ern, M., Hertzog, A., Kawatani, Y., Pulido, M., Shaw, T. A., Sigmond, M., Vincent, R., and Watanabe, S. (2010). Recent developments in gravity-wave

- effects in climate models and the global distribution of gravity-wave momentum flux from observations and models. *Quarterly Journal of the Royal Meteorological Society Q.J.R. Meteorol. Soc.*, 136(650):1103–1124.
- Alexander, M. J., Gille, J., Cavanaugh, C., Coffey, M., Craig, C., Eden, T., Francis, G., Halvorson, C., Hanningan, J., Khosravi, R., Kinnison, D., Lee, H., Massie, S., Nardi, B., Barnett, J., Hepplewhite, C., Lambert, A., and Dean, V. (2008). Global estimates of gravity wave momentum flux from High Resolution Dynamics Limb Sounder observations. *J. Geophys. Res.*, 113.
- Alexander, M. J., Holton, J. R., and Durran, D. (1995). The gravity wave response above deep convection in squall line simulation. *J. Atmos. Sci.*, 52(12):2212–2226.
- Alexander, M. J., May, P. T., and Beres, J. H. (2004). Gravity waves generated by convection in the Darwin area during the Darwin Area Wave Experiment. *J. Geophys. Res.*, 109.
- Allen, M., Yung, Y. L., and Waters, J. W. (1981). Vertical transport and photochemistry in the terrestrial mesosphere and lower thermosphere (50-120 km). *J. Geophys. Res.*, 86(A5):3617–3627.
- Allen, S. J. and Vincent, R. A. (1995). Gravity wave activity in the lower atmosphere: Seasonal and latitudinal variations. *J. Geophys. Res.*, 100(D1):1327–1350.
- Antonita, T. M., Ramkumar, G., Kumar, K. K., and Deepa, V. (2008). Meteor wind radar observations of gravity wave momentum fluxes and their forcing toward the Mesospheric Semiannual Oscillation. *J. Geophys. Res.*, 113.
- Beatty, T. J., Hostetler, C. A., and Gardner, C. S. (1992). Lidar observations of gravity waves and their spectra near the mesopause and stratopause at Arecibo. *J. Atmos. Sci.*, 49(6):477–496.

- Becker, E. (2004). Direct heating rates associated with gravity wave saturation. *Journal of Atmospheric and Solar-Terrestrial Physics*, 66(6–9):683 – 696. Dynamics and Chemistry of the MLT Region - PSMOS 2002 International Symposium.
- Becker, E. and Schmitz, G. (2002). Energy deposition and turbulent dissipation owing to gravity waves in the mesosphere. *Journal of the Atmospheric Sciences*, 59(1):54–68.
- Beres, J. H., Garcia, R. R., Boville, B. A., and Sassi, F. (2005). Implementation of a gravity wave source spectrum parameterization dependent on the properties of convection in the Whole Atmosphere Community Climate Model (WACCM). *J. Geophys. Res.*, 110(D10):D10108.
- Bernath, P. F., McElroy, C. T., Abrams, M. C., Boone, C. D., Butler, M., Camy-Peyret, C., Carleer, M., Clerbaux, C., Coheur, P.-F., Colin, R., DeCola, P., DeMazière, M., Drummond, J. R., Dufour, D., Evans, W. F. J., Fast, H., Fussen, D., Gilbert, K., Jennings, D. E., Llewellyn, E. J., Lowe, R. P., Mahieu, E., McConnell, J. C., McHugh, M., McLeod, S. D., Michaud, R., Midwinter, C., Nassar, R., Nichitiu, F., Nowlan, C., Rinsland, C. P., Rochon, Y. J., Rowlands, N., Semeniuk, K., Simon, P., Skelton, R., Sloan, J. J., Soucy, M.-A., Strong, K., Tremblay, P., Turnbull, D., Walker, K. A., Walkty, I., Wardle, D. A., Wehrle, V., Zander, R., and Zou, J. (2005). Atmospheric Chemistry Experiment (ACE): Mission overview. *Geophysical Research Letters*, 32(15):n/a–n/a. L15S01.
- Bevilacqua, R. M., Strobel, D. F., Summers, M. E., Olivero, J. J., and Allen, M. (1990). The seasonal variation of water vapor and ozone in the upper mesosphere: Implications for vertical transport and ozone photochemistry. *Journal of Geophysical Research: Atmospheres*, 95(D1):883–893.
- Bills, R. E., Gardner, C. S., and She, C. Y. (1991). Narrow band lidar technique for

- sodium temperature and doppler wind observations for the upper atmosphere. *Optical Engineering*, 30:13–21.
- Bishop, R. L., Larsen, M. F., Hecht, J. H., Liu, A. Z., and Gardner, C. S. (2004). TOMEX: Mesospheric and lower thermospheric diffusivities and instability layers. *J. Geophys. Res.*, 109.
- Bjarnason, G. G., Solomon, S., and Garcia, R. R. (1987). Tidal influences on vertical diffusion and diurnal variability of ozone in the mesosphere. *Journal of Geophysical Research: Atmospheres*, 92(D5):5609–5620.
- Blix, T. A., Thrane, E. V., and Andreassen, Ø. (1990). In situ measurements of the fine-scale structure and turbulence in the mesosphere and lower thermosphere by means of electrostatic positive ion probes. *Journal of Geophysical Research: Atmospheres*, 95(D5):5533–5548.
- Bossert, K., Fritts, D. C., Pautet, P.-D., Taylor, M. J., Williams, B. P., and Pendelton, W. R. (2014). Investigation of a mesospheric gravity wave ducting event using coordinated sodium lidar and Mesospheric Temperature Mapper measurements at ALOMAR, Norway (69°N). *Journal of Geophysical Research: Atmospheres*, 119(16):9765–9778. 2014JD021460.
- Cao, B., Heale, C. J., Guo, Y., Liu, A. Z., and Snively, J. B. (2016). Observation and modeling of gravity wave propagation through reflection and critical layers above Andes Lidar Observatory at Cerro Pachón, Chile. *Journal of Geophysical Research: Atmospheres*, 121(21):12,737–12,750. 2016JD025173.
- Carlson, C. G., Swenson, G. R., Dragic, P. D., and Liu, A. Z. (2005). Maui mesosphere and lower thermosphere (MALT) Na lidar enterprise. In Schäfer, K., Comerón, A. T.,

- Slusser, J. R., Picard, R. H., Carleer, M. R., and Sifakis, N., editors, *Remote Sensing of Clouds and the Atmosphere*, volume 5979 of *Proceedings of the SPIE*, pages 270–279.
- Ceselski, B. F. (1974). Cumulus convection in weak and strong tropical disturbances. *J. Atmos. Sci.*, 31:1241–1255.
- Chen, C., Chu, X., McDonald, A. J., Vadas, S. L., Yu, Z., Fong, W., and Lu, X. (2013). Inertia-gravity waves in Antarctica: A case study using simultaneous lidar and radar measurements at McMurdo/Scott Base (77.8°S, 166.7°E). *Journal of Geophysical Research: Atmospheres*, 118(7):2794–2808.
- Chimonas, G. and Grant, J. (1984). Shear excitation of gravity waves. part i: Modes of a two-scale atmosphere. *Journal of the Atmospheric Sciences*, 41(15):2269–2277.
- Chu, X., Gardner, C. S., and Franke, S. J. (2005). Nocturnal thermal structure of the mesosphere and lower thermosphere region at Maui, Hawaii (20.7°N), and Starfire Optical Range, New Mexico (35°N). *J. Geophys. Res.*, 110.
- Chu, X. and Papen, G. C. (2005). Resonance fluorescence lidar for measurement of the Middle and Upper Atmosphere. In Takashi, T. and Fukuchi, T., editors, *Laser Remote Sensing*, volume 87, pages 179–432. Taylor & Francis Group.
- Clayson, C. A. and Kantha, L. (2008). On turbulence and mixing in the free atmosphere inferred from high-resolution soundings. *Journal of Atmospheric and Oceanic Technology*, 25(6):833–852.
- Damiani, A., Storini, M., Santee, M. L., and Wang, S. (2010). Variability of the nighttime oh layer and mesospheric ozone at high latitudes during northern winter: influence of meteorology. *Atmospheric Chemistry and Physics*, 10(21):10291–10303.

- Das, U., Sinha, H. S. S., Sharma, S., Chandra, H., and Das, S. K. (2009). Fine structure of the low-latitude mesospheric turbulence. *J. Geophys. Res.*, 114(D10).
- Dewan, E. (1997). Saturated-cascade similitude theory of gravity wave spectra. *Journal of Geophysical Research: Atmospheres*, 102(D25):29799–29817.
- Dewan, E. M. (1994). The saturated-cascade model for atmospheric gravity wave spectra, and the wavelength-period (W-P) relations. *Geophysical Research Letters*, 21(9):817–820.
- Dewan, E. M. and Good, R. E. (1986). Saturation and the “universal” spectrum for vertical profiles of horizontal scalar winds in the atmosphere. *Journal of Geophysical Research: Atmospheres*, 91(D2):2742–2748.
- Eckermann, S. D., Hirota, I., and Hocking, W. K. (1995). Gravity wave and equatorial wave morphology of the stratosphere derived from long-term rocket soundings. *Quarterly Journal of the Royal Meteorological Society*, 121(521):149–186.
- Eckermann, S. D. and Preusse, P. (1999). Global measurements of stratospheric mountain waves from space. *Science*, 286:1534, doi:10.1126/science.286.5444.1534.
- Ehard, B., Achtert, P., Dörnbrack, A., Gisinger, S., Gumbel, J., Khaplanov, M., Rapp, M., and Wagner, J. (2016). Combination of lidar and model data for studying deep gravity wave propagation. *Monthly Weather Review*, 144(1):77–98.
- Engelbart, D. A. M. and Bange, J. (2002). Determination of boundary-layer parameters using wind profiler/RASS and sodar/RASS in the frame of the LITFASS project. *Theoretical and Applied Climatology*, 73(1):53–65.
- Eyler, E. E., Yiannopoulou, A., Gangopadhyay, S., and Melikechi, N. (1997). Chirp-free nanosecond laser amplifier for precision spectroscopy. *Opt. Lett.*, 22(1):49–51.

- Falkovich, G., Fouxon, A., and Stepanov, M. G. (2002). Acceleration of rain initiation by cloud turbulence. *Nature*, 419(6903):151–154.
- Fovell, R., Durran, D., and Holton, J. R. (1992). Numerical simulations of convectively generated stratospheric gravity waves. *Journal of the Atmospheric Sciences*, 49(16):1427–1442.
- Frederick, J. E. (1979). Influence of gravity wave activity on lower thermospheric photochemistry and composition. *Planet. Space Sci.*, 27(12):1469–1477.
- Fricke, K. H. and von Zahn, U. (1985). Mesopause temperatures derived from probing the hyperfine structure of the D₂ resonance line of sodium by lidar. *J. Atmos. Terr. Phys.*, 47(5):499–512.
- Fritts, D. C. (1982). Shear excitation of atmospheric gravity waves. *Journal of the Atmospheric Sciences*, 39(9):1936–1952.
- Fritts, D. C. (1984). Shear excitation of gravity waves. Part II: Upscale scattering from Kelvin-Helmholtz waves. *Journal of the Atmospheric Sciences*, 41(15):2278–2288.
- Fritts, D. C. and Alexander, M. J. (2003). Gravity wave dynamics and effects in the middle atmosphere. *Rev. Geophys.*, 41(1).
- Fritts, D. C., Bizon, C., Werne, J. A., and Meyer, C. K. (2003). Layering accompanying turbulence generation due to shear instability and gravity-wave breaking. *J. Geophys. Res.*, 108(D8).
- Fritts, D. C., Janches, D., Riggins, D. M., Stockwell, R. G., Sulzer, M. P., and Gonzales, S. (2006). Gravity waves and momentum fluxes in the mesosphere and lower thermosphere using 430 MHz dual-beam measurements at Arecibo: 2. Frequency spectra, momentum fluxes, and variability. *J. Geophys. Res.*, 111:D18108, doi:10.1029/2005JD006883.

- Fritts, D. C. and Nastrom, G. D. (1992). Sources of mesoscale variability of gravity waves. part ii: Frontal, convective, and jet stream excitation. *J. Atmos. Sci.*, 49(2):111–127.
- Fritts, D. C. and Rastogi, P. K. (1985). Convective and dynamical instabilities due to gravity wave motions in the lower and middle atmosphere: Theory and observations. *Radio Science*, 20(6):1247–1277.
- Fritts, D. C., Tsuda, T., Kato, S., Sato, T., and Fukao, S. (1988). Observational evidence of a saturated gravity wave spectrum in the troposphere and lower stratosphere. *Journal of the Atmospheric Sciences*, 45(12):1741–1759.
- Fritts, D. C. and Vincent, R. A. (1987). Mesospheric momentum flux studies at Adelaide, Australia: Observations and a gravity wave–tidal interaction model. *J. Atmos. Sci.*, 44(3):605–619.
- Fritts, D. C., Wan, K., Franke, P. M., and Lund, T. (2012). Computation of clear-air radar backscatter from numerical simulations of turbulence: 3. off-zenith measurements and biases throughout the lifecycle of a kelvin-helmholtz instability. *Journal of Geophysical Research: Atmospheres*, 117(D17):n/a–n/a. D17101.
- Fritts, D. C., Wan, K., Werne, J., Lund, T., and Hecht, J. H. (2014). Modeling the implications of Kelvin-Helmholtz instability dynamics for airglow observations. *J. Geophys. Res. Atmos.*, 119(14):2014JD021737.
- Fukao, S., Yamanaka, M. D., Ao, N., Hocking, W. K., Sato, T., Yamamoto, M., Nakamura, T., Tsuda, T., and Kato, S. (1994). Seasonal variability of vertical eddy diffusivity in the middle atmosphere 1. Three-year observations by the middle and upper atmosphere radar. *J. Geophys. Res.*, 99(D9):18973–18987.
- Funke, B., López-Puertas, M., García-Comas, M., Stiller, G. P., von Clarmann, T., Höpfner, M., Glatthor, N., Grabowski, U., Kellmann, S., and Linden, A. (2009). Carbon monoxide

- distributions from the upper troposphere to the mesosphere inferred from 4.7 m non-local thermal equilibrium emissions measured by MIPAS on Envisat. *Atmospheric Chemistry and Physics*, 9(7):2387–2411.
- Gage, K. S. and Balsley, B. B. (1984). MST radar studies of wind and turbulence in the middle atmosphere. *J. Atmos. Terr. Phys.*, 46:739–753.
- Garcia, R. R., López-Puertas, M., Funke, B., Kinnison, D. E., Marsh, D. R., and Qian, L. (2016). On the secular trend of CO_x and CO₂ in the lower thermosphere. *J. Geophys. Res. Atmos.*, 121(7):3634–3644.
- Garcia, R. R. and Solomon, S. (1985). The effect of breaking gravity waves on the dynamics and chemical composition of the mesosphere and lower thermosphere. *J. Geophys. Res.*, 90(D2):3850–3868.
- Gardner, C. S. (1994). Diffusive filtering theory of gravity wave spectra in the atmosphere. *J. Geophys. Res.*, 99(D10):20,601–20,622.
- Gardner, C. S. (1998). Theoretical models for gravity wave horizontal wave number spectra: Effects of wave field anisotropies. *J. Geophys. Res.*, 103(D6):6417–6425.
- Gardner, C. S., Espy, P. J., Forbes, J. M., Hysell, D. L., Liu, H.-L., Plane, J. M. C., Rapp, M., Swenson, G. R., Thayer, J. T., and Walterscheid, R. L. (2014). OASIS: Exploring the Interaction of Earth’s Atmosphere with Space, An Atmospheric and Geospace Sciences Report Submitted to NSF. page <http://rsss.csl.illinois.edu/workshop>.
- Gardner, C. S., Franke, S. J., Yang, W., Tao, X., and Yu, J. R. (1998). Interpretation of gravity waves observed in the mesopause region at Starfire Optical Range, New Mexico: Strong evidence for nonseparable intrinsic (m, ω) spectra. *J. Geophys. Res.*, 103(D8):8699–8713.

- Gardner, C. S., Gulati, K., Zhao, Y., and Swenson, G. R. (1999). Measuring gravity wave momentum fluxes with airglow imagers. *J. Geophys. Res.*, 104(D10):11,903–11,915.
- Gardner, C. S., Hostetler, C. A., and Lintelman, S. (1993). Influence of the mean wind field on the separability of atmospheric perturbation spectra. *J. Geophys. Res.*, 98(D5):8859–8872.
- Gardner, C. S. and Liu, A. Z. (2007). Seasonal variations of the vertical fluxes of heat and horizontal momentum in the mesopause region at Starfire Optical Range, New Mexico. *J. Geophys. Res.*, 112.
- Gardner, C. S. and Liu, A. Z. (2010). Wave-induced transport of atmospheric constituents and its effect on the mesospheric Na layer. *J. Geophys. Res.*, 115(D20):D20302.
- Gardner, C. S. and Liu, A. Z. (2014). Measuring eddy heat and constituent fluxes with High-Resolution Na and Fe Doppler Lidars. *J. Geophys. Res.*, 119:10583–10603.
- Gardner, C. S. and Liu, A. Z. (2016). Chemical transport of neutral atmospheric constituents by waves and turbulence: Theory and observations. *Journal of Geophysical Research: Atmospheres*, 121(1):494–520. 2015JD023145.
- Gardner, C. S., Liu, A. Z., and Guo, Y. (2016). Vertical and horizontal transport of mesospheric Na: Implications for the mass influx of cosmic dust. *Journal of Atmospheric and Solar-Terrestrial Physics*.
- Gardner, C. S. and Vargas, F. A. (2014). Optimizing three-frequency Na, Fe, and He lidars for measurements of wind, temperature, and species density and the vertical fluxes of heat and constituents. *Appl. Opt.*, 53(19):4100–4116.
- Gardner, C. S. and Yang, W. (1998). Measurements of the dynamical cooling rate associated with the vertical transport of heat by dissipating gravity waves in the mesopause

- region at the Starfire Optical Range, New Mexico. *J. Geophys. Res.*, 103(D14):16,909–16,926.
- Gavrilov, N. (1990). Parameterization of accelerations and heat flux divergences produced by internal gravity waves in the middle atmosphere. *Journal of Atmospheric and Terrestrial Physics*, 52(9):707 – 713.
- Gavrilov, N. M., Luce, H., Crochet, M., Dalaudier, F., and Fukao, S. (2005). Turbulence parameter estimations from high-resolution balloon temperature measurements of the MUTSI-2000 campaign. *Annales Geophysicae*, 23(7):2401–2413.
- Gibson, A. J., Thomas, L., and Bhattachacharyya, S. K. (1979). Laser observations of the ground-state hyperfine structure of sodium and of temperatures in the upper atmosphere. *Nature*, 281(5727):131–132.
- Gossard, E. E. (1962). Vertical flux of energy into the lower ionosphere from internal gravity waves generated in the troposphere. *Journal of Geophysical Research*, 67(2):745–757.
- Guo, Y. and Liu, A. Z. (2017). Seasonal variation of vertical heat and energy fluxes due to dissipating gravity waves in the mesopause region over the Andes. *Journal of Geophysical Research: Atmospheres*.
- Guo, Y., Liu, A. Z., and Gardner, C. S. (2017). First na lidar measurements of turbulence heat flux, thermal diffusivity, and energy dissipation rate in the mesopause region. *Geophysical Research Letters*. 2017GL073807.
- Hall, C. M., Hoppe, U. P., Blix, T. A., Thrane, E. V., Manson, A. H., and Meek, C. E. (1999). Seasonal variation of turbulent energy dissipation rates in the polar mesosphere: A comparison of methods. *Earth, Planets and Space*, 51(7):515–524.

- Hanle, W. (1924). Über magnetische beeinflussung der polarisation der resonanzfluoreszenz. *Zeitschrift für Physik*, 30(1):93–105.
- Hecht, J. H., Walterscheid, R. L., Fritts, D. C., Isler, J. R., Senft, D. C., Gardner, C. S., and Franke, S. J. (1997). Wave breaking signatures in OH airglow and sodium densities and temperatures 1. Airglow imaging, Na lidar and MF radar observations. *J. Geophys. Res.*, 102(D6):6655–6668.
- Hecht, J. H., Wan, K., Gelinas, L. J., Fritts, D. C., Walterscheid, R. L., Rudy, R. J., Liu, A. Z., Franke, S. J., Vargas, F. A., Pautet, P. D., Taylor, M. J., and Swenson, G. R. (2014). The life cycle of instability features measured from the Andes Lidar Observatory over Cerro Pachon on 24 March 2012. *J. Geophys. Res. Atmos.*, 119(14):8872–8898.
- Heck, W. J., Panofsky, H. A., and Bender, M. A. (1977). The effect of clear-air turbulence on a model of the general circulation of the atmosphere. *Beitr. Phys. Atmos.*, 50(89-97).
- Heisenberg, W. (1948). On the theory of statistical and isotropic turbulence. *Proceedings of the Royal Society of London A: Mathematical, Physical and Engineering Sciences*, 195(1042):402–406.
- Hickey, M. and Cole, K. (1988). A numerical model for gravity wave dissipation in the thermosphere. *Journal of Atmospheric and Terrestrial Physics*, 50(8):689 – 697.
- Hickey, M. P. and Brown, J. S. (2000). Resolving ambiguities in gravity wave propagation directions inherent in satellite observations: A simulation study. *Geophys. Res. Lett.*, 27(18):2901–2904.
- Hickey, M. P., Walterscheid, R. L., and Schubert, G. (2011). Gravity wave heating and cooling of the thermosphere: Sensible heat flux and viscous flux of kinetic energy. *Journal of Geophysical Research: Space Physics*, 116(A12):2156–2202. A12326.

- Hines, C. O. (1960). Internal atmospheric gravity waves at ionospheric heights. *Can. J. Phys.*, 38:1441–1481.
- Hines, C. O. (1965). Dynamical heating of the upper atmosphere. *Journal of Geophysical Research*, 70(1):177–183.
- Hines, C. O. (1970). Eddy diffusion coefficients due to instabilities in internal gravity waves. *J. Geophys. Res.*, 75(19):3937–3939.
- Hines, C. O. (1988). Generation of turbulence by atmospheric gravity waves. *J. Atmos. Sci.*, 45(7):1269–1278.
- Hines, C. O. (1991). The saturation of gravity waves in the middle atmosphere. part II: Development of doppler-spread theory. *Journal of the Atmospheric Sciences*, 48(11):1361–1379.
- Hocking, W. K. (1986). Observation and measurement of turbulence in the middle atmosphere with a VHF radar. *J. Atmos. Terr. Phys.*, 48(7):655–670.
- Hocking, W. K. (1996). An assessment of the capabilities and limitations of radars in measurements of upper atmosphere turbulence. *Adv. Space Res.*, 17(11):37–47.
- Hocking, W. K. (2005). A new approach to momentum flux determinations using SKiYMET meteor radars. *Ann. Geophys.*, 23(7):2433–2439.
- Hodges, R. R. (1967). Generation of turbulence in the upper atmosphere by internal gravity waves. *J. Geophys. Res.*, 72(13):3455–3458.
- Hodges, R. R. (1969). Eddy diffusion coefficients due to instabilities in internal gravity waves. *J. Geophys. Res.*, 74(16):4087–4090.

- Holton, J. R. (1983). The influence of gravity wave breaking on the circulation of the middle atmosphere. *J. Atmos. Sci.*, 40(10):2497–2507.
- Holton, J. R. and Alexander, M. J. (1999). Gravity waves in the mesosphere generated by tropospheric convection. *Tellus*, 51(A-B):45–58.
- Huang, T. Y. W. and Smith, A. K. (1991). The mesospheric diabatic circulation and the parameterized thermal effect of gravity wave breaking on the circulation. *Journal of the Atmospheric Sciences*, 48(8):1093–1111.
- Huang, W., Chu, X., Gardner, C. S., Carrillo-Sánchez, J. D., Feng, W., Plane, J. M. C., and Nesvorný, D. (2015). Measurements of the vertical fluxes of atomic Fe and Na at the mesopause: Implications for the velocity of cosmic dust entering the atmosphere. *Geophysical Research Letters*, 42(1):169–175. 2014GL062390.
- Jiang, J. H., Wu, D. L., and Eckermann, S. D. (2002). Upper Atmosphere Research Satellite (UARS) MLS observation of mountain waves over the Andes. *J. Geophys. Res.*, 107(D20):doi:10.1029/2002JD002091.
- Jin, J. J., Semeniuk, K., Jonsson, A. I., Beagley, S. R., McConnell, J. C., Boone, C. D., Walker, K. A., Bernath, P. F., Rinsland, C. P., Dupuy, E., Ricaud, P., De La Noë, J., Urban, J., and Murtagh, D. (2005). Co-located ACE-FTS and Odin/SMR stratospheric-mesospheric CO 2004 measurements and comparison with a GCM. *Geophysical Research Letters*, 32(15). L15S03.
- Kinnison, D. E., Brasseur, G. P., Walters, S., Garcia, R. R., Marsh, D. R., Sassi, F., Harvey, V. L., Randall, C. E., Emmons, L., Lamarque, J. F., Hess, P., Orlando, J. J., Tie, X. X., Randel, W., Pan, L. L., Gettelman, A., Granier, C., Diehl, T., Niemeier, U., and Simmons, A. J. (2007). Sensitivity of chemical tracers to meteorological parameters in the MOZART-3 chemical transport model. *J. Geophys. Res.*, 112(D20):D20302.

- Klostermeyer, J. (1990). On the role of parametric instability of internal gravity waves in atmospheric radar observations. *Radio Science*, 25(05):983–995.
- Kolmogorov, A. N. (1941). Dissipation of energy in locally isotropic turbulence. *Akademiia Nauk SSSR Doklady*, 32(16).
- Krueger, D. A., She, C.-Y., and Yuan, T. (2015). Retrieving mesopause temperature and line-of-sight wind from full-diurnal-cycle Na lidar observations. *Appl. Opt.*, 54(32):9469–9489.
- Larsen, M. F., Rutger, J., and Holden, D. N. (1987). Direct measurements of vertical-velocity power spectra with the SOUSY-VHF-Radar wind profiler system. *Journal of the Atmospheric Sciences*, 44(23):3442–3448.
- Li, T., She, C. Y., Liu, H.-L., and Montgomery, M. T. (2007). Evidence of a gravity wave breaking event and the estimation of the wave characteristics from sodium lidar observation over Fort Collins, CO (41°N, 105°W). *Geophys. Res. Lett.*, 34.
- Lindzen, R. S. (1981). Turbulence and stress owing to gravity wave and tidal breakdown. *J. Geophys. Res.*, 86:9707–9714.
- Liu, A. Z. (2009). Estimate eddy diffusion coefficients from gravity wave vertical momentum and heat fluxes. *Geophys. Res. Lett.*, 36.
- Liu, A. Z. and Gardner, C. S. (2005). Vertical heat and constituent transport in the mesopause region by dissipating gravity waves at Maui, Hawaii (20.7°N), and Starfire Optical Range, New Mexico (35°N). *J. Geophys. Res.*, 110.
- Liu, A. Z. and Guo, Y. (2016). Photomultiplier tube calibration based on Na lidar observation and its effect on heat flux bias. *Appl. Opt.*, 55(33):9467–9475.

- Liu, A. Z., Guo, Y., Vargas, F., and Swenson, G. R. (2016). First measurement of horizontal wind and temperature in the lower thermosphere (105–140 km) with a Na Lidar at Andes Lidar Observatory. *Geophys. Res. Lett.*, 43:doi:10.1002/2016GL068461.
- Liu, A. Z., Roble, R. G., Hecht, J. H., Larsen, M. F., and Gardner, C. S. (2004). Unstable layers in the mesopause region observed with na lidar during the turbulent oxygen mixing experiment (tomex) campaign. *J. Geophys. Res.*, 109.
- Liu, H.-L. (2000). Temperature changes due to gravity wave saturation. *J. Geophys. Res.*, 105(D10):12329–12336.
- Liu, H.-L., Hagan, M. E., and Roble, R. G. (2000). Local mean state changes due to gravity wave breaking modulated by the diurnal tide. *J. Geophys. Res.*, 105(D10):12381–12396.
- Lu, X., Chen, C., Huang, W., Smith, J. A., Chu, X., Yuan, T., Pautet, P.-D., Taylor, M. J., Gong, J., and Cullens, C. Y. (2015a). A coordinated study of 1 h mesoscale gravity waves propagating from Logan to Boulder with CRRL Na Doppler lidars and temperature mapper. *Journal of Geophysical Research: Atmospheres*, 120(19):10,006–10,021. 2015JD023604.
- Lu, X., Chu, X., Fong, W., Chen, C., Yu, Z., Roberts, B. R., and McDonald, A. J. (2015b). Vertical evolution of potential energy density and vertical wave number spectrum of Antarctic gravity waves from 35 to 105 km at McMurdo (77.8°S, 166.7°E). *Journal of Geophysical Research: Atmospheres*, 120(7):2719–2737. 2014JD022751.
- Lübken, F.-J. (1992). On the extraction of turbulent parameters from atmospheric density fluctuations. *J. Geophys. Res.*, 97(D18):20385–20395.
- Lübken, F.-J. (1997). Seasonal variation of turbulent energy dissipation rates at high latitudes as determined by in situ measurements of neutral density fluctuations. *J. Geophys. Res.*, 102(D12):13441–13456.

- Lübken, F.-J., Hillert, W., Lehmacher, G., and von Zahn, U. (1993). Experiments revealing small impact of turbulence on the energy budget of the mesosphere and lower thermosphere. *J. Geophys. Res.*, 98(D11):20369–20384.
- Lübken, F.-J., von Zahn, U., Thrane, E., Blix, T., Kokin, G., and Pachomov, S. (1987). In situ measurements of turbulent energy dissipation rates and eddy diffusion coefficients during MAP/WINE. *J. Atmos. Terr. Phys.*, 49(7-8):763–775.
- Lumley, J. L. and Panofsky, H. A. (1964). *The structure of atmospheric turbulence*. John Wiley & Sons.
- Matcheva, K. I. and Strobel, D. F. (1999). Heating of Jupiter's thermosphere by dissipation of gravity waves due to molecular viscosity and heat conduction. *Icarus*, 140(2):328 – 340.
- Medvedev, A. S. and Klaassen, G. P. (2003). Thermal effects of saturating gravity waves in the atmosphere. *J. Geophys. Res.*, 108(D2):4040, doi:10.1029/2002JD002504.
- Meraner, K. and Schmidt, H. (2016). Transport of nitrogen oxides through the winter mesopause in HAMMONIA. *J. Geophys. Res. Atmos.*, 121(6):2556–2570. 2015JD024136.
- Montgomery, R. B. (1948). Vertical eddy flux of heat in the atmosphere. *Journal of Meteorology*, 5(6):265–274.
- Nappo, C. J. (2013). *An introduction to atmospheric gravity waves*. Academic Press.
- Nastrom, G. D., VanZandt, T. E., and Warnock, J. M. (1997). Vertical wavenumber spectra of wind and temperature from high-resolution balloon soundings in the lower atmosphere over Illinois. *J. Geophys. Res.*, 102:6685–6702.

- O'Connor, E. J., Illingworth, A. J., Brooks, I. M., Westbrook, C. D., Hogan, R. J., Davies, F., and Brooks, B. J. (2010). A method for estimating the turbulent kinetic energy dissipation rate from a vertically pointing doppler lidar, and independent evaluation from balloon-borne in situ measurements. *Journal of Atmospheric and Oceanic Technology*, 27(10):1652–1664.
- Papen, G. C., Pfenninger, W. M., and Simonich, D. M. (1995). Sensitivity analysis of narrowband wind-temperature lidar systems. *Appl. Opt.*, 34(3):480–498.
- Peters, G. and Kirtzel, H. J. (1994). Measurements of momentum flux in the boundary layer by RASS. *Journal of Atmospheric and Oceanic Technology*, 11(1):63–75.
- Picone, J. M., Hedin, A. E., Drob, D. P., and Aikin, A. C. (2002). NRLMSISE-00 empirical model of the atmosphere: Statistical comparisons and scientific issues. *Journal of Geophysical Research: Space Physics*, 107(A12):1468.
- Pitteway, M. L. V. and Hines, C. O. (1963). The viscous damping of atmospheric gravity waves. *Can. J. Phys.*, 41(12):1935–1948.
- Plane, J. M. C., Feng, W., and Dawkins, E. C. M. (2015). The mesosphere and metals: Chemistry and changes. *Chemical Reviews*, 115(10):4497–4541. PMID: 25751779.
- Plumb, R. A. (1979). Eddy fluxes of conserved quantities by small-amplitude waves. *Journal of the Atmospheric Sciences*, 36(9):1699–1704.
- Priestley, C. H. B. and Swinbank, W. C. (1947). Vertical transport of heat by turbulence in the atmosphere. *Proceedings of the Royal Society of London A: Mathematical, Physical and Engineering Sciences*, 189(1019):543–561.
- Qian, L., Solomon, S. C., and Kane, T. J. (2009). Seasonal variation of thermospheric density and composition. *J. Geophys. Res.*, 114.

- Randall, C. E., Harvey, V. L., Singleton, C. S., Bernath, P. F., Boone, C. D., and Kozyra, J. U. (2006). Enhanced NO_x in 2006 linked to strong upper stratospheric Arctic vortex. *Geophysical Research Letters*, 33(18). L18811.
- Rapp, M., Strelnikov, B., Müllemann, A., Lübken, F.-J., and Fritts, D. C. (2004). Turbulence measurements and implications for gravity wave dissipation during the MaCWAVE/MIDAS rocket program. *Geophys. Res. Lett.*, 31:L24S07, doi:10.1029/2003GL019325.
- Rinsland, C. P., Boone, C., Nassar, R., Walker, K., Bernath, P., McConnell, J. C., and Chiou, L. (2005). Atmospheric Chemistry Experiment (ACE) Arctic stratospheric measurements of NO_x during February and March 2004: Impact of intense solar flares. *Geophysical Research Letters*, 32(16):n/a–n/a. L16S05.
- Sasi, M. N. and Vijayan, L. (2001). Turbulence characteristics in the tropical mesosphere as obtained by MST radar at Gadanki (13.5° N, 79.2° E). *Annales Geophysicae*, 19(8):1019–1025.
- Sato, K. (1990). Vertical wind disturbances in the troposphere and lower stratosphere observed by the mu radar. *J. Atmos. Sci.*, 47(23):2803–2817.
- Schneider, J. M. and Lilly, D. K. (1999). An observational and numerical study of a sheared, convective boundary layer. Part I: Phoenix II observations, statistical description, and visualization. *Journal of the Atmospheric Sciences*, 56(17):3059–3078.
- Schoeberl, M. R., Strobel, D. F., and Apruzese, J. P. (1983). A numerical model of gravity wave breaking and stress in the mesosphere. *J. Geophys. Res.*, 88(C9):5249–5259.
- Senft, D. C. and Gardner, C. S. (1991). Seasonal variability of gravity wave activity and spectra in the mesopause region at Urbana. *J. Geophys. Res.*, 96(D9):17229–17264.

- Senft, D. C., Hostetler, C. A., and Gardner, C. S. (1993). Characteristics of gravity wave activity and spectra in the upper stratosphere and upper mesosphere at Arecibo during early April 1989. *J. Atmos. Terr. Phys.*, 55(3):425–439.
- Seuront, L., Schmitt, F., Schertzer, D., Lagadeuc, Y., and Lovejoy, S. (1996). Multifractal intermittency of Eulerian and Lagrangian turbulence of ocean temperature and plankton fields. *Nonlinear Processes in Geophysics*, 3(4):236–246.
- Sharman, R. D., Trier, S. B., Lane, T. P., and Doyle, J. D. (2012). Sources and dynamics of turbulence in the upper troposphere and lower stratosphere: A review. *Geophysical Research Letters*, 39(12). L12803.
- She, C.-Y. (2001). Spectral structure of laser light scattering revisited: bandwidths of nonresonant scattering lidars. *Appl. Opt.*, 40(27):4875–4884.
- She, C. Y., Bills, R. E., Latifi, H., Yu, J. R., Alvarez, R. J., and Gardner, C. S. (1990). Two frequency lidar techniques for mesospheric sodium temperature measurements. *Geophys. Res. Lett.*, 17:929–932.
- She, C. Y. and Yu, J. R. (1994). Simultaneous three-frequency Na lidar measurements of radial wind and temperature in the mesopause region. *Geophys. Res. Lett.*, 21(17):1771–1774.
- She, C. Y. and Yu, J. R. (1995). Doppler-free saturation fluorescence spectroscopy of Na atoms for atmospheric applications. *Appl. Opt.*, 34:1063–1075.
- She, C. Y., Yu, J. R., Huang, J. W., Nagasawa, C., and Gardner, C. S. (1991). Na temperature lidar measurements of gravity wave perturbations of winds, density and temperature in the mesopause region. *Geophys. Res. Lett.*, 18(7):1329–1331.

- She, C. Y., Yu, J. R., Latifi, H., and Bills, R. E. (1992). High-spectral-resolution fluorescence light detection and ranging for mesospheric sodium temperature measurements. *Appl. Opt.*, 31(12):2095–2106.
- Smith, A. K. (2012). Global dynamics of the MLT. *Surveys in Geophysics*, 33(6):1177–1230.
- Smith, J. A. and Chu, X. (2015). High-efficiency receiver architecture for resonance-fluorescence and Doppler lidars. *Appl. Opt.*, 54(11):3173–3184.
- Smith, R. B. (1979). The influence of mountains on the atmosphere. *Advances in Geophysics*, 21:87 – 230.
- Smith, R. B. (1985). On severe downslope winds. *Journal of the Atmospheric Sciences*, 42(23):2597–2603.
- Smith, S., Baumgardner, J., and Mendillo, M. (2009). Evidence of mesospheric gravity-waves generated by orographic forcing in the troposphere. *Geophys. Res. Lett.*, 36.
- Snively, J. B., Pasko, V. P., Taylor, M. J., and Hocking, W. K. (2007). Doppler ducting of short-period gravity waves by midlatitude tidal wind structure. *J. Geophys. Res.*, 112:A03304, doi:10.1029/2006JA011895.
- Strobel, D. F., Summers, M. E., Bevilacqua, R. M., DeLand, M. T., and Allen, M. (1987). Vertical constituent transport in the mesosphere. *Journal of Geophysical Research: Atmospheres*, 92(D6):6691–6698.
- Su, L., Collins, R. L., Krueger, D. A., and She, C.-Y. (2008). Statistical analysis of sodium doppler wind–temperature lidar measurements of vertical heat flux. *Journal of Atmospheric and Oceanic Technology*, 25(3):401–415.

- Sukoriansky, S., Galperin, B., and Perov, V. (2005). Application of a new spectral theory of stably stratified turbulence to the atmospheric boundary layer over sea ice. *Boundary-Layer Meteorology*, 117(2):231–257.
- Sun, J., Nappo, C. J., Mahrt, L., Belušić, D., Grisogono, B., Stauffer, D. R., Pulido, M., Staquet, C., Jiang, Q., Pouquet, A., Yagüe, C., Galperin, B., Smith, R. B., Finnigan, J. J., Mayor, S. D., Svensson, G., Grachev, A. A., and Neff, W. D. (2015). Review of wave-turbulence interactions in the stable atmospheric boundary layer. *Reviews of Geophysics*, 53(3):956–993. 2015RG000487.
- Suzuki, S., Shiokawa, K., Otsuka, Y., Kawamura, S., and Murayama, Y. (2013). Evidence of gravity wave ducting in the mesopause region from airglow network observations. *Geophysical Research Letters*, 40(3):601–605.
- Swinbank, W. C. (1951). The measurement of vertical transfer of heat and water vapor by eddies in the lower atmosphere. *Journal of Meteorology*, 8(3):135–145.
- Tao, X. and Gardner, C. S. (1995). Heat Flux observations in the mesopause region above Haleakala. *Geophys. Res. Lett.*, 22(20):2829–2832.
- Tatarskii, V. I. (1971). The effects of the turbulent atmosphere on wave propagation. *Jerusalem: Israel Program for Scientific Translations, 1971.*
- Taylor, G. I. (1915). Eddy motion in the atmosphere. *Philosophical Transactions of the Royal Society of London. Series A, Containing Papers of a Mathematical or Physical Character*, 215:1–26.
- Taylor, M. J., Gu, Y. Y., Tao, X., and Gardner, C. S. (1995). An investigation of intrinsic gravity wave signatures using coordinated lidar and nightglow image measurements. *Geophys. Res. Lett.*, 22(20):2853–2856.

- Vadas, S. L. (2013). Compressible f-plane solutions to body forces, heatings, and coolings, and application to the primary and secondary gravity waves generated by a deep convective plume. *Journal of Geophysical Research: Space Physics*, 118(5):2377–2397.
- Vadas, S. L. and Fritts, D. C. (2006). Influence of solar variability on gravity wave structure and dissipation in the thermosphere from tropospheric convection. *J. Geophys. Res.*, 111.
- VanZandt, T. E. and Fritts, D. C. (1989). A theory of enhanced saturation of the gravity wave spectrum due to increases in atmospheric stability. *pure and applied geophysics*, 130(2):399–420.
- VanZandt, T. E., Nastrom, G. D., and Green, J. L. (1991). Frequency spectra of vertical velocity from Flatland VHF radar data. *Journal of Geophysical Research: Atmospheres*, 96(D2):2845–2855.
- Vincent, R. (1984). Gravity-wave motions in the mesosphere. *Journal of Atmospheric and Terrestrial Physics*, 46(2):119 – 128.
- Vincent, R. A. and Reid, I. M. (1983). HF Doppler measurements of mesospheric gravity wave momentum fluxes. *J. Atmos. Sci.*, 40(5):1321–1333.
- Vlasov, M. N. and Kelley, M. C. (2014). Criterion for analyzing experimental data on eddy diffusion coefficients. *Ann. Geophys.*, 32(6):581–588.
- Vlasov, M. N. and Kelley, M. C. (2015). Eddy diffusion coefficients and their upper limits based on application of the similarity theory. *Ann. Geophys.*, 33(7):857–864.
- Walterscheid, R. L. (1981a). Dynamical cooling induced by dissipating internal gravity waves. *Geophys. Res. Lett.*, 8(12):1235–1238.

- Walterscheid, R. L. (1981b). Inertial-gravity wave induced accelerations of mean flow having an imposed periodic component: Implications for tidal observations in the meteor region. *J. Geophys. Res.*, 86(C10):9698–9706.
- Walterscheid, R. L. (2001). Gravity wave transports and their effects on the large-scale circulation of the upper mesosphere and lower thermosphere. *Adv. Space Res.*, 27(10):1713–1721.
- Walterscheid, R. L. and Hickey, M. P. (2011). Group velocity and energy flux in the thermosphere: Limits on the validity of group velocity in a viscous atmosphere. *Journal of Geophysical Research: Atmospheres*, 116(D12). D12101.
- Walterscheid, R. L. and Schubert, G. (1990). Nonlinear evolution of an upward propagation gravity wave: overturning, convection, transience and turbulence. *J. Atmos. Sci.*, 47(1):101–125.
- Wang, L., Fritts, D. C., Williams, B. P., Goldberg, R. A., Schmidlin, F. J., and Blum, U. (2006). Gravity waves in the middle atmosphere during the MaCWAVE winter campaign: evidence of mountain wave critical level encounters. *Ann. Geophys.*, 24:1209–1226.
- Weinstock, J. (1978). Vertical turbulent diffusion in a stably stratified fluid. *J. Atmos. Sci.*, 35(6):1022–1027.
- Weinstock, J. (1981). Energy dissipation rates of turbulence in the stable free atmosphere. *Journal of the Atmospheric Sciences J. Atmos. Sci.*, 38(4):880–883.
- Weinstock, J. (1982). Nonlinear theory of gravity waves: Momentum deposition, generalized Rayleigh friction, and diffusion. *J. Atmos. Sci.*, 39(8):1698–1710.

- Weinstock, J. (1983). Heat flux induced by gravity waves. *Geophys. Res. Lett.*, 10(2):165–167.
- Weinstock, J. (1990). Saturated and unsaturated spectra of gravity waves and scale-dependent diffusion. *Journal of the Atmospheric Sciences*, 47(18):2211–2226.
- Williams, B. P., Fritts, D. C., Vance, J. D., She, C. Y., Abe, T., and Thrane, E. (2006). Sodium lidar measurements of waves and instabilities near the mesopause during the DELTA rocket campaign. *Earth Planets Space*, 58(9):1131–1137.
- Xu, J., Gao, H., Smith, A. K., and Zhu, Y. (2012). Using TIMED/SABER nightglow observations to investigate hydroxyl emission mechanisms in the mesopause region. *J. Geophys. Res.*, 117(D2):D02301.
- Xu, J., Smith, A. K., and Ma, R. (2003). A numerical study of the effect of gravity-wave propagation on minor species distributions in the mesopause region. *J. Geophys. Res.*, 108(D3).
- Yang, G., Clemesha, B., Batista, P., and Simonich, D. (2008). Lidar study of the characteristics of gravity waves in the mesopause region at a southern low-latitude location. *J. Atmos. Sol.-Terr. Phys.*, 70(7):991–1011.
- Yiğit, E. and Medvedev, A. S. (2009). Heating and cooling of the thermosphere by internal gravity waves. *Geophys. Res. Lett.*, 36(14):L14807.
- Yiğit, E., Medvedev, A. S., Aylward, A. D., Hartogh, P., and Harris, M. J. (2009). Modeling the effects of gravity wave momentum deposition on the general circulation above the turbopause. *J. Geophys. Res.*, 114:D07101, doi:10.1029/2008JD011132.
- Yu, J. R. and She, C. Y. (1995). Climatology of a midlatitude mesopause region observed

- by a lidar at Fort Collins, Colorado (40.6°N, 105°W). *Journal of Geophysical Research: Atmospheres*, 100(D4):7441–7452.
- Yu, Y. and Hickey, M. P. (2007). Time-resolved ducting of atmospheric acoustic-gravity waves by analysis of the vertical energy flux. *Geophysical Research Letters*, 34(2).
- Yuan, T. (2004). *Seasonal variations of diurnal and semidiurnal tidal-period perturbations in mesopause region temperature and zonal and meridional winds above Fort Collins, Colorado (40 degrees° N, 105 °W) based on sodium-Lidar observation over full diurnal cycles*. PhD thesis, Colorado State University.
- Yuan, T., Heale, C. J., Snively, J. B., Cai, X., Pautet, P.-D., Fish, C., Zhao, Y., Taylor, M. J., Pendleton, W. R., Wickwar, V., and Mitchell, N. J. (2016). Evidence of dispersion and refraction of a spectrally broad gravity wave packet in the mesopause region observed by the Na lidar and Mesospheric Temperature Mapper above Logan, Utah. *Journal of Geophysical Research: Atmospheres*, 121(2):579–594. 2015JD023685.
- Zhang, S. D., Huang, C. M., Huang, K. M., Zhang, Y. H., Gong, Y., and Gan, Q. (2017). Vertical wavenumber spectra of three-dimensional winds revealed by radiosonde observations at midlatitude. *Annales Geophysicae*, 35(1):107–116.
- Zhang, S. D., Yi, F., Huang, C. M., and Huang, K. M. (2012). High vertical resolution analyses of gravity waves and turbulence at a midlatitude station. *J. Geophys. Res.*, 117(D2):D02103.
- Zhang, X., Forbes, J. M., Hagan, M. E., Russell III, J. M., Palo, S. E., Mertens, C. J., and Mlynczak, M. G. (2006). Monthly tidal temperatures 20–120 km from TIMED/SABER. *J. Geophys. Res.*, 111.
- Zhao, Y., Liu, A. Z., and Gardner, C. S. (2003). Measurements of atmospheric stability in

- the mesopause region at Starfire Optical Range, NM. *J. Atmos. Sol.-Terr. Phys.*, 65:219–232.
- Zhu, X. (1994). A new theory of the saturated gravity wave spectrum for the middle atmosphere. *J. Atmos. Sci.*, 51(24):3615–3626.
- Zhu, X., Yee, J.-H., Swartz, W. H., Talaat, E. R., and Coy, L. (2010). A spectral parameterization of drag, eddy diffusion, and wave heating for a three-dimensional flow induced by breaking gravity waves. *J. Atmos. Sci.*, 67(8):2520–2536.
- Zimmermann, D. (1975). Determination of the lifetime of the $4p_{1/2}$ -state of potassium by Hanle-effect. *Zeitschrift für Physik A*, 275(5):5–10.
- Zink, F. and Vincent, R. A. (2004). Some inferences on turbulence generation by gravity waves. *J. Geophys. Res.*, 109.